Numerical Perspective on Tsunami Hazards and Their Mitigation by Coastal Vegetation

Roberto Marivela Colmenarejo

Dissertation submitted to the Faculty of the
Virginia Polytechnic Institute and State University
in partial fulfillment of the requirements for the degree of

Doctor of Philosophy
in
Geosciences

Robert Weiss, Chair
Martin Chapman
Scott D. King
Christopher Roy
Nina Stark

April 25, 2017
Blacksburg, Virginia

Keywords: tsunami, solitary waves, coastal vegetation

Numerical Perspective on Tsunami Hazards and Their Mitigation by Coastal Vegetation

Roberto Marivela Colmenarejo

ABSTRACT

Tsunamis are among the most threatening natural hazards that can affect coastal communities and infrastructures. In order to provide useful information for coastal protection, one of my aims in this dissertation is to identify the physical metrics that better represent the damage cause by tsunamis. I approach this problem by carrying out three-dimensional-SPH numerical simulations of solitary waves which allow to track spatial-temporal evolution of physical variables during their breaking. By comparing these evolutions it is possible to visualize the complex hydrodynamic process that occurs during breaking. Results show that the highest danger lies in the environment of the shoreline. However the highest vulnerability of coastal communities and infrastructures lies onshore where they find themselves more exposed to the destructive capacity of extreme tsunami waves. In this regard, the second main goal in this dissertation is to understand how coastal vegetation reduces and modifies the onshore wave inundation. I address this problem by using shallow water equations and Serre-Green-Naghdi equations employed in a set of two-dimensional depth-integrated simulations. Analysis of results indicate the existence of a transition zone located between where runup is not affected at all and where runup suffers the maximum reduction by the vegetation. This infers the requirement of a minimum length of the vegetated barrier in order to achieve the maximum runup reduction under a specific set properties such as barrier location, barrier width, beach slope and/or wave amplitude. Overall we conclude, after intense validation work, that numerical approaches are very convenient tools to analyze difficult wave processes. However it is necessary to be aware of the limitation of each numerical approach.

Numerical Perspective on Tsunami Hazards and Their Mitigation by Coastal Vegetation

Roberto Marivela Colmenarejo

GENERAL AUDIENCE ABSTRACT

Tsunamis are long waves with large wave height that are mainly generated by ocean-based earthquakes. They can also be a consequence of other natural events such as landslides, intense volcanic activities, large storm floods or even asteroid impacts. Coastal communities tend to not consider these low-frequency threats and occupy large coastal areas and so they become very vulnerable to tsunamis. In this dissertation, two main goals are addressed: The first one is to identify where and when the highest dangerousness of the tsunamis occur so coastal habitants can avoid such areas. The second goal focuses on the flooding areas caused by tsunamis where onshore habitants are more vulnerable. We study how a natural element, such as coastal vegetation, affects, reduces and modifies the flooding due to tsunamis. Some design criteria are presented for the coastal vegetation to reduce the flooding to a maximum.

Acknowledgments

I would like to mention my most sincere appreciation to Dr. Robert Weiss, not just for providing me the chance to be part of his group, but also for his support, knowledge and guidance. This change has become the most intense experience in my life. I would also like to honestly thank my committee members, Drs. Martin Chapman, Scott King, Christopher Roy and Nina Stark for their extremely useful comments along these four years of research. They have provided me focus and wisdom criteria. Additionally I would like to mention my most sincere appreciation to Amir Zainali and Kannikha Kolandaivelu for their experience, patience, friendship and love during these years of work.

The work presented in this document has been partially supported by the National Science Foundation under the Grants No. NSF-CMMI-1208147 and NSF-CMMI-1206271.

Contents

List of Figures

List of Tables

Chapter 1

Introduction

More than half of world's population lives and works within 200 km from the coast as of 1998, and 75 percent within 400 km according to NOAA[1]. In the United States of America, it is estimated that 55-60 percent of the population lives in cities around the coast and its density has increased from 275 to 400 habitants per square kilometer between 1960 and 1990. More recent studies, as per United Nations Environment Programme[2] (UNEP), estimated that over 50 percent of the world's population lives within 60 km of the coast as of today. This trend of the population to occupy near-shore areas makes the coastal population and infrastructures vulnerable to damage caused by tsunamis.

Additionally, taking into account that 80 percent of the volcanic eruptions on Earth take place in the oceanic crust (NOAA[3]), that over 81 percent of the world's largest earthquakes occur in oceanic crust (USGS[4]) and that 71 percent of the Earth's surface is covered by oceans, tsunamis are a serious threat that can significantly affect coastal communities and infrastructures even when they are located far away from the tsunami source. These communities are becoming more exposed to the tsunamis as the population migration towards the coastal big cities has increased and additionally the increasing sea level (~1 m by 2100 A.D. as per USGS[5] predictions) due to global warming increase the risk factor.

A tsunami is a sequence of water waves generated by a disturbance of the ocean floor due to natural events such as earthquakes. Since tsunamis are very long waves they can travel though the ocean from the source location with almost no energy dissipation and affect large areas of coast. Hence, tsunamis are one of the most threatening natural hazards and often

---

[1] http://oceanservice.noaa.gov/websites/retiredsites/natdia_pdf/3hinrichsen.pdf

[2] http://web.unep.org/urban_environment/issues/coastal_zones.asp

[3] http://oceantoday.noaa.gov/deepoceanvolcanoes/

[4] https://www2.usgs.gov/faq/categories/9831/3342

[5] https://wh.er.usgs.gov/slr/sealevelrise.html

they are more dangerous than the parent earthquake, for example. The natural events that originate tsunamis are:

- Volcanic explosions and collapse/engulfment of the volcanic chambers or failure of their slopes may generate sudden displacement of water that leads to extremely destructive tsunami waves in the immediate source area. Events have been documented, for instance, in the volcano of Santorini island where volcanic eruption and the resulting tsunami is believed to have destroyed the Greek Minoan civilization around 1490 B.C. Another example is the explosion of the Krakatoa volcano which generated a $>$ 40 m high tsunami wave due to collapse of its caldera into the ocean.

- Asteroid impacts can also be source of tsunami waves, next to earthquakes. The most evidenced event of this kind is the Eltanin impact that occurred in the late Pliocene, around 2.5 Ma ago, in the current southwest Chile. It is estimated that the asteroid was between 1 and 4 km in diameter and traveled at a velocity of 20 km/s. It left a crater 35 km in diameter. Numerical simulations show that waves would have been 35 m high. Fortunately, events of this high magnitude are very unlikely to occur in the near future.

- Landslides are the second most common tsunami source. Emerged and submerged landslides in the coast margins involve a rapid displacement of mass into the water, resulting in water displacement generating tsunamis. Landslides are frequently triggered by earthquakes and those that occur in inlets generate fierce tsunamis because the waves interact with each other very intensely which makes them gain extra destructive capacity that locally focuses in the bay. This was the case in 1958, in Lituya

Bay, Alaska, where 60 million cubic meters of rock fell into the bay pushing water to about 525 m high on the opposite slope and generating a 30 m high tsunami wave that traveled across the bay.

- Earthquakes are the most common source of tsunamis as earthquakes occur more frequently than the aforementioned natural events. The displacement of the bottom ocean due to an earthquake triggers a displacement of the water mass producing tsunami waves. Among many examples, the latest and more important earthquakes that generated large tsunamis in recent history are:
  - The 2004 Indian Ocean earthquake, with a 9.1-9.3 magnitude, was the third largest earthquake ever recorded and it generated a tsunami wave of ~ 30 m height. It was one of the deadliest natural disaster in recent history, killing between 230,000-280,000 people in 14 countries distributed around the Indian Ocean coast. This shows that in the case of earthquakes, the damage area and resulting casualties caused by earthquake-generated tsunami can far exceed the damage and casualties that result directly from earthquake shaking.
  - The 2011 Tohoku 9.0-9.1 magnitude earthquake was the most powerful earthquake in Japan's history and was the fourth largest earthquake ever recorded. It killed nearly 20,000 people. The economic cost of this event was estimated by the World Bank as 235 billion US dollars becoming the costliest natural disaster in world history. Fig. 1.1 shows the economical impact of this tsunami in comparison with the time series of the GDP for Japan, Chile, Turkey and Italy, all of them with a history of earthquakes within their territory. It can be seen that the economical cost of Japan's 2011 tsunami is enormous. The GDP of 149 countries, out of 194

in the world, are lower than the economical cost of this tsunami as per the 2015 World Bank[6] information. The economical estimation is as large as the GDP of Chile and around one third of Turkey's GDP which are nations with intense earthquake activity. It can also be observed that the GDP of Japan decreased after 2011, which indicates that tsunamis may have indirect economical impacts delayed over time.

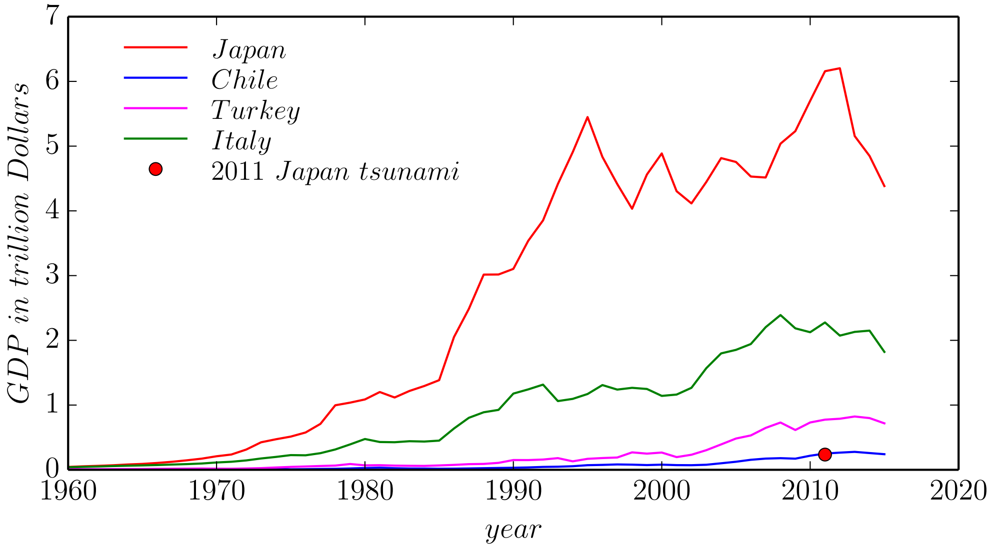

Figure 1.1: Evolution of GDP of several countries and economic impact of the 2011 Japan tsunami as reference as per the 2015 World Bank data[6].

Tsunamis can travel at about 800 km/h in open ocean. However their speed of travel decreases and their wave height increases as the water depth decreases. Hence when tsunamis approach the coast, their wave celerity decreases up to around 45 km/h and their wave height can increase drastically. This means that, for the 2004 Ocean Indian tsunami, a huge mass of moving water with tremendous force reached the facing coast as soon as 14 minutes after

---

[6] http://data.worldbank.org/indicator/NY.GDP.MKTP.CD

the earthquake.

Although earthquake magnitude is not the one only factor to evaluate the tsunami intensity, it is one of the most important ones. The energy required to displace water above the epicenter in order to create a tsunami is very large and a tsunami that could be generated by earthquakes whose magnitude is < 6.5 is very unlikely. According to USGS[7], earthquakes whose magnitudes are between 6.5 and 7.5 usually do not create dangerous tsunamis by themselves. However these kinds of earthquakes may trigger landslides that could generate tsunamis larger than the one generated by the earthquake itself. Earthquakes in the magnitude range 7.6 to 7.8 can cause locally dangerous tsunamis, but rarely affect distant coastlines hundreds to thousands of kilometers away. However, larger shocks with magnitudes exceeding 8.0 can produce destructive tsunamis at both nearby and distant coastlines.

One may think that earthquakes capable of generating tsunamis do not happen often. Fig. 1.2 shows the distribution of the number of earthquakes per year since 1990 to 2015 for magnitude ranges as per USGS[8]. As an average, 134 earthquakes between 6.0-6.9 magnitude occurred per year since 1990, 17 earthquakes between 7.0-7.9 magnitude occurred per year since 1990 and 1 earthquake of magnitude > 8 occurred per year since 1990. This indicates that an earthquake capable of producing a tsunami has happened worldwide every three months, at least in the last 25 years.

Although the damage due to earthquakes can be correlated with magnitude, tsunami height is not strongly related to the earthquake magnitude. The tsunami height is the most proper variable to estimate the tsunami damages. However tsunami height also depends on the

---

[7] https://www2.usgs.gov/faq/categories/9755/3042

[8] https://earthquake.usgs.gov/earthquakes/browse/stats.php

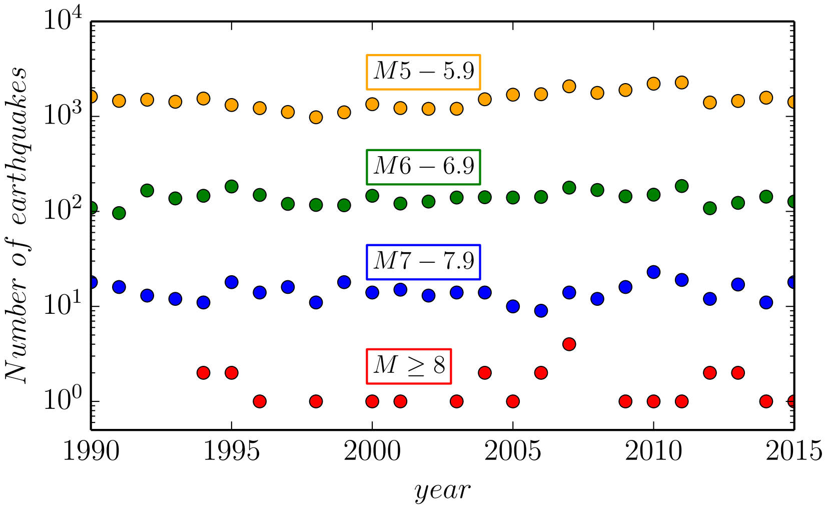

Figure 1.2: Number of earthquakes per year documented worldwide from 1990 to 2015 for four earthquake magnitude ranges. Note that the vertical axis is in logarithmic scale. Data from NGDC/WDS Global Historical Tsunami Database[9].

water depth and on the orientation of earthquake slip vector, where the reverse and normal faults are more likely to cause tsunamis compared to strikeslip faults, which is around 15 percent. Figure 1.3 depicts the earthquake magnitude versus their tsunami height from the NGDC/WDS Global Historical Tsunami Database[9] where it can be observed that there is no clear relationship between both metrics. Additionally, as the tsunami approaches the shore, the ocean becomes shallower so the height of the tsunami wave increases. Changes in coastal bathymetry and topography easies waves interactions which may increase wave heights at certain locations, for the same tsunami event.

---

[9] http://ngdc.noaa.gov/hazard/tsu_db.shtml

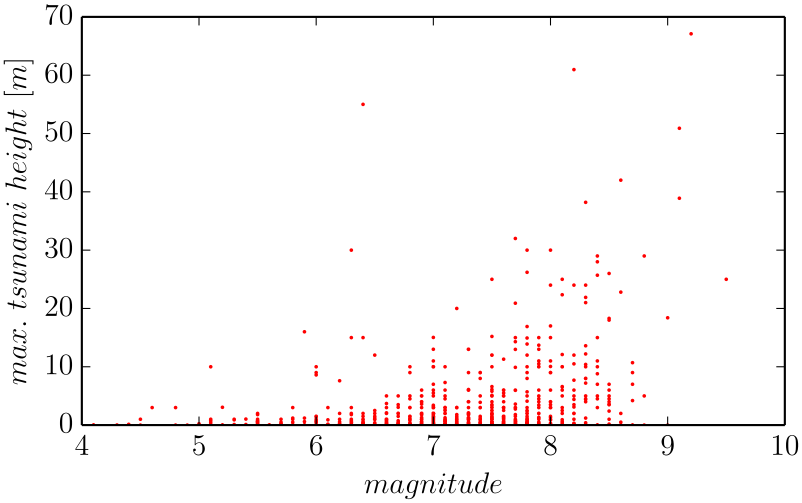

Figure 1.3: Maximum tsunami height in meters versus the earthquake magnitude according to NGDC/WDS Global Historical Tsunami Database[9].

Figure 1.4 depicts the accumulated number of tsunamis documented so far from 1700 to 2015 along with the magnitude of the earthquakes that created them. Note that rate of tsunamis is the slope of the line shown in the upper subfigure. It can be observed that the trend in the number of tsunamis changed after 1850 and also that the magnitudes of earthquakes are better known after around 1900. This does not mean that there are more tsunamis or earthquakes since 1900 but could reflect a more complete record of earthquake and tsunami events. Very often the assumption that the worst event has already happened in the past is taken into great considerations. However this assumption may not be true due to the sparseness of data before 1900 as highlighted in Fig. 1.4. We may think we know what we do not know and the worst tsunami may not have happened yet. Coastal assessments, evacuation plans and design criteria in coastal areas threatened by tsunamis should take into account worse events than those that are known.

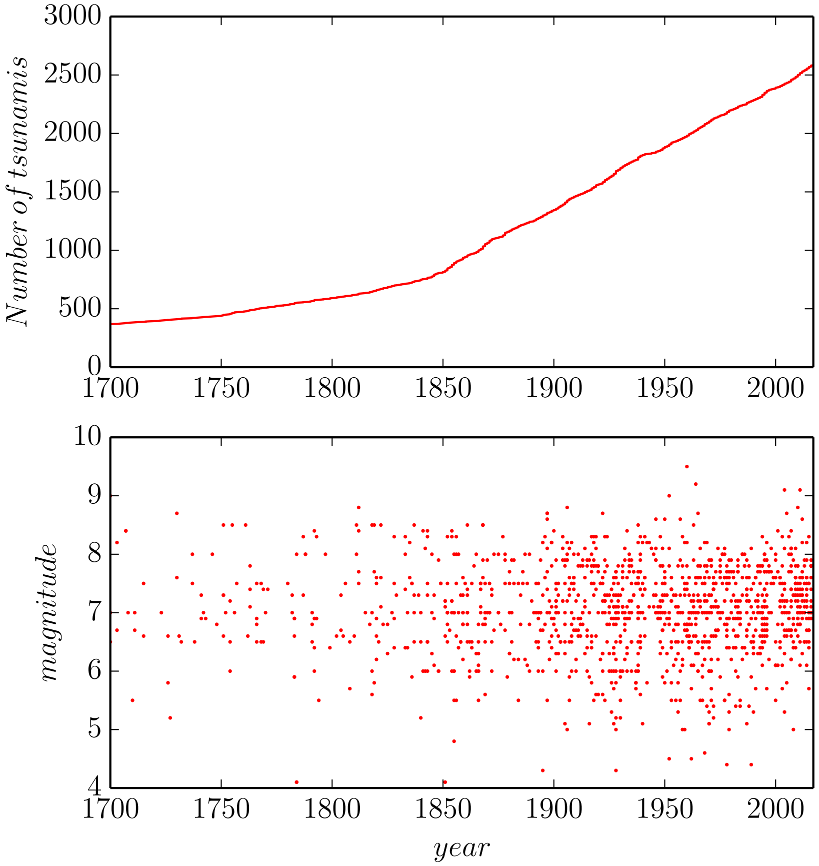

Figure 1.4: Accumulated number of tsunamis documented so far shown from 1700 to 2015 at the top. Magnitude of the earthquakes that created the tsunamis from 1700 to 2015 at the bottom. Data from NGDC/WDS Global Historical Tsunami Database[9].

1.1 Outline and Contributions

This dissertation is organized as follows:

- In chapter two, a study of numerical three-dimensional simulations of the cnoidal waves that were carried out in experiments is presented. The numerical method employed is a Lagrangian mesh-free approach called Smoothed Particle Hydrodynamics (SPH). The goal of this study is to compare the viscosity models most broadly used by the SPH users-community in order to identify which method better represents the experimental results of cnoidal waves. After comparison with experiments, analysis of averaged velocity profiles and averaged y-vorticity profiles, along with their root mean square is developed. Additionally vortexes that appear within the flow due to cnoidal waves breaking are tracked and analyzed under different tracking approaches. Results and experiment from this study is applied to the work presented in the next chapter.

- In chapter three, we analyze the breaking process of solitary waves by using the three-dimensional simulations developed with the SPH model. Validation is developed by comparison of SPH results with other experimental and numerical studies. Results from simulations are depth-averaged and we study the spatial-temporal evolution of potential energy, kinetic energy and flow momentum of the flow during breaking and wave inundation. Analysis describes the transformation from potential to kinetic energy and we observe that when the flow reaches its maximum potential energy, the flow kinetic energy is very low and vice versa. We conclude that momentum flow describes the hazard of the tsunami waves more appropriately. We also conclude that the most dangerous instant of the wave during its breaking is when the wave front reaches the shoreline, regardless of the wave amplitude. Additionally, wave front always experiences the maximum values of potential and kinetic energy and also the maximum of the flow momentum as well. This work is in-press for publication in the Journal of Waterway, Port, Coastal, and Ocean Engineering.

- In chapter four, we carry out numerical simulations based on Serre-Green-Naghdi equations (SGN) and Nonlinear Shallow Water equations (NSW) to study interaction of long waves against emerged cylinders. Cylinders are represented by numerical objects instead of numerical friction. We validate the numerical approach with velocities and water depths collected by Acoustic Doppler Velocimeters (ADV) and acoustic gauges respectively from experiments. We study the maximum values of momentum flux and water depth at the beach and observe that they may increase in some areas behind the patches of cylinders as a consequence of interactions of refractions that are generated from patches edges. This study is in review process for Marine Geology journal.

- In chapter five, motivated by the previous study, we study the effect of a vegetation barrier in reducing the runup of solitary waves using SGN and NSW equations. The vegetation is represented by a staggered distribution of emerged cylinders. Different configurations are set where we modify the barrier location, barrier width, beach slope and solitary wave amplitude. Refraction generated from the barrier edge interact with each other behind the barrier which increased the runup behind barrier. To avoid this we conclude that a minimum barrier length is required in order to achieve the maximum runup reduction that each barrier configuration could provide.

Chapter 2

Simulation of Breaking Cnoidal Waves and Eddy Evolution Using Smoothed Particle Hydrodynamics[†]

[†] **Note:** Authors, Marivela-Colmenarejo R. and Weiss R., consider that this manuscript will be submitted to a journal in the near future.

Abstract

We employ Smoothed Particles Hydrodynamics method to simulate experiments of sequence of cnoidal waves carried out in the Large Wave Flume Facility at the O.H. Hinsdale Laboratory (OSU). We compare velocity profiles between numerical simulations and experiments and also analyze the averaged velocity, vorticity and their root mean square to identify areas of high turbulence. We observe that different number and kinds of eddies appear within the flow due to the breaking process. We track the swirls so we find patterns of their trajectory, intensity, lifetime and interactions. We also conclude that particle size affects results of velocity, vorticity and swirl evolutions greatly, regardless of the viscosity model employed.

2.1 Introduction

Breaking waves have been broadly employed to study the rate of energy dissipation when the waves approach a shore. Although physical modeling has been used to study these waves, in this study we employ experiments for validation of the numerical method, which provides large amount of data for variables that are not easy to measure in experiments. We use experiments for the numerical simulation comparison and further on, we track eddies evolution during the breaking process for a better understanding of the turbulence involved in this phenomena.

Wave breaking creates turbulence which is represented by the intensity, shape and movement of the eddies as well as their evolution. The highest turbulence is located in the free surface environment when the bore collapses, which generates different patterns in the flow. This generates eddies that remain developing in the flow even after the breaking finishes.

Traditionally, grid-based methods were primarily used for solving breaking hydrodynamics. However, due to the fast and large deformations located in the breaking area, Lagrangian methods are lately becoming more appropriate to reproduce the breaking phenomenon because there is no mesh involved in the calculation. This makes these methods very convenient for reproducing splashing of breaking. Also, Lagrangian methods allow to calculate the governing equations more naturally since their particle-based approach intend to reproduce the flow more in a more realistic manner.

Smoothed Particles Hydrodynamics (SPH) is one of the most broadly extended Lagrangian methods applied in engineering. This method was first developed for astrophysical simulations by Lucy (1977), Gingold and Monaghan (1977) and it became more popular in other fields related to free surface flows since 1994 (Monaghan, 1994). This method is characterized by its simplicity for simulating free surface without almost any restrictions, which makes it very convenient for studying high turbulence flows such as breaking waves or the interaction among waves and maritime structures (Grassa, 2004) which was employed successfully in López and Marivela (2009), in López et al. (2009) and in López et al. (2011). Dalrymple and Rogers (2006) used SPH for 'waves on a beach' simulations and for 'bore-in-a-box' problems defined by Gomez-Gesteira and Dalrymple (2004). Shao (2006) applied $k - \epsilon$ model turbulence to SPH for studying cnoidal waves and compared the results with Bradford (2000) and found that turbulence is much larger in plunging waves compared with spilling waves.

We employ the GPUSPH code, which for a better performance, uses graphical processing unit (GPU) for the SPH calculations (Hérault et al., 2010). This improvement increased the speedup calculation by one to two orders of magnitude. GPUSPH also uses neighbor searching and list, which was presented in Gesteira et al. (2008). For a better understanding of the turbulence in breaking waves using SPH, Zheng et al. (2009) used a sub-grid turbulence model and an iterative solution in the Poisson's equation. Li et al. (2010) applied SPH for simulations of bores passing through bridge piers where they switched the artificial viscosity by two viscosity terms, the laminar viscosity and the SPS stress tensor obtained by Boussinesq hypothesis.

In order to determine the SPH reliability for simulating turbulence cases, Valizadeh et al. (2012) studied the decay of turbulence in fixed and rotating boxes. The decay of normalized energy using SPH is very similar to computational and experimental results shown in Robinson and Monaghan (2012), Clercx et al. (1999), Van Heijst et al. (2006) and Maassen et al. (2002).

2.2 SPH method

The SPH method is based on the interpolation of the domain by Lagrangian particles. For fluid applications, the initial distance between particles is constant and equal to the particle size, h. SPH, being a mesh-free technique, uses a kernel as interpolation function based on searching neighbors. The Navier-Stokes equations for conservation of mass and momentum are written as:

$$\begin{aligned} \frac{d\rho_a}{dt} &= \sum_b m_b (v_a - v_b) \cdot \nabla W_{ab} \\ \frac{dv_a}{dt} &= -\sum_b m_b \left(\frac{p_b}{\rho_b^2} + \frac{p_a}{\rho_a^2} + \Pi_{ab} \right) \nabla W_{ab} \end{aligned} \tag{2.1}$$

where ρ, m, v and p represent the density, mass, velocity and pressure respectively, of the fluid particle, a, with respect to its neighboring fluid particles, b. The distance between particle a and b is r_{ab}, W is the interpolation kernel function and Π represents the artificial viscosity (AR) term presented in Monaghan (1992):

$$\Pi_{ab} = \begin{cases} \dfrac{-\alpha c_s \mu_{ab} + \beta \mu_{ab}^2}{\rho_{ab}} & \text{if } v_{ab} \cdot r_{ab} < 0 \\ 0 & \text{if } v_{ab} \cdot r_{ab} > 0 \end{cases} \tag{2.2}$$

where

$$\mu_{ab} = \frac{h v_{ab} \cdot r_{ab}}{r_{ab}^2 + (0.1h)^2} \tag{2.3}$$

and c_s represents the speed of sound. For surface flows, α and β are constant parameters with values equal to 0.01 and 0 respectively. For an unsteady hydraulic jump case, López et al. (2010) assigned a different value of α to each particle depending on its vorticity and thus α was updated at each time step of calculation.

Although it has been broadly used, the AR of Monaghan (1992) does not completely describe completely the hydrodynamics of the free surface. To improve this representation, sub-particle scale (SPS) uses a similar approach to the sub-grid scale (SGS) employed in the Eulerian grid-bases Large Eddy Simulation (LES) schemes. For a complete description of the SPS viscosity model we refer to Dalrymple and Rogers (2006). SPH, as per its Lagrangian nature, requires an expression that provides pressure value to the particles as their density fluctuates. For this purpose the equation of state presented in Monaghan (1992) has been broadly used. In this way the simulated water becomes a quasi-incompressible flow by setting, $\gamma = 7$ in equation (3.4):

$$p_i = \frac{\rho_0 \cdot c^2}{\gamma}\left(\left(\frac{p_i}{p_0}\right)^{\gamma} - 1\right) \tag{2.4}$$

We use fixed boundary particles regularity distributed in the bottom and sides of the domain to represent the boundaries. The distance between boundary particles is also h. To prevent fluid particles from crossing the boundaries, boundary particles apply Lennard-Jones forces to fluid particles. If the distance between boundary particles is the same as the fluid particle size, there are irregularities in the represented boundary where fluid particles tend to stay, which generates extra numerical boundary effect. Grassa (2007) proposed to reduce the distance between boundary particles to reduce the size of the cavities so they do not hold fluid particles. Marivela and López (2011) set the boundary particle distance between two and four times smaller than h. Monaghan and Kajtar (2009) proposed to apply a kernel to the boundary particles to smooth the boundary effects which achieves more realistic numerical boundary surfaces (2.5). They suggested $d_0 = 5gH_0$ where H_0 is the still water depth and d_0 the distance up to where the kernel is apply to.

$$f(r_{ab}) = \frac{1}{\beta}\left(\frac{gH_0}{r_{ab} - d_0} W(r,h)\left(\frac{\vec{r}_{ab}}{r_{ab}}\right)\frac{2m_b}{m_a + m_b}\right) \tag{2.5}$$

2.3 Setup

Experiments were developed in the Large Wave Flume (LWF) Facility at the O.H. Hinsdale Laboratory at Oregon State University. The dimensions of the flume are 104 m long, 3.7 m wide and 4.6 m depth.

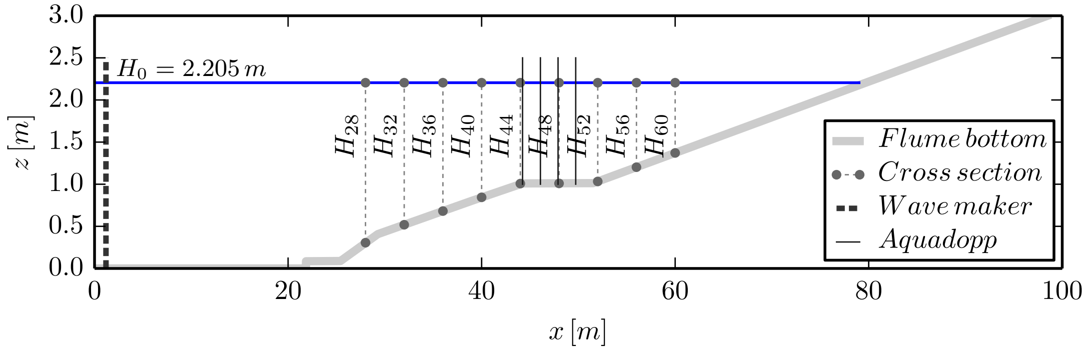

Figure 2.1: Large Wave Flume experiment setting with two main 1:24 slopes and a 7.45 m flat section in between. The amplitude of the wave maker displacement is 1.1 m and the period is 8 s. Four Nortek Aquadopps acoustic 3D profiles are located at $x_1 = 44.232$, $x_2 = 46.075$, $x_3 = 47.896$ and $x_4 = 49.723$ m to obtain data for the comparison with the numerical results. Nine cross sections from $x = 28$ m until $x = 60$ m separated by 4 m are used for numerical analysis.

The heavily instrumented LWF was custom configured for this project with a rigid concrete slab beach with 1:24 slope and a 7.45 m flat section at 1.05 m depth shown in Fig. 5.3. The piston type wave maker generated cnoidal waves with 1.1 m amplitude and 8 s period.

We carry out SPH simulations by reproducing the same conditions of experiments. We study the effect of different particle size in the swirls evolutions that develop in the flow due the breaking of the wave. The h simulated are 0.018, 0.030, 0.050, 0.060, 0.100 and 0.120 m. Boundary has been reproduced as per Monaghan and Kajtar (2009). The duration of the simulations are 120 s.

2.4 Experiments-simulations comparison

2.4.1 Velocity

We employed high resolution acoustic Doppler profilers (Nortek Aquadopp), located at x_1 = 44.232, x_2 = 46.075, x_3 = 47.896 and x_4 = 49.723 m, to obtain velocities from experiments. All Aquadopps were synchronized and measurements were recorded using high precision data acquisition system. Velocity profilers took vertical measurements at the following elevation from the bottom: 0.104 m until 0.854 m with 0.05 m increment. In Fig. 2.2 we compare the u-velocity profile averaged over time, U, between the experiments (red circles) and the numerical simulations (gray scale symbols) at the four Aquadopp locations shown in Fig. 5.3. Note that we do not consider the initial transient for averaging and we use $\sqrt{gH_i}$ to normalize U. We use the initial water depth at the Aquadopps locations, H_i, to normalize the depth, z.

In the first row of Fig. 2.2, a), corresponds to results of the simulations developed with AR (Monaghan, 1992), where $\alpha = 0.01$. The second row, b), presents results developed using SPS and the standard Smagorinsky model presented in Smagorinsky (1963) to determine the eddy viscosity. In Fig. 2.2 we also present the root mean square of $U/\sqrt{gH_i}$ with red triangles. The velocity profiles of all simulations are between the experimental values defined by $(U \pm U_{rms})/\sqrt{gH_i}$. This occurs regardless of the particle size and the viscosity model employed (AR or SPS). However the velocity profiles at x_3 and x_4, between simulations and experiments, are more different than at x_1 and x_2. Also this difference increases as the particle size decreases. Overall there are two trends of the velocity profiles. The first

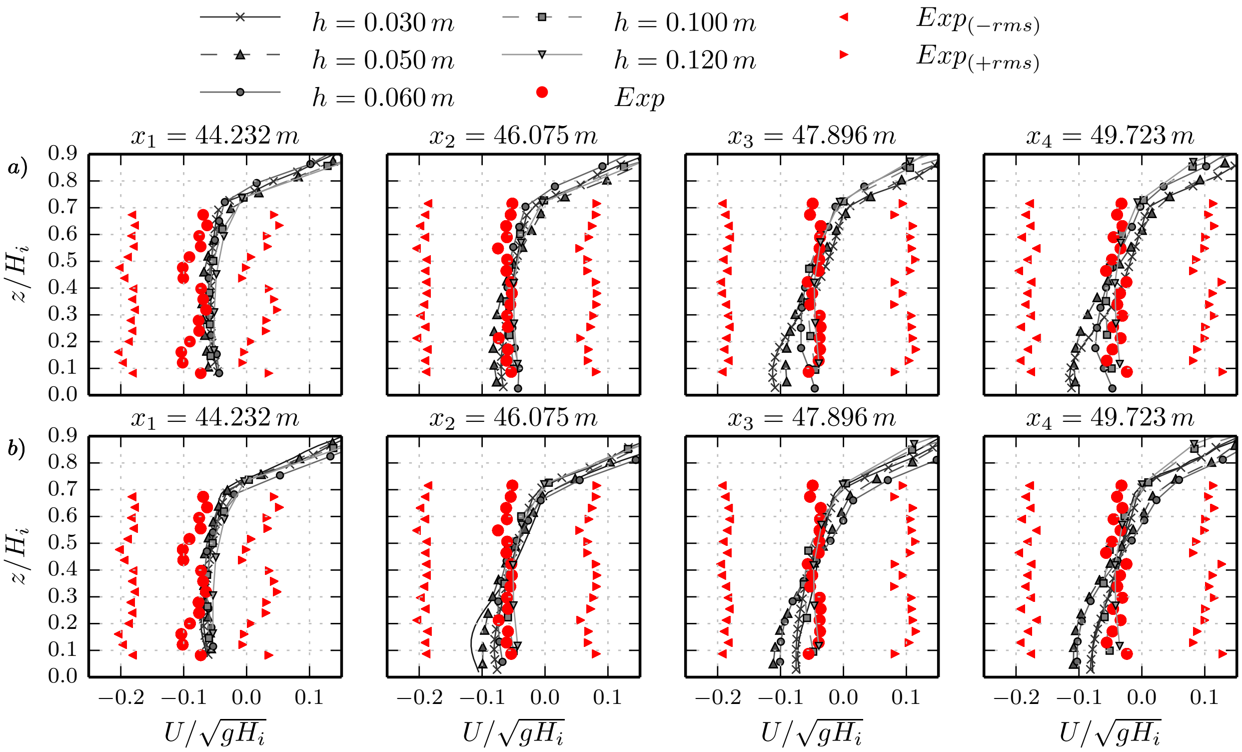

Figure 2.2: Comparison of velocity profiles averaged over time, U, at $x_1 = 44.232$, $x_2 = 46.075$, $x_3 = 47.896$ and $x_4 = 49.723$ m, between experiments and simulations for five particle sizes and with two viscosity models: Artificial viscosity (α=0.01) and sub-particle scaling ($C = 0.3$) in rows a) and b) respectively. Water depth, z, is normalized with the initial depth, H_i, at x_1, x_2, x_3 and x_4 m locations and U is normalized with $\sqrt{gH_i}$. The averaged $U/\sqrt{gH_i}$ velocity from experiments is represented with red circles and red triangles pointing towards right and left represent $(U \pm U_{rms})/\sqrt{gH_i}$ respectively. Data from simulations are represented with gray-scale colors as depending on h value.

one appears when $z/H_i < 0.7$, where the velocity profiles tend to be nearly vertical, and the second one when $z/H_i > 0.7$, where the velocity profiles increase significantly. We observe, especially at x_3 and x_4, that, as h decreases, the velocity profiles of SPS (row b) subfigures) come closer to the experiments data than the velocity profiles of AR (row a) subfigures).

In Fig. 2.3 we show the comparison of the normalized U_{rms} profiles, normalized with $\sqrt{gH_i}$, between experiments and simulations for different h values and for AR and SPS viscosity models shown in rows a) and b) respectively. As it occurs with the U profile (Fig. 2.2), there

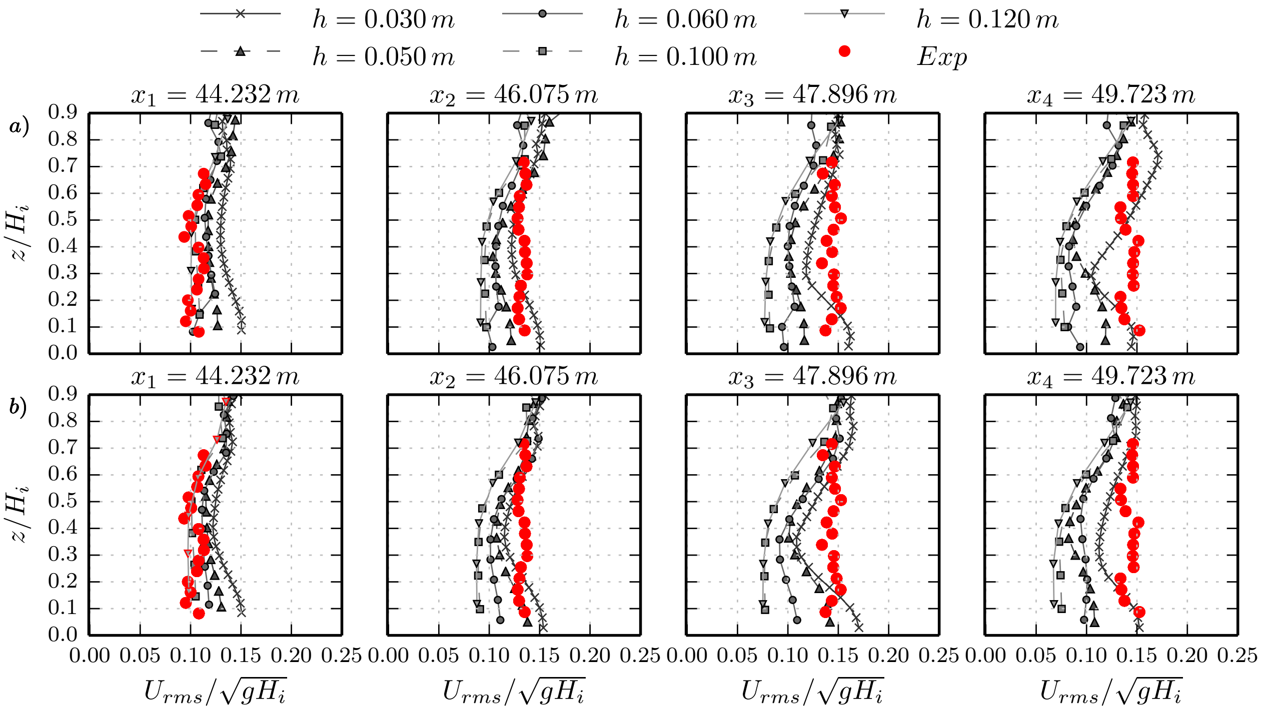

Figure 2.3: Comparison of profiles of root mean square of the velocity averaged over time, U, at x_1 = 44.232, x_2 = 46.075, x_3 = 47.896 and x_4 = 49.723 m, between experiments and simulations for five particle sizes and with two viscosity models: Artificial viscosity (α=0.01) and sub-particle scaling (C = 0.3) in rows a) and b) respectively. Water depth, z, is normalized with the initial depth, H_i, at x_1, x_2, x_3 and x_4 m locations and U_{rms} is normalized with $\sqrt{gH_i}$. Data from experiments is represented with red circles and data from simulations is represented with gray-scale colors depending on the h value.

is larger difference at of $U_{rms}/\sqrt{gH_i}$ between x_3 and x_4 compared to x_1 and x_2 m. However we observe that the U_{rms} becomes closer to the experiments measurements as h decreases at x_3 and x_4. As in Fig. 2.2, SPS better represents the experiments data in Fig. 2.3 as well. This means that, since the eddies formation depends on the vorticity, and since vorticity depends on U_{rms}, small particles sizes along the SPS viscosity model is a more appropriate numerical setup to reproduce swirls accurately.

2.4.2 Vorticity

We present in Fig. 2.4 the profiles of the time-averaged y-vorticity, Ω, at x_{1-4} locations. As in Fig. 2.2 and 2.3, the initial transient is not considered for the averaging and H_i is used to normalize z.

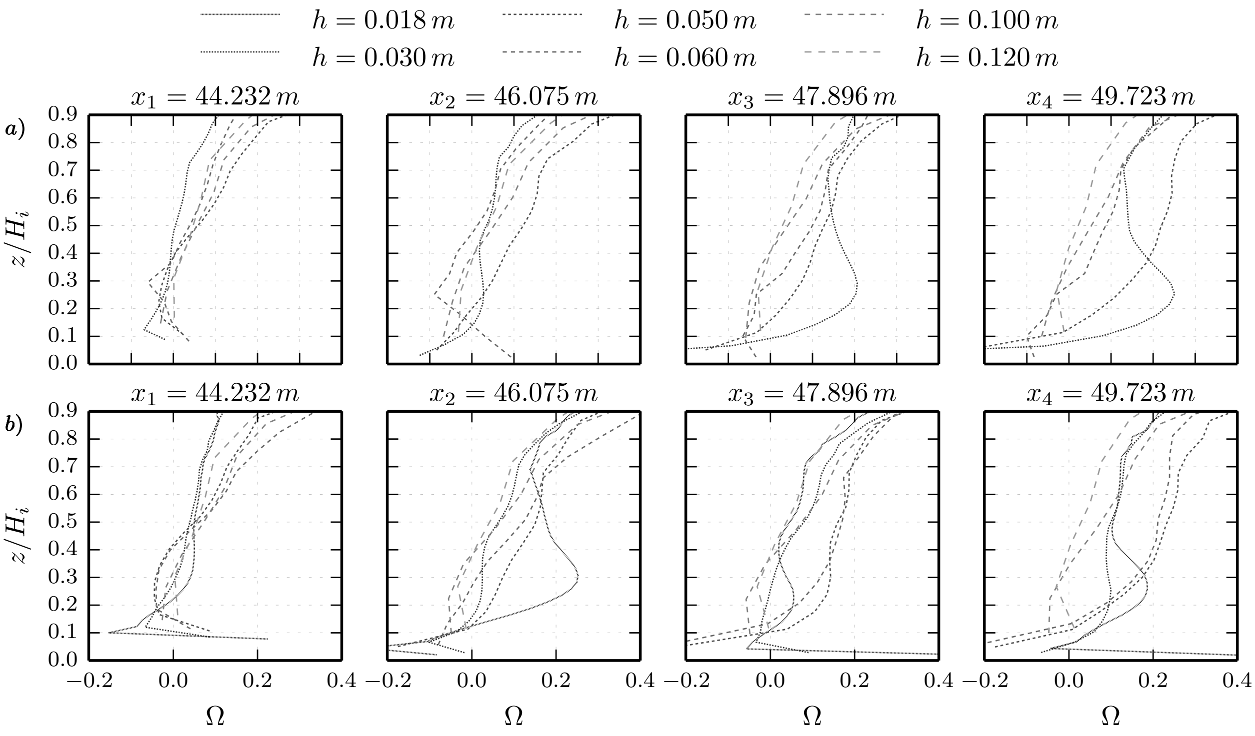

Figure 2.4: Profiles of the flow vorticity averaged over time, Ω, at x_1 = 44.232, x_2 = 46.075, x_3 = 47.896 and x_4 = 49.723 m, from simulations with six particle sizes and with two viscosity models: Artificial viscosity (α=0.01) and sub-particle scaling (C = 0.3) in rows a) and b) respectively. Water depth, z, is normalized with the initial depth, H_i, at x_1, x_2, x_3 and x_4 m locations.

Although small values of h are needed to simulate the swirls evolution correctly, a convergence of the results in the viscosity model as h decreases is also required. As expected, Ω increases as h decreases overall. However there is a larger convergence of the Ω profiles at x_3 and x_4 for SPS compared to AR. For instance, note at x_4 that the difference of the Ω profiles between h = 0.030 and 0.050 m of AR is slightly larger than the difference of the Ω profiles between

$h = 0.018$ and 0.030 m for SPS. This indicates a slightly larger numerical convergence of the SPS viscosity model compared to AR, which makes SPS more adequate to develop swirls tracking of the flow under breaking sequence of cnoidal waves.

2.5 Analysis of simulations

In this section we show results of velocity, vorticity and their rms from numerical simulations carried out with the SPS viscosity model. The data is obtained from the nine regularly distributed cross sections at each 4 m located between $x = 28$ and 60 m and depicted in Fig. 2.1. We also study the variations of these variables along the tank length.

2.5.1 Velocity

By analyzing velocity profiles at different locations we obtain their evolution along the tank and as function of the particle size as well. Bore collapse occurs before $x = 40$ m so the first three locations, $x = 28$, 32 and 36 m, analyze the flow before the waves break. The next three locations, placed on the flat area at $x = 40$, 44 and 48 m, analyze the main turbulence generated due the breaking. The last three locations, sited on the second slope at $x = 52$, 56 and 60 m, study the turbulence associated to secondary breakings.

Since the breaking of the simulated cnoidal waves generate very turbulent flow, we averaged the velocity profiles to better analyze the velocity profile patterns. Figure 2.5 shows the $U/\sqrt{gH_i}$ along depth of the numerical simulations for the six particle sizes at aforementioned nine locations where H_i is their initial water depth shown in Fig, 2.1. At $x = 28$, 32 and 36

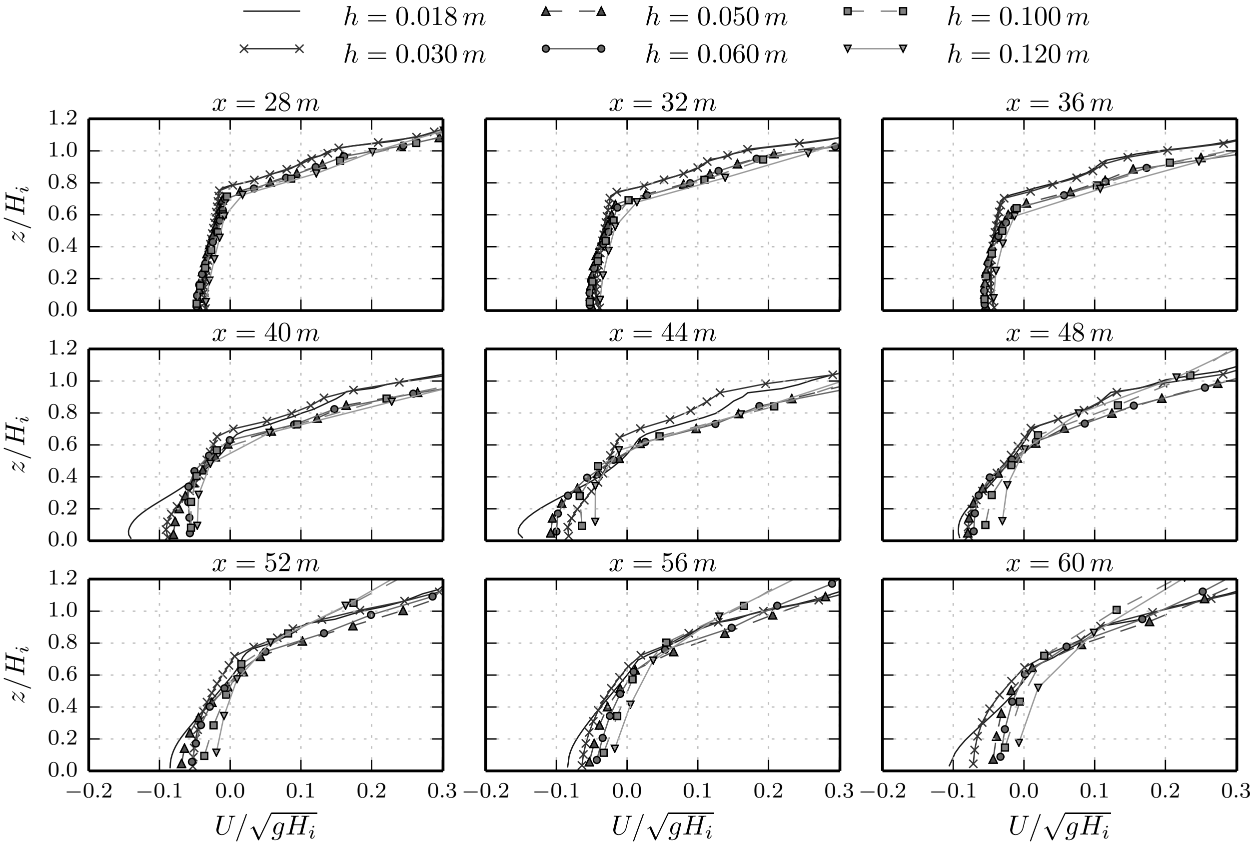

Figure 2.5: Nine i profiles of velocity averaged over time, U, at $x = 28 - 60$ m each 4 m from simulations for six particle sizes and with the sub-particle scaling viscosity model ($C = 0.3$). Water depth, z, is normalized with the initial water depth, H_i, at each respective locations and U is normalized with $\sqrt{gH_i}$. Particle sizes are represented with different symbols and line styles.

m locations, the averaged velocity profiles take very similar shape regardless of the h values. The profile shape has two trends: The first one occurs when $z/H_i < 0.7$ and $U/\sqrt{gH_i} < 0$. The second trend occurs when $z/H_i > 0.7$ and $U/\sqrt{gH_i} > 0$. This indicates the effect of the wave on the upper layer of the flow when it approaches the shoreline before its breaking. However, at $x \geq 40$ m locations in Fig. 2.5, the change at $z/H_i \sim 0.7$ becomes smoother and the velocity profiles become more homogeneous with only one general trend. This is because the bore collapse occurs between $x = 36 \sim 40$ m and the effects of its breaking propagate deeper within the flow. Despite the presence of only one trend of the velocity profiles when

$x \geq 40$ m, there are differences between them as h decreases, especially at $x = 40$, 44 and 60 m locations. This indicates that small h simulations represent this complex phenomenon more accurately. However, except at $x = 40$, 44 and 60 m, $h = 0.018$ m would not be necessary because a clear convergence occur in the velocity profiles as h increases.

We observe that the flow close to the boundaries is less affected by boundary effects as h decreases, which contributes to higher accuracy. Moreover, small particles located in the free surface environment are more able to accurately represent velocities as h decreases, which is relevant during breaking and bore collapse. These reasons additionally explain why numerical setup with small particles are more convenient to simulate this complex hydrodynamics. When $h = 0.120$ and 0.100 m, fluid particles do not accurately represent velocity values and also they are too big to reproduce bore collapse and splashing adequately. This can be seen when $z/H_i > 0.7$ and for $x \geq 40$ but especially at $x = 40$ and 44 m.

Figure 2.6 shows U_{rms}, root mean square of U. Overall we observe that when $z/H_i > 1$, the values of U_{rms} differ from simulations with different h. This is because the number of particles sampled over $z/H_i \geq 1$ is very less compared with the number of particles sampled when $z/H_i < 1$. Despite this, all the profiles of $U_{rms}/\sqrt{gH_i}$ follow a common trend with a smooth transition at $z/H_i \sim 0.7$. This transition is smoother than the one observed of $U/\sqrt{gH_i}$ when $z/H_i \sim 0.7$ in Fig. 2.5. However, there is a clear dependence of the profile of $U_{rms}/\sqrt{gH_i}$ on h, especially at $x = 40$ and 44 m locations where, for instance, the profiles of $h = 0.018$ m get larger than the profiles of $h \geq 0.30$ m. At these locations, breaking process generates more random eddies pattern for smaller particle sizes. This indicates that small particles are more capable to reproduce turbulence more accurately. Hence *rms* analysis is very important to simulate swirls properly as we pointed out in the previous section.

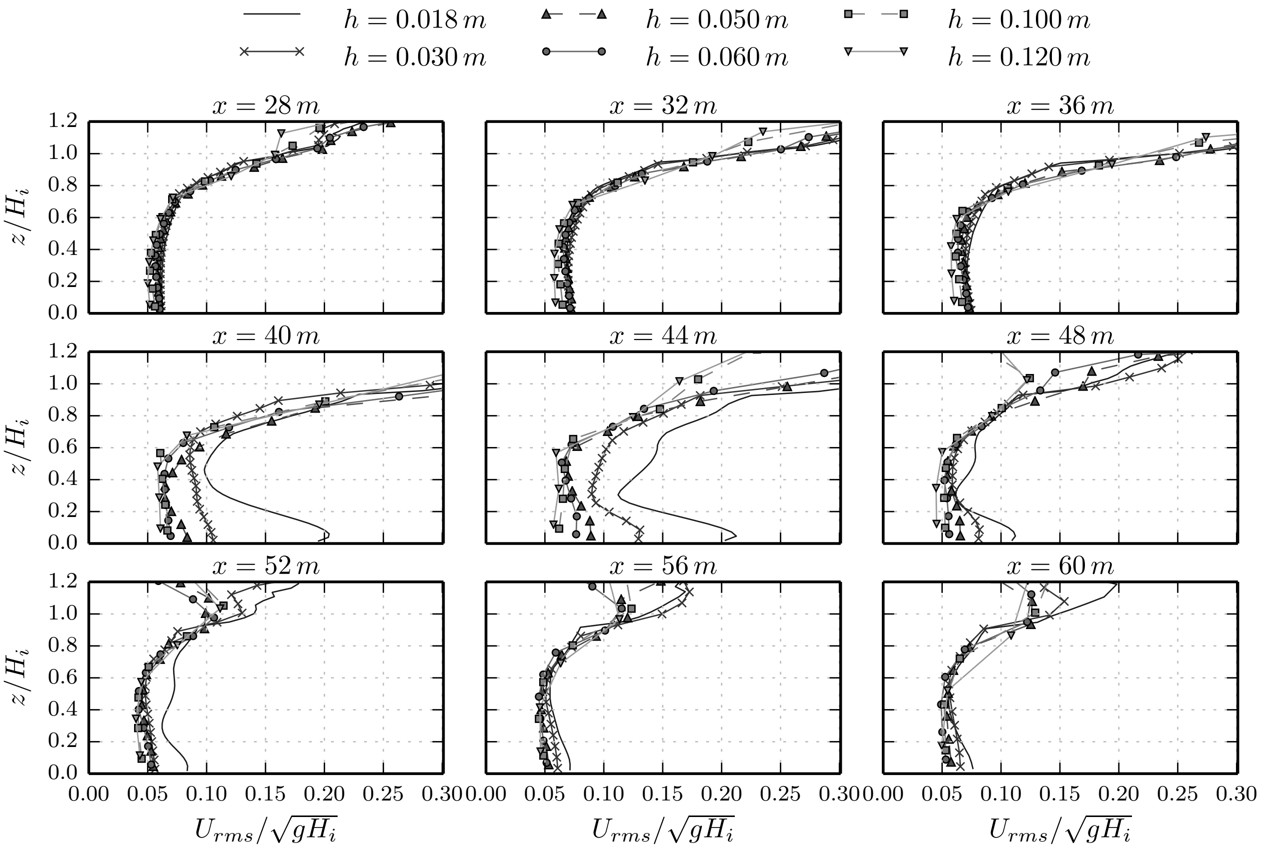

Figure 2.6: Nine profiles of the root mean square of the velocity averaged over time, U, at $x = 28 - 60$ m, at each 4 m, from simulations for six particle sizes and with the sub-particle scaling viscosity model ($C = 0.3$). Water depth, z, is normalized with the initial water depth, H_i, at each respective locations and U_{rms} is normalized with $\sqrt{gH_i}$. Particle sizes are represented with different symbols and line styles.

At locations $x = 40$ to 52 m and for $h = 0.018$ m simulations, the lower part of the $U/\sqrt{gH_i}$ profiles increase significantly. This indicates that Monaghan and Kajtar (2009) boundary representation does not add numerical roughness to the flow, which indicates the suitability of the boundary representation employed.

We present the longitudinal velocity, vel, and its root mean square, vel_{rms}, in Fig. 2.7a and 2.7b respectively. Both, vel and vel_{rms}, are averaged over depth and simulation time.

The measures are taken at 0.5 m increment along the tank length. We observe that *vel* longitudinal profiles are very similar regardless of the particle size for $x < 17$ m. However, differences appear from where the tank bottom changes at $x \geq 22$ m. Differences increase as the effect of the beach slope increases. Overall *vel* increases as h decreases. However the difference of *vel* between $h = 0.018$ and 0.030 m simulations are very small, which indicates that the velocity convergence mentioned in the cross sections is also valid for a longitudinal analysis as h decreases.

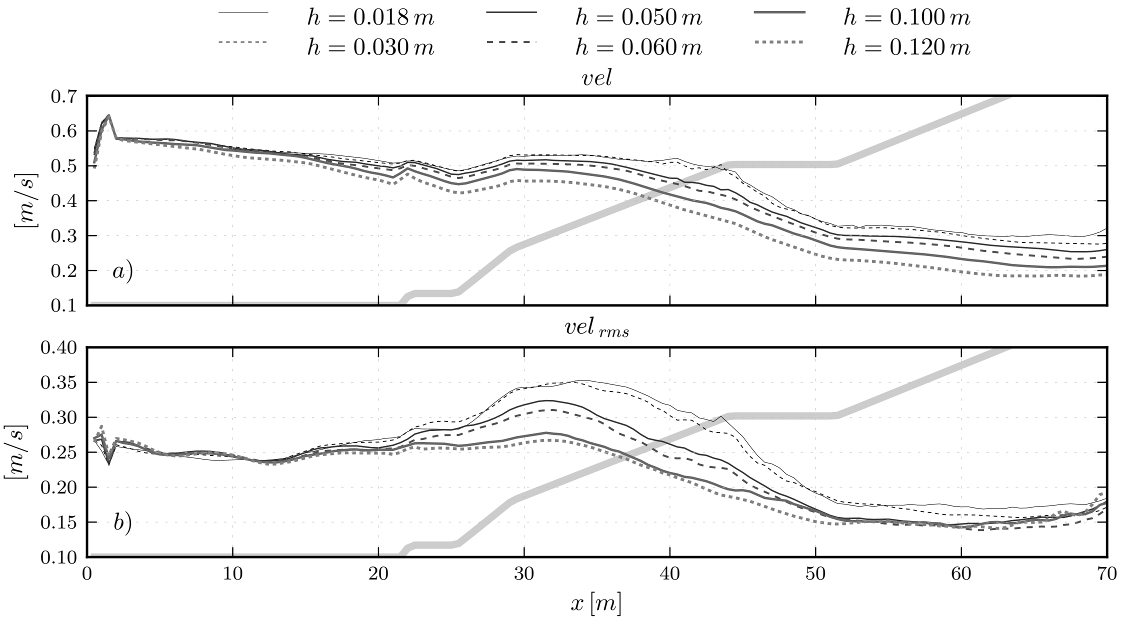

Figure 2.7: a) Longitudinal velocity averaged over depth and time, *vel*. b) Longitudinal root mean square of the velocity averaged over depth and time, vel_{rms}. The six particle sizes are represented with different line styles. The bottom of the tank is sketched as reference with gray and thick line.

The longitudinal profiles of vel_{rms} along the tank, Fig. 2.7.b, are similar when $x < 17$ m regardless of the h value. However they differ considerably as h decreases for $x \geq 17$ m. Despite the differences, vel_{rms} of $h = 0.030$ and 0.018 m are very similar, which also indicates the presence vel_{rms} convergence along the flume when $h \leq 0.030$ m as it happened with *vel*. As observed in the cross sections, vel_{rms} is more sensitive to variations of h than *vel*, which as we mentioned, is more important to eddies analysis. Note that boundary effects are not observed in the longitudinal profiles of vel nor vel_{rms}.

2.5.2 Vorticity

We present in Fig. 2.8 the profiles of the y-vorticity averaged over time, Ω, at the same cross sections where we study U and U_{rms} and shown in Fig. 5.3. The Ω profiles are similar to each other when $x \leq 36$ m which are locations before the breaking. At this locations Ω decreases as h decreases as well. However, during and after the breaking, at $x \geq 40$, we observe that Ω becomes very sensitive to h variations and profiles differ to each other significantly and they also take different shapes, especially at $x = 40$, 44 and 48 m. At these locations Ω increases rapidly for $z/H_i < 0.55$ and reaches a peak when $z/H_i \sim 0.25$ for $h = 0.018$ m. Note that this also happens at $x = 60$ m. Although depth is normalized, the Ω peak at $z/H_i \sim 0.25$ does not change at these locations which indicates that this is depth where the flow is most turbulent at.

In general, there is mesh dependence for reproducing vorticity accurately. For instance, although $h = 0.030$ m simulation reproduces turbulence, it is not able to reproduce vorticity fluctuations as accurate as the $h = 0.018$ m simulation does. In the Ω analysis it becomes more difficult to identify convergence as easy as it is for U and U_{rms}.

Figure 2.9 shows the profile of Ω_{rms}, root mean square of Ω, at the cross sections locations shown in Fig. 5.3. There is also a high dependence on h. However, despite this dependence, Ω_{rms} increases rapidly for $z/H_i < 0.55$ and reaches peaks when $z/H_i \sim 0.25$ for $h = 0.018$ m

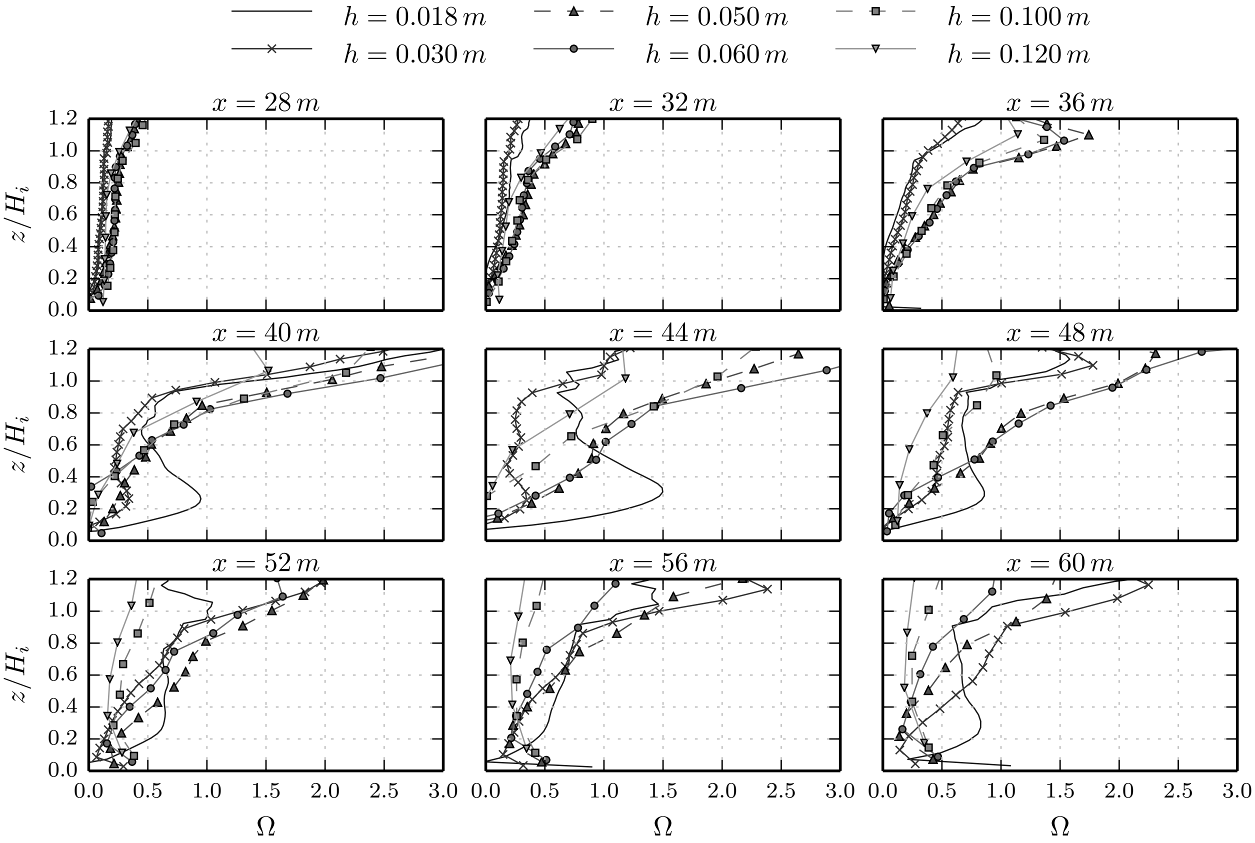

Figure 2.8: Nine profiles of the vorticity averaged over time, Ω, at $x = 28 - 60$ m, at each 4 m, from simulations for six particle sizes and with the sub-particle scaling viscosity model ($C = 0.3$). Water depth, z, is normalized with the initial water depth, H_i, at each respective locations. Particle sizes are represented with different symbols and line styles.

at $x \geq 40$ m as happened with Ω. In fact, Ω_{rms} profiles are very similar to the Ω profiles. Overall Ω_{rms} is larger than Ω which indicates the turbulence at $z/H_i \sim 0.25$ is very high.

The longitudinal profile of the y-vorticity, $vor(y)$, and its root mean square, $vor(y)_{rms}$, both averaged over depth and over simulation time, are shown in Fig. 2.10.a and b respectively for different values of h. The bore collapse happens around $x = 36 \sim 40$ m and so $vor(y)$ tends to be similar for $x < 36$. However when $x \geq 40$ m, $vor(y)$ becomes larger as h decreases. The $vor(y)$ of $h = 0.120$ and 0.100 m are low and hence they cannot reproduce the internal eddies associated with the breaking process accurately. However, for the $h \leq 0.060$ m cases, their

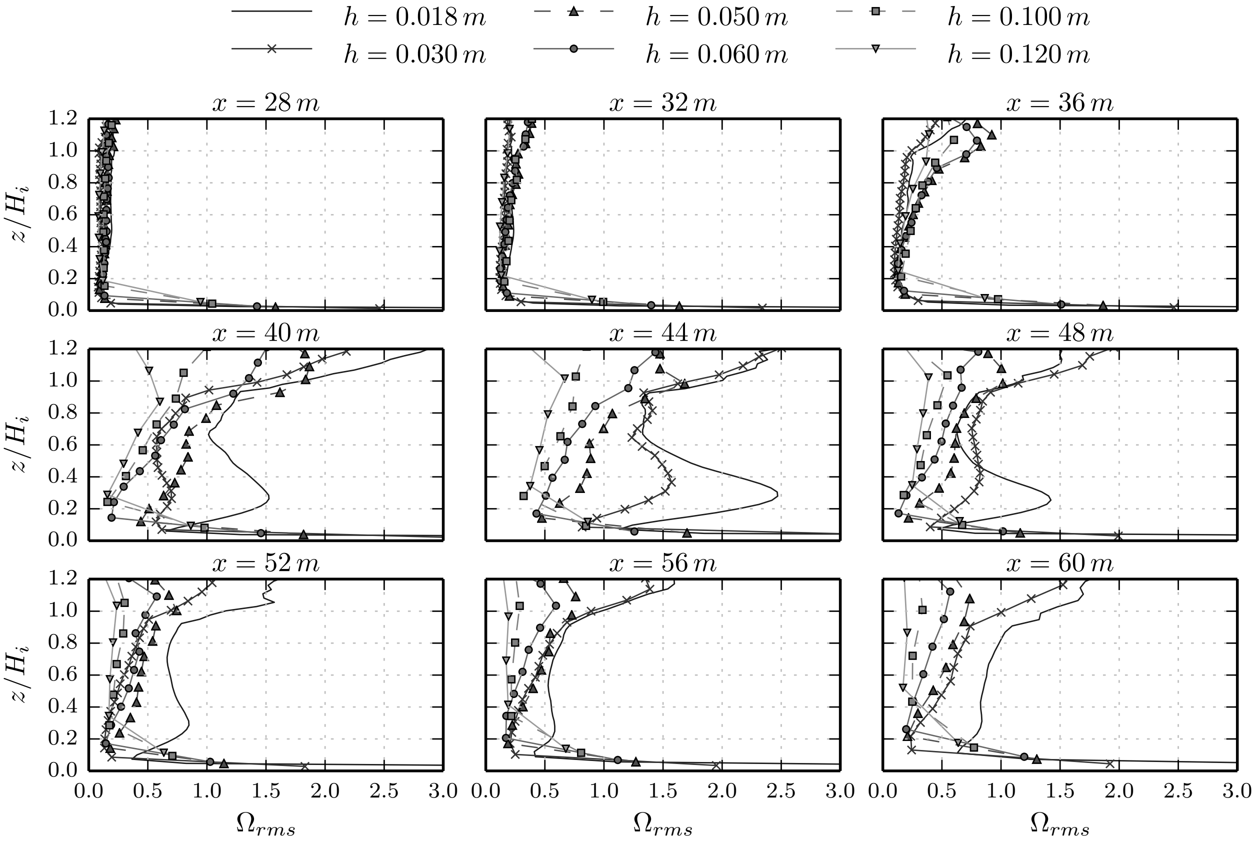

Figure 2.9: Nine profiles of the root mean square of the vorticity averaged over time, Ω, at $x = 28 - 60$ m, at each 4 m, from simulations for six particle sizes and with the sub-particle scaling viscosity model ($C = 0.3$). Water depth, z, is normalized with the initial water depth, H_i, at each respective locations. Particle sizes are represented with different symbols and line styles.

$vor(y)$ takes similar values with some fluctuation after $x \sim$ 45-55 m. This is because the $0.018 \leq h \leq 0.050$ simulations reproduce the flow variations due to the breaking. We observe that $vor(y)$ takes high values for $h = 0.018$ m when $x > 55$ m. This is because $h = 0.018$ m is capable to reproduce the flow variations close to the shoreline, where the depth becomes smaller. Additionally small particles have larger suitability to represent the eddies correctly since the $vor(y)_{rms}$ in Fig. 2.10.b tends to decrease as h decreases, except at $x = 38 \sim 49$ m where $vor(y)_{rms}$ increases as h decreases. This indicates that small particles are more capable of representing the variations of $vor(y)$ more accurately.

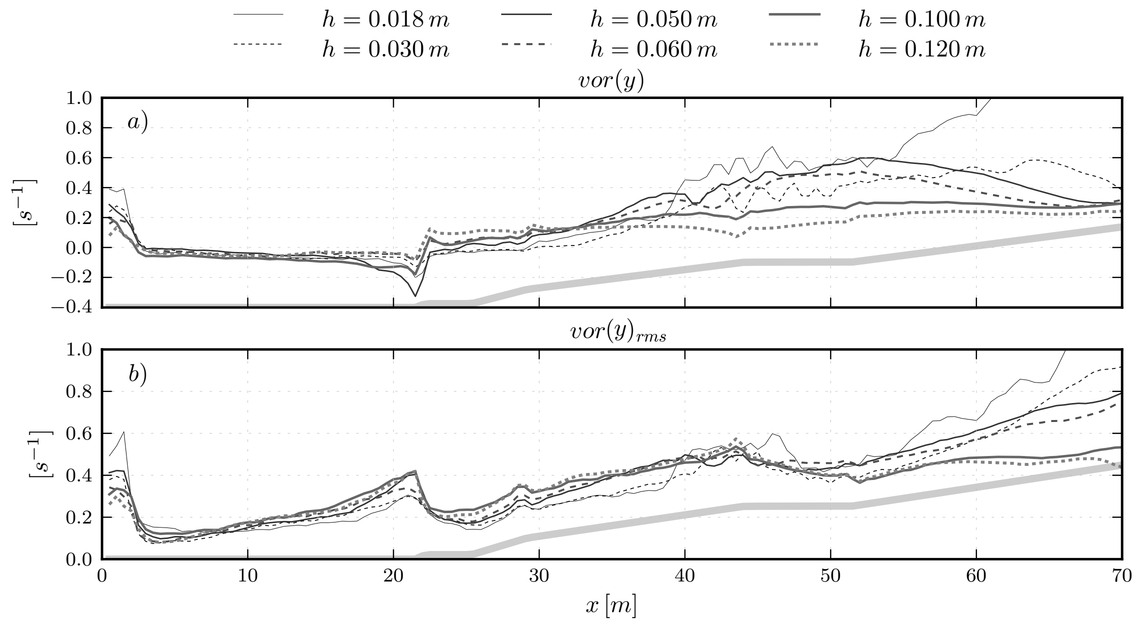

Figure 2.10: a) Longitudinal vorticiy averaged over depth and time, $vor(y)$. b) Longitudinal root mean square of the velocity averaged over depth and time, $vor(y)_{rms}$. The six particle sizes are represented with different line styles. The bottom of the tank is sketched as reference with gray and thick line.

2.5.3 Swirls evolution

From the analysis of the previous figures, we observe that h = 0.018 and 0.030 m are the more suitable particle sizes to study the evolution of swirls due to the hydrodynamics effects of the breaking inside the flow. Figure 2.11 shows the instantaneous y-vorticity, $vorticity(y)$, for simulations with h = 0.018 m (left column) and h = 0.030 m (right column). Rows correspond with timesteps, t = 17, 25, 33, 41 and 89 s presented from top to bottom respectively. We observe that the internal eddies differ among timesteps for both columns. This is because the after breaking effects not only depend on the piston movement, but also on the hydrodynamics conditions remaining from the previous cnoidal wave breaking. For the same timesteps, there are large differences in the number and distribution of eddies between different h. This is because $h = 0.018$ m simulation is able to reproduce small swirls during the during and after the breaking process.

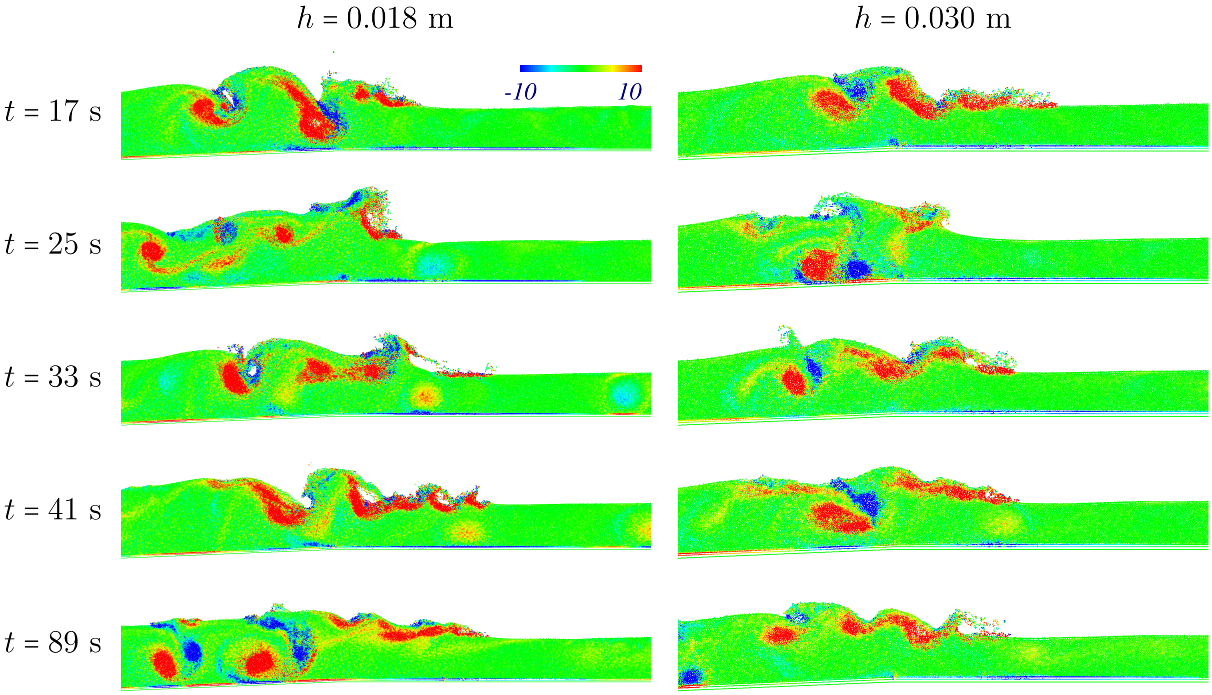

Figure 2.11: Comparison of instant *vorticity*(y) between $h = 0.018$ m and $h = 0.030$ m simulations at x between 40 and 50 m and at $t = 17$, 25, 33, 41 and 89 s timesteps. Note the difference between timesteps are multiple of the period ($T = 8$ s). There is better swirls tails definition for $h = 0.018$ m.

We observe that stability and lifetime of the eddies are larger for $h = 0.018$ m than for $h = 0.030$ m. This simulation is more able to reproduce more splashing in the water surface which develops additional swirls creating extra differences. Vortex evolutions are also better defined for $h = 0.018$ m due to the presence of eddies tails. These tails interact with other tails and eddies so hydrodynamics gets more complex as h decreases.

Overall, although the difference of the free surface is not very large for different values of

h, we observe much larger differences within the flow as h decreases. To illustrate this observation, we show in Fig. 2.12 the number of swirls in log_{10} scale that each simulation is able to reproduce versus the intensity of the eddies. We observe that as h decreases, the number and the vorticity of the eddies increase significantly. For instance, for the $h = 0.120$ m simulation, there is no particle whose $vorticity(y) > 21$ s^{-1}. This means that there is a strong limitation in reproducing high turbulent flows and their associated swirls accurately by using large h.

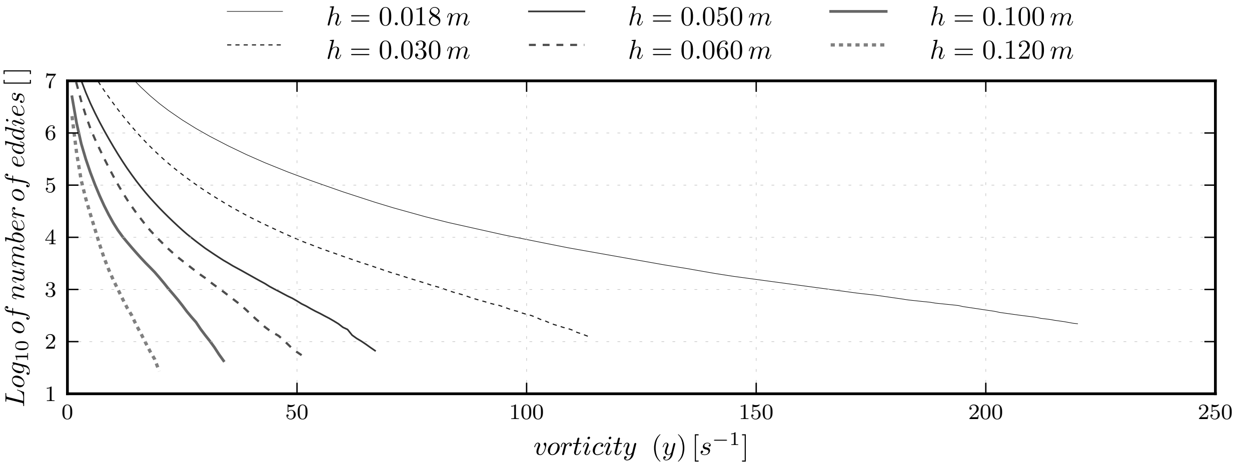

Figure 2.12: Logarithm$_{10}$ of sum of all particles which have a $vorticity(y)$ higher than shown in x-axis. The sum is carried out for all timesteps (40 per second) in the whole time simulation. Notice that simulations with larger particle sizes are not able to reproduce high $vorticity(y)$.

Although there is a strong dependence of the swirls formation on h, we track the swirls formed due to the breaking and and show their evolution in Fig. 2.13, 2.14 and 2.15. For a better representation of the swirls patterns in these figures, we only present the swirls whose $vorticity(y) \geq 10$ s^{-1} clockwise and ≤ 10 s^{-1} anti-clockwise.

To track the swirls we set a fixed grid of cells. We use the particles contained in each cell to average the vorticity in each cell. To have a clear vortex representation, the most appropriate cell size is $1.5h$ for $h = 0.050$ and 0.030 m and $4h$ for $h = 0.018$ m. If the cell size is larger than the aforementioned values, the number of studied eddies is very low for $h = 0.050$ m and the precision for tracking swirls decreases for $h = 0.018$ m. If the cell size are smaller than the aforementioned values, the number of swirls becomes too large it is difficult to find swirls evolution trends for $h = 0.018$ m.

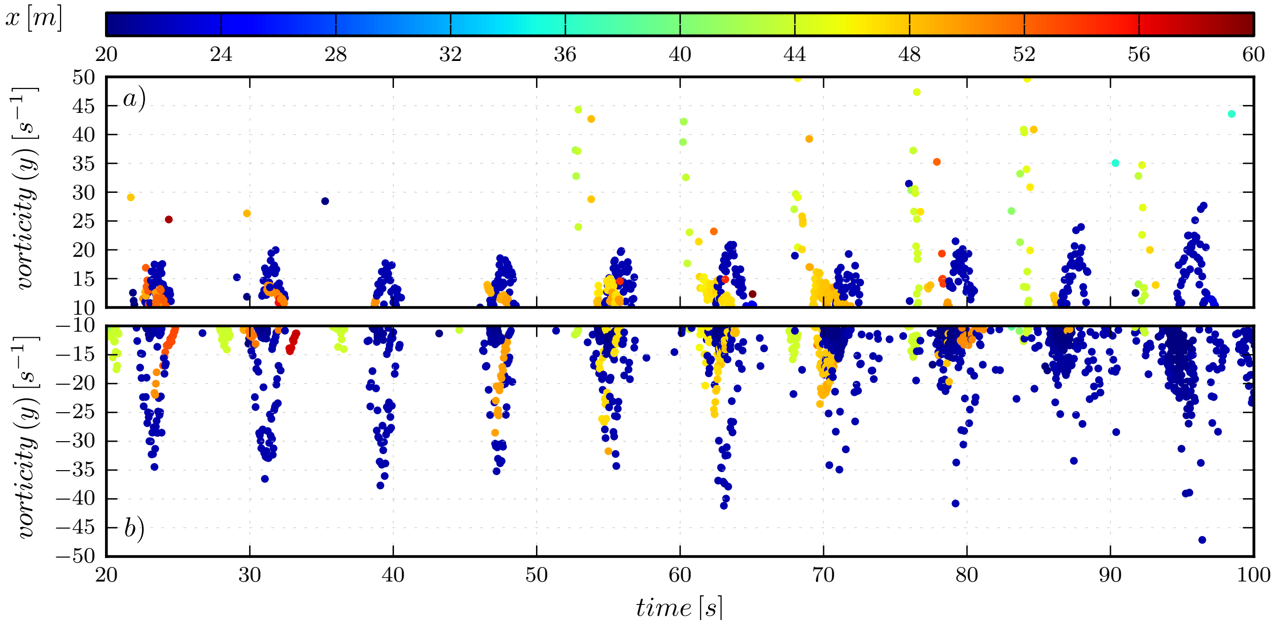

Figure 2.13: Swirls evolution for $h = 0.050$ m simulation over a $1.5h$ cell size grid averaging. a) Clockwise swirls. b) Anti-clockwise swirls. The color map represents the x locations of the eddies. Note that there are anti-clockwise swirls and clockwise swirls at $x = 22$ m with a delay of approximate 2 s. The anti-clockwise gets larger with the time. Clockwise swirls are located at $x = 40$ and 46 m.

Figures 2.13a and b show the time evolution and the $vorticity(y)$ of the clockwise and anti-clockwise swirls respectively for the $h = 0.050$ m simulation. There are clockwise and anti-clockwise eddies at $x \sim 22$ m in each cycle. These eddies get larger as the simulation progresses. When $t > 50$ another set of swirls appear at $x \sim 40$ m which can reach $vorticity(y) = 45$ s^{-1}. Although they are unstable and decay fast, their appearance is constant. This $h = 0.050$ simulation is not able to reproduce breaking effects for long so there is only a weak anti-clockwise vortex located around $x = 32$ m with $vorticity(y) = -15$ s^{-1} approximately. Overall, in this figure we observe that $x \sim 22$ m is the location where steady clockwise and anti-clockwise swirls appear. This is consistent with the variations of $vor(y)$ and $vor(y)_{rms}$ observed at $x \sim 22$ m in Fig. 2.10a and b respectively. Eddies located at $x > 25$ m are unsteady.

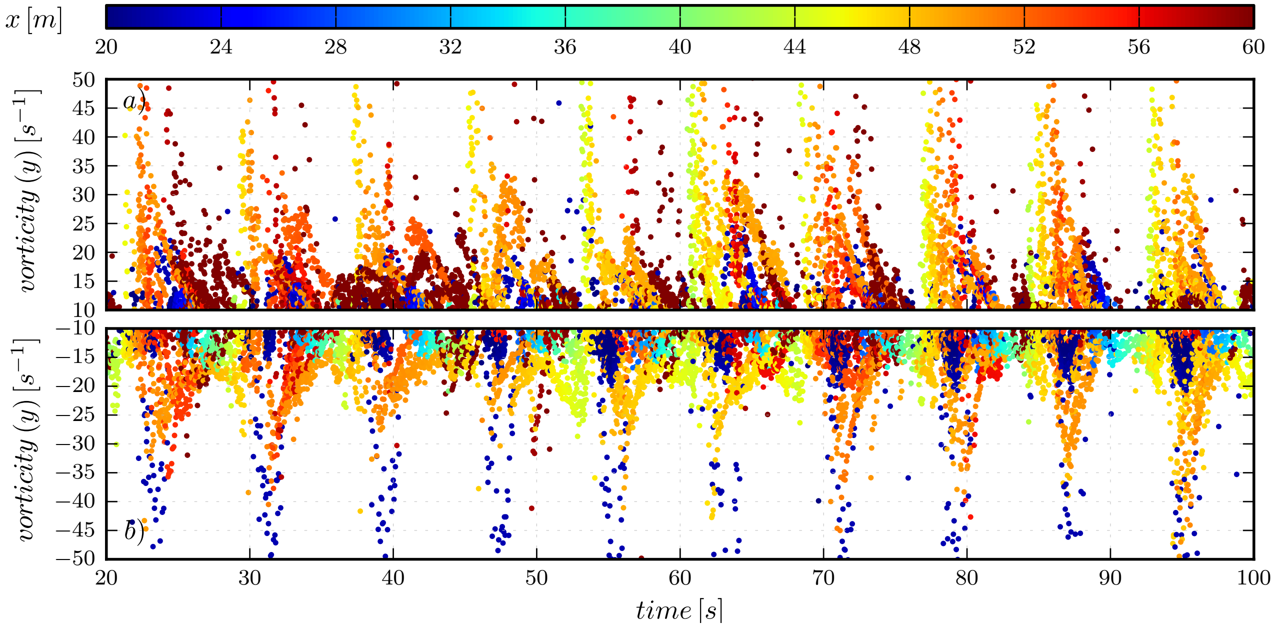

Figure 2.14: Swirls evolution for $h = 0.030$ m simulation over a $1.5h$ cell size grid averaging. a) Clockwise swirls. b) Anti-clockwise swirls. The color map represents the x locations of the eddies. Eddies produced because secondaries breaking appear at $x > 48$ m.

A more detailed study is carried out by analyzing $h = 0.030$ m simulation. Fig. 2.14a and b show the clockwise and the anti-clockwise swirls respectively. We observe that the anti-clockwise swirls located at $x \sim 22$ m are more intense, while the vorticity of the clockwise swirls approximately keep their values compared with $h = 0.050$ m simulation. We also observe that there are clockwise swirls whose $vorticity(y)$ reaches 50 s^{-1} located at $x \sim 40$ m and anti-clockwise swirls with about 2 s of delay whose $vorticity(y)$ is around -30 s^{-1}. Also there are other clockwise swirls around $x \sim 46$ m with a delay of up to 2 s approximately with respect to the anti-clockwise swirls. Additionally there are extra clockwise swirls at $x \sim 48$ and $x \sim 60$ m but they do not follow a clear pattern. Overall Fig. 2.14 shows that the main breaking creates a more clear sequence of eddies represented with good regularity and intensity.

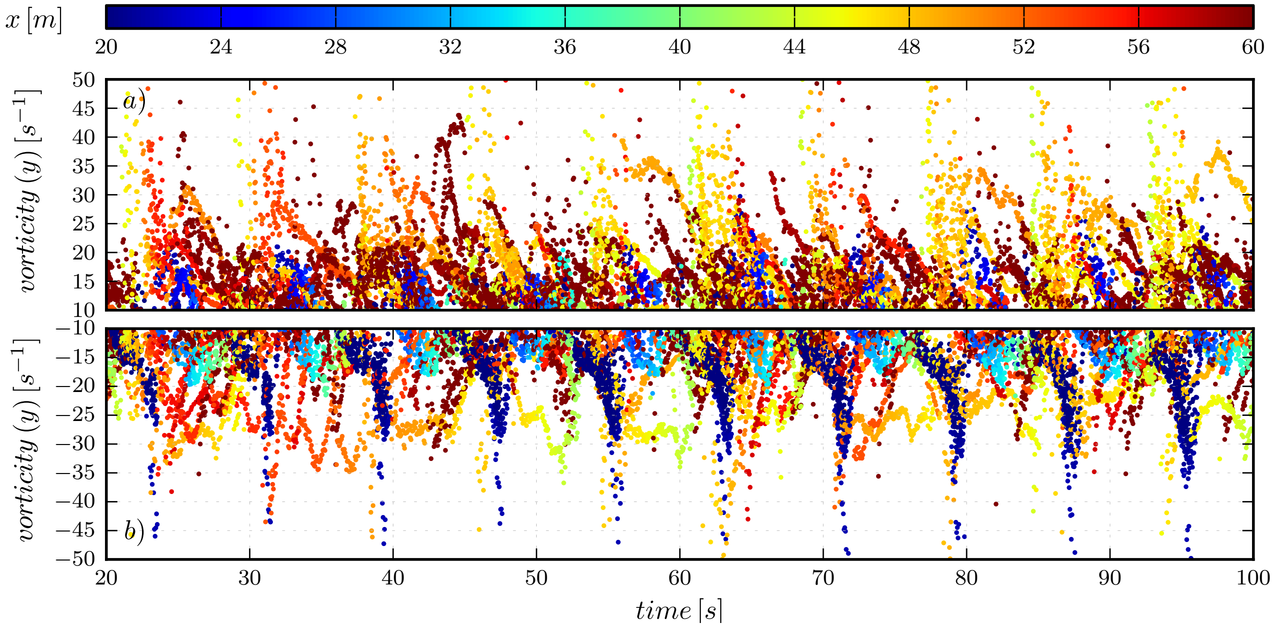

Figure 2.15: Swirls evolution for $h = 0.018$ m simulation over a $4h$ cell size grid averaging. a) Clockwise swirls. b) Anti-clockwise swirls. The color map represents the x locations of the eddies. Note that $t > 52$ s eddies formed are more homogeneous pattern.

The same analysis becomes more complicated for $h = 0.018$ m simulation. In this case, Fig. 2.15a and b, show the existence of many small swirls located at $x \sim 60$ m and, as shown in Fig. 2.13 and 2.14, the anti-clockwise swirls also appear at $x \sim 22$ m.

Some of the anti-clockwise swirls reach a $vorticity(y)$ of -50 s^{-1}, however, many of the anti-clockwise swirls have a $vorticity(y) < -25$ s^{-1}. These swirls are very steady and located at $x = 40\text{-}44$ m. Note that the flow does not have a homogeneous turbulent pattern from $t = 20$ to 53 s in the clockwise eddies. When $t \sim 50$ s the flow has a very high amount of turbulence.

After that, the flow turbulence takes a more homogeneous behavior. Although $h = 0.018$ m discretization is able to catch more swirls, their intensity is not higher than the swirls caught with the $h = 0.030$ m discretization. In general $vorticity(y)$ is larger in clockwise swirls when compared to anti-clockwise swirls, which agrees with results shown in Fig. 2.10. This is due to the larger number of swirls and their large vorticity.

2.6 Conclusions

We analyze the reliability of SPH method to simulate cnoidal waves generated by wave maker. The domain studied has two main slopes with a flat section between them. After comparing numerical results with experiments, we average over time the velocity and vorticity, along with their root mean square (rms), and we study their profiles along the depth at four cross sections. Additionally we average over time and depth the velocity, vorticity and their rms along the tank length. Additionally we track the swirls to investigate patterns in the swirls evolution.

We conclude that there is sensitivity in the SPH results as there are differences in the velocity and vorticity depending on the size of the SPH particles, h. This is because remnant hydrodynamical conditions of the previous cycle highly influences the flow condition of the incoming cycle. Hence there are significant differences in the hydrodynamics of the flow between the cnoidal waves in all the simulations. And so the mentioned dependence also appears in the evolutions of the swirls patterns. Overall, flow differences decrease as h decreases. Although these differences occurs in all cycles of every simulation, the averaged analysis become a very convenient way to analyze turbulence patterns.

Despite the changing hydrodynamics conditions between cycles, we observe convergences across and along tank of the averaged velocity, vorticity and of their rms. This convergence appears for the simulations with values of h equal to 0.030 and 0.018 m. For future and similar works, we recommend to develop sensibility analysis of the average velocity, velocity and their rms along and across the tank. We conclude that, although $h = 0.030$ and $h = 0.018$ m simulations are good enough to study vorticity of the flow, the $h = 0.018$ m simulation is more accurate to study the patterns of eddies. Despite the dependence of swirls decay on the wave maker cycle, there is an appearance of homogeneous eddies in the tank when $t > 53$ s.

Chapter 3

The Temporal and Spatial Evolution of Potential Energy, Kinetic Energy and Momentum Flux in Tsunami Waves during Breaking and Inundation[†]

[†] **Citation:** Marivela-Colmenarejo R., Weiss R., Synolakis C. (2017), The Temporal and Spatial Evolution of Potential Energy, Kinetic Energy and Momentum Flux in Tsunami Waves during Breaking and Inundation, Journal of Waterway, Port, Coastal, and Ocean Engineering. **DOI:** 10.1061/(ASCE)WW.1943-5460.0000402.

Abstract

A plethora of studies in the past decade describes tsunami hazards and study their evolution from the source to the target coastline, but mainly focus on coastal inundation and maximum runup. Nonetheless, anecdotal reports from eyewitnesses, photographs and videos suggest counterintuitive flow dynamics, for example rapid initial acceleration when the wave first strikes the initial shoreline. Further, the details of the flow field at or within tens of meters of the shoreline are exquisitely important in determining damage to structures and evacuation times. Based on a set of three-dimensional Lagrangian numerical simulations, we use GPUSPH model to simulate solitary waves and analyze the spatial-temporal distribution of the potential energy, kinetic energy and momentum flux during the breaking process. The wave front accelerates when in the proximity of the shoreline due to the change in slope of wave path and hence is the most dangerous part of the tsunami at any time regardless of the H/d_0 wave ratio. We infer that the highest destructive capacity of flow occurs when momentum flux reaches its maximum and this takes place in the initial shoreline environment. This maximum coincides with the local maxima of the potential and kinetic energy thereby making the shoreline prone to the most turbulent and dangerous flow, during the breaking and inundation processes. Therefore momentum flux is a more important variable, over and above potential and kinetic energy, to be considered in tsunami-hazard and mitigation evaluations and in nearshore structures design.

3.1 Introduction

A large number of fatalities and huge financial loses due to property damage were caused by the 2004 Sumatra tsunami which struck in the Indian Ocean. This presented a wake-up call around the globe for awareness of and improved preparedness for tsunamis (Synolakis and Bernard, 2006) and other coastal hazards. In its aftermath, many countries initiated the assessment or, in some cases reassessment, of their tsunami risks which mainly have been based on the maximum runup determination.

An analytical model for non-breaking solitary-wave runup has been broadly referenced for this purpose which is detailed in Synolakis (1987). However, numerical models serve as a better approach in analysis of breaking waves due to its complexity. Dunbar and Weaver (2008), in their report for U.S. coastlines, outlined the importance of numerical modeling in hazard assessments to quantify the impacts of future destructive coastal hazards. Boussinesq and shallow water equations can be applied to simulate wave dynamics especially for breaking waves (Zhang et al., 2013). Boussinesq equations, in particular, are appropriate to study the wave approach and the runup process, and significant efforts have been made to include the proper dispersive terms (Lynett et al., 2002; Lynett and Liu, 2004a; Madsen et al., 2006; Roeber and Cheung, 2012). For a better representation of the flow field characteristics with Boussinesq equations, Lynett and Liu (2004b) proposed to use multi-layer of the water column. However, the irrotational assumption, appropriate for non-breaking waves, is violated in the surf zone where the waves break (Zhang et al., 2013). Therefore, to fully understand and comprehensively study the very near-shore dynamics, including breaking, three-dimensional computational modeling studies are neccesary.

Dunbar and Weaver (2008) highlighted that the runup value alone might not be suitable to quantify the damage caused by tsunamis. Although runup describes the inundated area to the first order and can be potentially employed for a large-scale overview of post-tsunami damage, runup values might not be sufficient to explore better coastal hazard mitigation strategies and solutions. Park et al. (2013) and Qi et al. (2014) concluded that the flow velocity and momentum flux are highly suitable indicators to estimate tsunami damages. In this contribution, we use three-dimensional Lagrangian numerical simulations to simulate the experimental setup of Synolakis (1986, 1987) for studying the solitary wave canonical problem using GPUSPH model in order to revisit wave breaking hydrodynamics.

Due to their simple nature and the ease in experimental and numerical simulation reproductions, solitary waves are utilized in this study, even though Hammack and Segur (1978), Yeh et al. (1996), Madsen et al. (2008) and Madsen and Schaeffer (2010) discussed the fact that solitary waves are not the best model for tsunami waves.

3.2 Theoretical Background

3.2.1 The GPUSPH model

We use GPUSPH, a numerical model that employs Smoothed Particle Hydrodynamics (SPH), to simulate breaking and non-breaking solitary waves. GPUSPH solves the Navier-Stokes equations aided by the computational resource of graphical processing units (GPU, Hérault et al., 2010, 2006-2014). Due to its Lagrangian nature, SPH is an appropriate approach to simulate flows with high turbulence such as breaking waves (Dalrymple and

Rogers, 2006). Based on the general SPH formulation, the equations of motion are written as (Monaghan, 1992):

$$\begin{aligned}\frac{d\rho_a}{dt} &= \sum_b m_b(v_a - v_b)\cdot\nabla W_{ab}\\ \frac{dv_a}{dt} &= -\sum_b m_b\left(\frac{p_b}{\rho_b^2} + \frac{p_a}{\rho_a^2} + \Pi_{ab}\right)\nabla W_{ab}\end{aligned} \tag{3.1}$$

in which t is time and ρ, m, v and p represent the density, mass, velocity and pressure of the fluid particle a, and its neighboring fluid particles b. The distance between particle a and b is r_{ab}, $v_{ab} = v_a - v_b$, W_{ab} is the kernel or interpolation function and Π_{ab} is the artificial viscosity to prevent spurious particle movements (Monaghan, 1992), where

$$\Pi_{ab} = \begin{cases} \dfrac{-\alpha c_s \mu_{ab} + \Omega\mu_{ab}^2}{\rho_{ab}} & \text{if } v_{ab}\cdot r_{ab} < 0\\ 0 & \text{if } v_{ab}\cdot r_{ab} > 0\end{cases} \tag{3.2}$$

Here

$$\mu_{ab} = \frac{h v_{ab}\cdot r_{ab}}{r_{ab}^2 + (0.1h)^2} \tag{3.3}$$

and the speed of sound, c_s, is defined by $10\cdot g d_0$, where g is the acceleration due to gravity and d_0 is the still water depth. For surface flows, the parameters α and Ω are constants with values of 0.01 and 0 respectively (Monaghan, 1994). In our simulations the initial distance between particles, h, is constant. For each particle to consider its neighbors, the radius of the interpolation kernel is $2h$. All particles within the kernel are referred to as neighbor particles and form the neighbor list for the calculation of the physical properties. Because of the relative movement of particles, neighbor lists need to be updated at each time step. Since SPH model requires that the fluid be artificially compressible: Eq. (1), an equation of state is required to relate pressure to density (Monaghan, 1994):

$$p_i = \frac{c_s^2}{\rho_i\cdot\gamma}\left(\left(\frac{\rho_i}{\rho_0}\right)^{\gamma} - 1\right) \tag{3.4}$$

where p_i and ρ_i are the pressure and density of the particles i, ρ_0 is the reference density, and the parameter $\gamma = 7$. For a more complete description of the SPH method, we refer to Gingold and Monaghan (1977), Monaghan (1992) and Monaghan (1994).

3.2.2 The canonical problem for long-wave runup

We employ the experimental setup of Synolakis (1986, 1987) for the numerical simulations with GPUSPH (Fig. 3.1). The particle diameter is 0.010 m and equal to h in our simulations. The experimental domain is 37.73 m long, 0.39 m wide, and 0.61 m high. The initial water depth is $d_0 = 0.70$ m. The toe of the beach, X_0, is located at 14.68 m measured from the initial wavemaker location. Parameter β represents the slope of the beach ($\beta = 1 : 19.85$). H is the initial maximum wave height measured from the surface of the still water. The origin of the coordinate system is located at the initial position of the shoreline, x increases towards the wavemaker and z increases upward. The solitary waves have the following surface profile:

$$\eta(x,0) = H\,sech^2\left[\sqrt{3H/4d_0^3}(x - X_1)\right] \tag{3.5}$$

where X_1 refers to the x-location where the wave presents its amplitude. We use the wavemaker formula obtained from Eq. (3.5) and presented in Synolakis (1990):

$$\frac{d\delta}{dt} = \frac{H sech^2\, k(\delta - c_w t)}{1 + H sech^2\, k(\delta - c_w t)} \tag{3.6}$$

in which δ is the wavemaker displacement, k is the wave number ($k = \sqrt{3H/4d_0^3}$), and c_w is the propagation velocity of the wave.

The wavemaker is represented by boundary particles regularly distributed and applies Lennard-Jones boundary condition (Jones, 1924; Monaghan, 1994). We employ the smoothing kernel

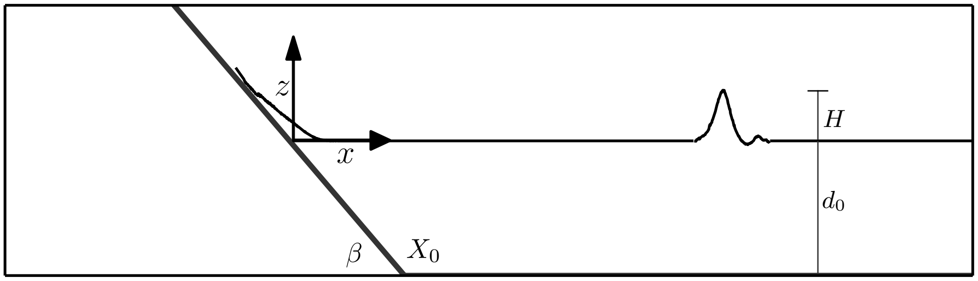

Figure 3.1: Experimental setup from Synolakis (1986) and Synolakis (1987) used in our GPUSPH simulations. The toe of the sloping beach is denoted by X_0 and located 14.68 m from the initial wavemaker position. H is the wave height measured from the initial depth, $d_0 = 0.70$ m. The beach slope is $\beta = 1 : 19.85$. Coordinate system origin is located at the initial beach shoreline.

of boundaries presented in Monaghan and Kajtar (2009) to the bottom, beach and side boundaries.

3.2.3 Data analysis of the GPUSPH simulations

To analyze the simulation results, we divide the model domain into a row of segments along the x-direction. Each segment is 0.01 m thick in x-direction, 0.39 m wide in y-direction and with infinite height. The time increment of the analysis is $\delta t = 0.10$ s. For a certain δt, we average in each i segment: 1) potential energy: $P_{Ei} = \rho g(|d_0| + \eta_i)$; 2) kinetic energy: $K_{Ei} = \frac{1}{2}\rho u_i^2$; and 3) momentum flux per unit width: $M_{f_i} = \rho(|d_i| + \eta_i)u_i^2$ (Yeh, 2006), where d_i and η_i are respectively the averaged water depth and the averaged water surface of each segment measured from the surface of still water, and u_i is the averaged x-velocity of each segment. Then we pick the maximum values and their locations of the aforementioned variables as follows: maximum flow potential energy, $\mathcal{P} = max\{P_{Ei}\}$; maximum flow kinetic energy, $\mathcal{K} = max\{K_{Ei}\}$; and maximum momentum flux, $\mathcal{M} = max\{M_{f_i}\}$. Note that we obtain one value of $\mathcal{P}$, $\mathcal{K}$ and $\mathcal{M}$ per δt. We repeat this process at each δt so we track the maxima values in space and time. Then we obtain: the absolute maximum of the flow potential energy during breaking ($\mathcal{P}' = max\{\mathcal{P}\}$), the absolute maximum of the flow kinetic energy ($\mathcal{K}' = max\{\mathcal{K}\}$) and the absolute maximum of the momentum flux ($\mathcal{M}' = max\{\mathcal{M}\}$). Note that we obtain just one value of $\mathcal{P}'$, $\mathcal{K}'$ and $\mathcal{M}'$ per simulation and that we do not consider high values of $\mathcal{P}$ during beach inundation for $\mathcal{P}'$ determination. For data analysis, we employ dimensionless time, $t^* = t\sqrt{g/d_0}$, dimensionless length, $x^* = x/d_0$, and dimensionless water-surface elevation, $\eta^* = \eta/d_0$.

Additionally, we use the wave crest, W_c, defined by the water elevation that represents the wave amplitude at each δt. The tracking of the wave crest during the simulation defines the wave crest path. We define the wave front, W_f, as the part of the wave whose elevation is 40% of H. The wave front threshold is determined by comparing the wave front of case $H/d_0 = 0.0185$ shown in Fig. 3.5.5 of Synolakis (1986) with a SPH simulation with the same setup. The best fit of the wave front comparison is determined by defining wave front as 40% of H. We keep this criterion for the rest of H/d_0 cases studied in this work.

3.3 Results

3.3.1 Validation of GPUSPH

To validate GPUSPH for the canonical problem, we simulate the strongly breaking 225a case as outlined in Synolakis (1986). The case refers to experiments with $d_0 = 0.1962$ m and $H/d_0 = 0.286$. In Fig. 3.2, we compare the experiment 225a (blue crosses) and GPUSPH

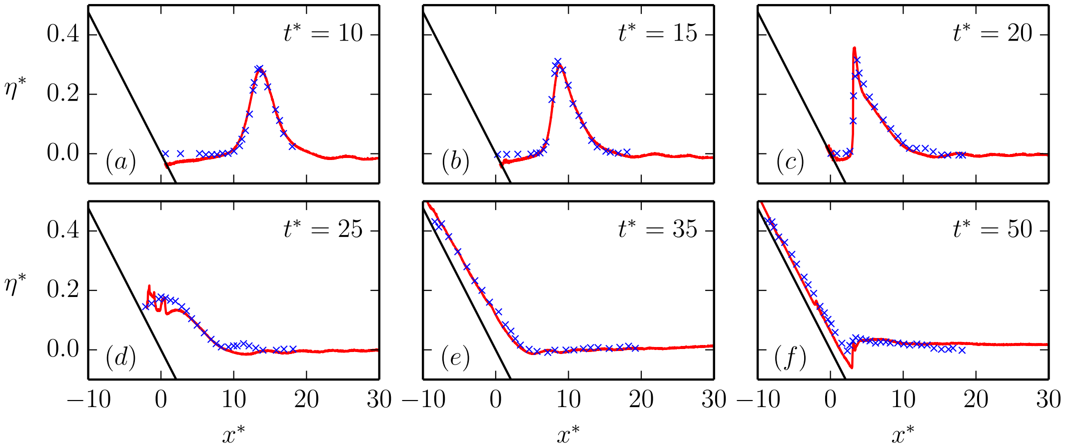

Figure 3.2: Comparison of water surface profiles between laboratory experiments ($H/d_0 = 0.286$, blue crosses, Synolakis, 1986) and the numerical simulation (red solid line). Note that the slight difference between the simulation and experiment near the shoreline in the early phases of the simulation, at $t^* = 10$ and $t^* = 15$, are due to numerical reasons. The slight depression is caused by the fact that a small number of particles are present and their velocity is small, resulting into to spurious behavior. However, it should be noted that this does not affect the wave itself, not even during its inundation because of the large and wave-related particle velocities.

simulation (red lines) before, during, and after wave breaking. Figure 3.2 shows an excellent fit between the measurements from the laboratory experiment and the GPUSPH simulation, even after breaking. In simulation, the water surface in front of the incident wave is dipped downward at $t^* = 10$ and 15. This is because the simulation initiates with regularly spaced particles and when $t > 0$ the particles get arranged according to the governing equations. For numerical reasons, the particles withdraw slightly from the original shoreline position because of a limited number of particles in a thin water layer with small particle velocities. However, there is no impact of this numerical artifact on the wave dynamics or inundation due to larger particle velocities affiliated with these processes. Thus the discrepancy is not observed in figures at $t^* > 20$, 25, 35 and 50.

Furthermore, in Fig. 3.3 we compare the evolution of the maximum wave heights, η_{max},

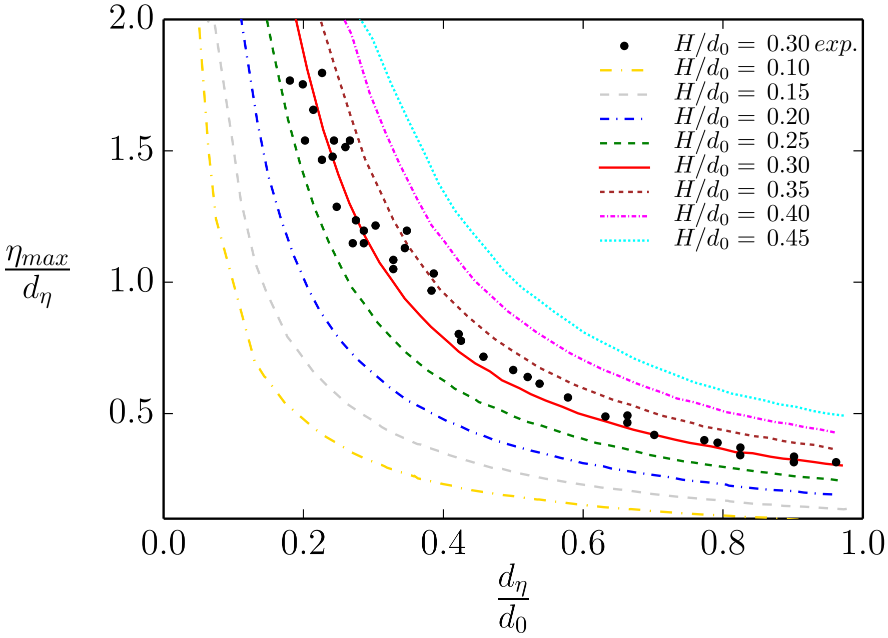

Figure 3.3: Maximum amplitude of different solitary waves simulations (lines) and from the experiment $H/d_0 = 0.30$ from Synolakis and Skjelbreia (1993) up 1:19.83 beach. Different water depth between 0.1 m and 0.4 m were taken into account in the experiment Synolakis and Skjelbreia (1993), but the data coming from different water depths is not discriminated, which helps to explain the significant spread of the experimental results.

between the solitary wave $H/d_0 = 0.30$ from Synolakis and Skjelbreia (1993, black dots) and our simulation (red solid line) where d_η is the depth at x-location of η_{max}. The observed discrepancy can be attributed to the complexity of obtaining accurate values for $\eta_{max}/d_\eta >$ 1.0. In the original study by Synolakis and Skjelbreia (1993), the data shown as black dots in Fig. 3.3 were obtained over different depths that varies from 0.1 m to 0.4 m. The above mentioned study does not provide actual water depth at each point which makes it more complex to reduce the distribution of data points in Fig. 3.3. However, the overall fit between the experiments and simulations is considered good despite the dispersion in the data points.

An additional validation is carried out by comparing the distribution of velocities between the experimental setup presented in Irish et al. (2014) and a SPH simulation with the same

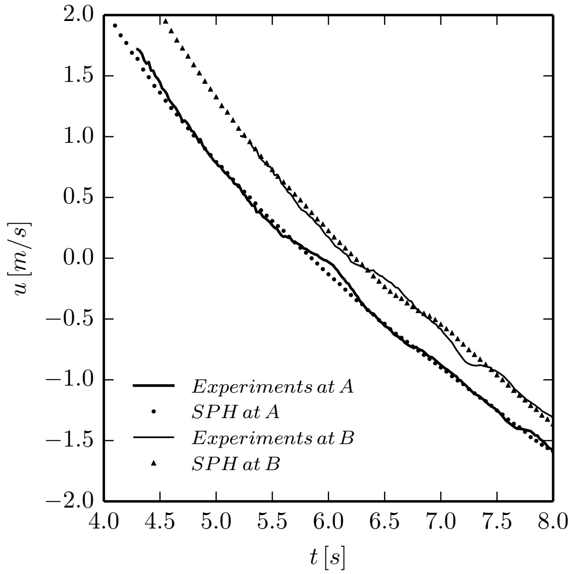

Figure 3.4: u-velocity comparison between the experiments (Irish et al., 2014) and the SPH simulations at locations $x = 32.87$ m (A) and $x = 35.06$ m (B) respectively from the initial wavemaker location ($x = 0$).

setup. The beach slope in these experiments is 1:10 whose toe is located at the end of a horizontal plane, located 22 m initial wavemaker location. The water depth is 0.73 m and the wave height is 0.43 m. Velocities in the experiments were measured using acoustic Doppler velocimeters (ADVs; 50 Hz) at locations x = 32.87 m (A) and x = 35.06 m (B). The elevation of the ADVs' sensors is 0.02 m. We measure the horizontal velocities from our simulation at the exact locations of the ADV sensors and we compare them with the horizontal velocity of Irish et al. (2014) in Fig. 3.4. A good fit is observed even in this case of intense breaking (H/d_0 = 0.589). This good fit also indicates the suitability of the SPH particle size to simulate the solitary waves presented in this work. Note that there is a lack of data from experiments during initial runup compared with SPH. This is because the bubbly and turbulent bore resulted in noisy measurements from ADVs.

We also carry out a SPH simulation of a solitary wave to compare velocity fields and vertical distributions with Lin et al. (1999) in which a $k-\varepsilon$ turbulence model was coupled with a two-dimensional RANS equation-type model. The particle size for this simulation is also 0.01 m and $H/d_0 = 0.28$. From the times $t^* = 10$, 15, 20 and 25 presented in Lin et al. (1999), we pick $t^* = 15$ and 20 for comparison because they depict the wave breaking. Figures 3.5 and 3.6 show the comparison of velocity analysis at $t^* = 15$ and 20 respectively where we use $\sqrt{g(d_0+H)}$, d_0 and $t\sqrt{g/d_0}$ to normalize velocity, space and time respectively. To obtain the velocity fields, we divide the domain in a $x-z$ array of prisms. The dimensions of the prisms are 0.25 m in x-direction, 0.39 m (same as the domain) in y-direction and 0.07 m in z-direction. We use all the particles within each prism to average the u-velocity, v-velocity and w-velocity along the y-direction. We observed that the averaged v-velocity is extremely small, especially before breaking. Figures 3.5a and 3.6a depict the comparison of the velocity fields between Lin et al. (1999) (blue arrows) and from our simulation (red arrows). As in Lin et al. (1999), the velocity magnitude is calculated by $\sqrt{u^2+w^2}$ and is represented by the vector length. The general structure of the velocity fields have very similar behavior in both cases indicating the suitability of our model. The velocity profiles are obtained by averaging the velocities of fluid particles contained within columns centered at $x^* = 10.065$, 8.065 and 6.065 for $t^* = 15$ and $x^* = 5.065$, 4.065 and 3.065 for $t^* = 20$. The dimensions of the columns are 0.01 m in x-direction, 0.39 m in y-direction (same as the domain) and they have infinite height. Figures 3.5b-d ($t^* = 15$) and 3.6b-d ($t^* = 20$) show comparisons of vertical distributions of u^* and w^* between SPH and Lin et al. (1999) at the aforementioned locations. We observe a good fit in all the comparisons of the velocity profiles. These results enforce the suitability of SPH to study flow velocity

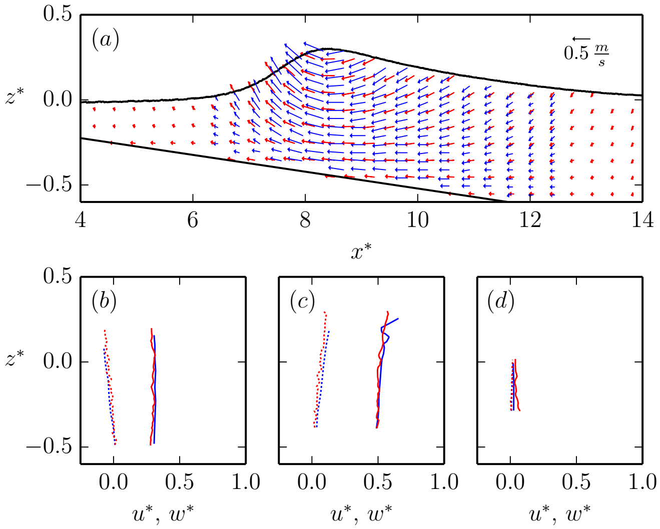

Figure 3.5: Velocity results comparison of a $H/d_0 = 0.28$ solitary wave at $t^* = 15$ between Lin et al. (1999) and our SPH simulation represented with blue and red colors respectively. We use d_0, $t\sqrt{g/d_0}$ and $\sqrt{g(d_0+H)}$ to normalize space, time and velocity respectively. a) shows the velocity field distribution. Use the 0.5 m/s arrow as reference. b), c) and d) show the comparison of the vertical distribution of y-averaged u^* velocity (continuous lines) and y-averaged w^* velocity (discontinuous lines) at $x^* = 10.065$, $x^* = 8.065$ and $x^* = 6.065$ respectively.

3.3.2 Solitary waves results

Figure 3.5.5 presented in Synolakis (1986) shows the comparison of the wave front path, for a $H/d_0 = 0.0185$ solitary wave, between experiments and the solution of the nonlinear theory. Synolakis (1986) indicates the presence of an intense wave front acceleration in the shoreline environment that has to be analyzed. We study this effect by simulating solitary waves with different H/d_0 ratios and showing the dimensionless spatio-temporal evolutions of their wave front paths in Fig. 3.7. Note in this figure that, the more horizontal the slope of the wave path is, the higher wave velocity is and vice versa.

The temporal evolution of $\mathcal{P}$, $\mathcal{K}$ and $\mathcal{M}$ and their absolute maxima are presented in Fig. 3.8

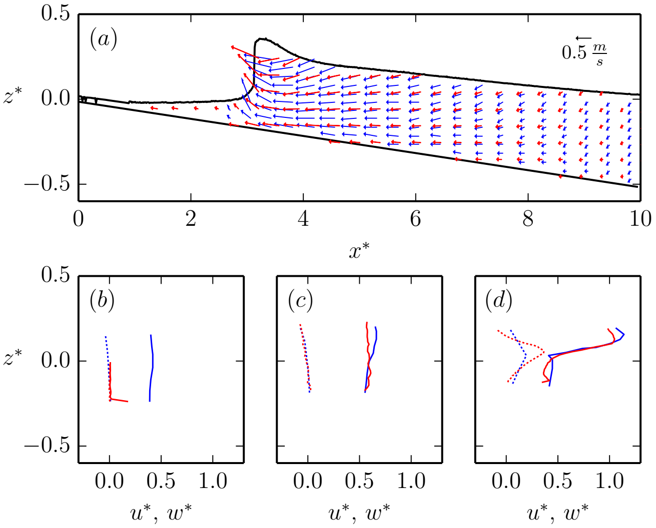

Figure 3.6: Velocity results comparison of a $H/d_0 = 0.28$ solitary wave at $t^* = 20$ between Lin et al. (1999) and our SPH simulation represented with blue and red colors respectively. We use d_0, $t\sqrt{g/d_0}$ and $\sqrt{g(d_0+H)}$ to normalize space, time and velocity respectively. a) shows the velocity field distribution. Use the 0.5 m/s arrow as reference. b), c) and d) show the comparison of the vertical distribution of y-averaged u^* velocity (continuous lines) and y-averaged w^* velocity (discontinuous lines) at $x^* = 5.065$, $x^* = 4.065$ and $x^* = 3.065$ respectively.

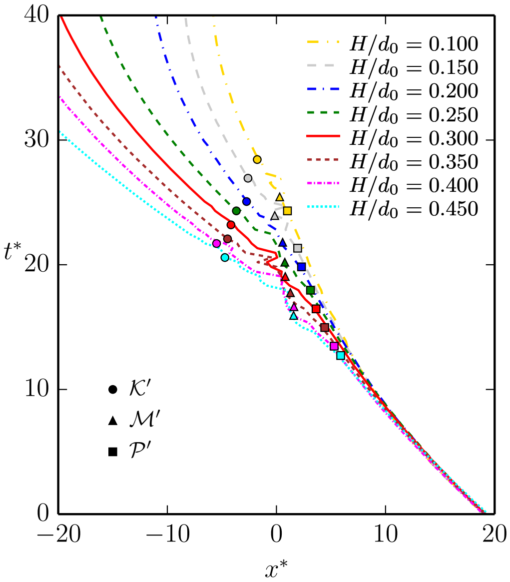

Figure 3.7: Wave front path of solitary waves of GPUSPH simulations for different ratios of H/d_0. $x^* = x/d_0$ and $t^* = t\sqrt{g/d_0}$. Origin of normalized time is set when wave front reaches the vertical of the beach toe, X_o, shown in Fig. 5.3. Squares, circles and triangles represent the absolute maxima of flow potential energy, $\mathcal{P}'$, the absolute maxima of flow kinetic energy, $\mathcal{K}'$, and the absolute maxima of momentum flux, $\mathcal{M}'$, respectively. Note that the x^* and t^* of $\mathcal{P}'$, $\mathcal{K}'$ and $\mathcal{M}'$ appear always on the wave front path.

for different H/d_0 ratios. $\mathcal{P}'$, $\mathcal{K}'$ and $\mathcal{M}'$ are represented consistently with squares, circles and triangles respectively in Fig. 3.7, 3.8, 3.9 and 3.10. The format of the lines that represent $\mathcal{P}$, $\mathcal{K}$ and $\mathcal{M}$ is consistent in Fig. 3.8 and 3.9. Figure 3.8a shows the temporal evolution of $\mathcal{P}$, in lines and when $\mathcal{P}'$ occurs. Figure 3.8b depicts the evolution of $\mathcal{K}$, and when $\mathcal{K}'$ occurs. The maximum kinetic energy evolution has two peaks. The first and smaller peak occurs due to the bore collapse (Yeh et al., 1989), and the second one arises at the beginning of the inundation due to the highly turbulent flow (circles located onshore in Fig. 3.7). Figure 3.8c shows the evolution of $\mathcal{M}$, and when $\mathcal{M}'$ occurs.

For the different H/d_0 solitary waves studied, Fig. 3.9 details the spatial evolution of the variables depicted in Fig. 3.8. Figure 3.9a shows $\mathcal{P}$ over space and where $\mathcal{P}'$ is. Figure 3.9b

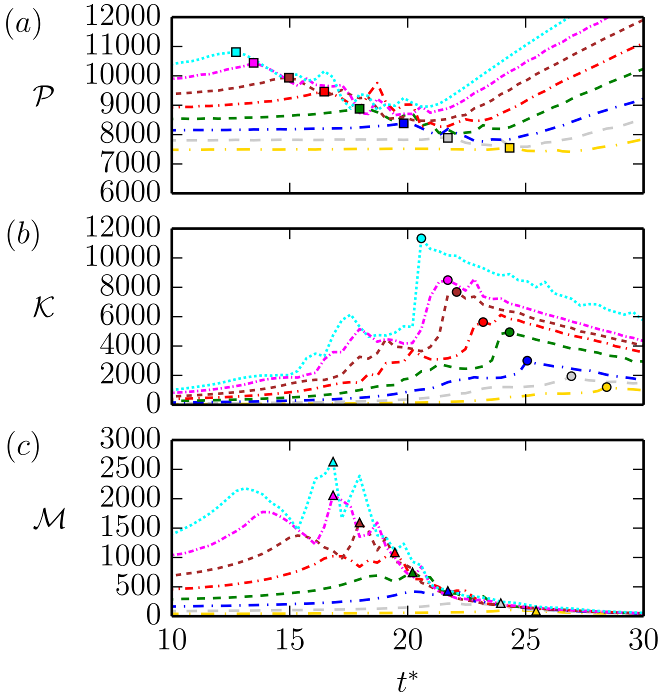

Figure 3.8: *a*) shows the temporal evolution of the maxima flow potential energy, $\mathcal{P}$, for different H/d_0 ratios and their absolute maxima, $\mathcal{P}'$, with squares. Values of $\mathcal{P}$ during beach inundation are not considered for $\mathcal{P}'$ determination. *b*) depicts the temporal evolution of the maxima flow kinetic energy, $\mathcal{K}$, for different H/d_0 ratios and their absolute maxima, $\mathcal{K}'$, with circles. *c*) shows the temporal evolution of the maxima momentum flux, $\mathcal{M}$, for different H/d_0 ratios and their absolute maxima, $\mathcal{M}'$, with triangles. For legend use the one shown in Fig. 3.7.

depicts $\mathcal{K}$ over space and $\mathcal{K}'$ locations (always onshore, Fig. 3.7). As in Fig. 3.8b, the $\mathcal{K}$ evolutions have two peaks as well. Figure 3.9c shows $\mathcal{M}$ over space and where $\mathcal{M}'$ is. Note that $\mathcal{M}'$ occur just before the shoreline and where $\mathcal{P}$ reach their local maxima or second peaks. These locations are also where the $\mathcal{K}$ experience sharp increases. Note that the wave approaches the beach from right to left in Fig. 3.9.

Figure 3.10a provides the relationship between the normalized absolute maxima of the momentum flux, $\mathcal{M}'^*$, with the H/d_0 ratio. We use the $\mathcal{M}'$ value of H/d_0 = 0.45 run for

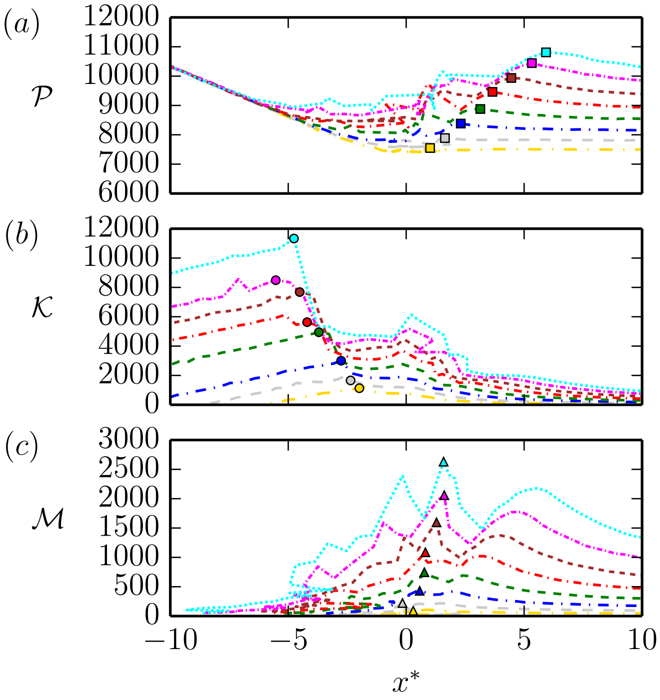

Figure 3.9: *a*) shows the spatial evolution of the maxima flow potential energy, $\mathcal{P}$, for different H/d_0 ratios and their absolute maxima, $\mathcal{P}'$, with squares. *b*) depicts the spatial evolution of the maxima flow kinetic energy, $\mathcal{K}$, for different H/d_0 ratios and their absolute maxima, $\mathcal{K}'$, with circles. *c*) shows the spatial evolution of the maxima momentum flux, $\mathcal{M}$, for different H/d_0 ratios and their absolute maxima, $\mathcal{M}'$, with triangles. For legend use the one shown in Fig. 3.7.

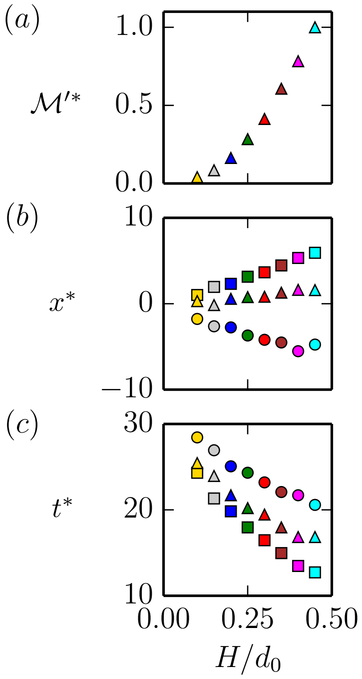

Figure 3.10: As Fig. 3.7, 3.8 and 3.9, this figure represents $\mathcal{P}'$, $\mathcal{K}'$ and $\mathcal{M}'$ with squares, circles and triangles respectively. *a*) provides the relationship between the normalized absolute maxima of the momentum flux, $\mathcal{M}'^{*}$, with the H/d_0 ratio. We use the $\mathcal{M}'$ value of the $H/d_0 = 0.45$ run for normalization. *b*) shows the relationship between the location where the absolute maxima of the flow potential energy, $\mathcal{P}'$, flow kinetic energy, $\mathcal{K}'$, and momentum flux, $\mathcal{M}'$, occur with the H/d_0 ratio. *c*) depicts the relationship between the time when $\mathcal{P}'$, $\mathcal{K}'$ and $\mathcal{M}'$ appear at with the H/d_0 ratio. For colors use the legend shown in Fig. 3.7.

normalization. Figure 3.10b shows the relationships between the locations of $\mathcal{P}'$, $\mathcal{K}'$ and $\mathcal{M}'$ and the H/d_0 ratios. Furthermore, Fig. 3.10c displays the relationships between the times of $\mathcal{P}'$, $\mathcal{K}'$ and $\mathcal{M}'$ and the H/d_0 ratios.

3.4 Discussion

In this contribution, we studied the three-dimensional breaking process of several solitary waves using the GPUSPH model. We tracked their wave fronts and showed their spatio-temporal evolution in Fig. 3.7. Note that slopes of the curves represent velocities of the wave front and variations in the slopes indicates a change in the wave front velocity (acceleration or deceleration). Furthermore, we can infer that the wave front acceleration intensifies with increasing H/d_0 ratios for gentler slopes. These accelerations occur between $\mathcal{P}'$ and $\mathcal{K}'$ in Fig. 3.7, 3.8, 3.9 and 3.10 and confirm the analytically predicted flow acceleration of Ho and Meyer (1962) and the numerical experiments of Hibberd and Peregrine (1979), as well as it shows a similarity in the near-shore behavior discussed by Pujara et al. (2015). We focused on the analysis of this acceleration with the goal to better understand near-shore wave breaking processes and to identify most danger-prone areas associated with tsunami inundation.

The wave front acceleration associated with bore collapse (Yeh, 1991) has implications for the spatio-temporal evolution of $\mathcal{P}$, $\mathcal{K}$ and $\mathcal{M}$. While shoaling, as the wave becomes higher and steeper, the maximum potential energy, $\mathcal{P}$, also increases. The maximum elevation during shoaling defines the absolute maximum of the potential energy, $\mathcal{P}'$. The largest velocities occur in the wave tip during bore collapse. However, the averaged velocity of the wave tip segment is not the largest because the averaging also considers slower water located deeper. The largest averaged velocity in the entire simulation appears at $\mathcal{K}'$ (circles in Fig. 3.8b and 3.9b), which is when and where the wave front and wave crest converge (Fig. 3.7). This location is onshore so the water is shallow and the entire velocity profile progresses with high velocity.

During breaking, potential energy is transformed into kinetic energy (Yeh et al., 1989). However this transformation of energy does not occur suddenly. Experiments show that the energy transformation is done through a gradual momentum exchange (Yeh, 1991), which can also be observed between $\mathcal{P}'$ and $\mathcal{K}'$ in Fig. 3.8a-b and in 3.9a-b. To better understand the energy transformation process, it is important to observe that when $\mathcal{P}'$ occurs (squares in Fig. 3.8a), $\mathcal{K}$ at that time is very low when compared with $\mathcal{K}'$, (circles in Fig. 3.8b). Conversely, when $\mathcal{K}$ reaches its $\mathcal{K}'$, $\mathcal{P}$ at that time is low compared with its absolute maximum, $\mathcal{P}'$, (squares in Fig. 3.8a). After $\mathcal{P}'$, $\mathcal{P}$ transforms into $\mathcal{K}$ during breaking and a highly turbulent flow environment is generated due to the bore collapse. Despite the turbulence, we observe a consistent transformation pattern, regardless of the H/d_0 ratio, where the second peak of $\mathcal{P}$ in Fig. 3.8a almost coincides with the first peak of $\mathcal{K}$ in Fig. 3.8b. This similarity also is observed in the spatial analysis: the second peak of $\mathcal{P}$ almost coincides with first peak of $\mathcal{K}$ in Fig. 3.9a and 3.9b respectively.

Kinetic and potential flow energies are partly responsible for the powerful flow conditions during tsunamis. Furthermore we employ the momentum flux that has its absolute maximum where $\mathcal{P}$ and $\mathcal{K}$ have their almost simultaneous local maxima. The hydrodynamic force and the slamming force have been identified (FEMA, 2011) to govern the tsunami load. However, since we are not modeling any object located in the wave breaking trajectory, we study the momentum flux instead considering that hydrodynamic force is proportional to the momentum flux (Yeh, 2006). Also, according to FEMA (2008), Koshimura et al. (2009b) and Koshimura et al. (2009a), the momentum flux can be related to the probability of damage. For studies with objects in the flow we recommend further analysis that consider slamming forces since they may be larger than hydrodynamic force, of which momentum flux is a proxy. Figures 3.8c and 3.9c depict the spatio-temporal evolution of the maximum momentum flux, $\mathcal{M}$. The triangles in both figures indicate the absolute maximum of momentum flux, $\mathcal{M}'$, which takes place at the same time the local maxima of potential and kinetic energies occur. $\mathcal{M}'$ appears just after the wave tip falls down on the water surface. This bore collapse causes a highly chaotic and turbulent layer of flow with significantly higher velocity at the surface and its vicinity. This process, in turn, suddenly increases $\mathcal{K}$ (first sharp increase in Fig. 3.8b and Fig. 3.9b). Bore collapse also leads to an increase of $\mathcal{P}$ (local maxima peaks in Fig. 3.8a and 3.9a). Both simultaneous gains in $\mathcal{K}$ and $\mathcal{P}$ lead to $\mathcal{M}'$ (Fig. 3.8c and 3.9c). This juxtaposition of the three variables mentioned above pins down the spatio-temporal extent of the most turbulent and dangerous flow. $\mathcal{M}'$ occurs just before shoreline (triangles close to $x^* = 0$ in Fig. 3.9c.) regardless of the H/d_0 ratio of the wave. For the larger waves, $H/d_0 =$ 0.45, 0.40 and 0.35 runs, secondary peaks most immediately follows $\mathcal{M}'$ thereby amplifying their dangerousness. We recommend that the aforementioned results be considered in the design of shoreline facilities due to their relevance.

Figure 3.10a depicts the $\mathcal{M}'$ as function of H/d_0. This figure allows to estimate the absolute maximum of momentum flux for any solitary wave not studied in this work and developed with the same setup. Additionally, Fig. 3.10b and 3.10c render the spatial and temporal distribution of $\mathcal{P}'$, $\mathcal{K}'$ and $\mathcal{M}'$. The larger the H/d_0 ratio is, the larger the distance between $\mathcal{P}'$ and $\mathcal{K}'$ become (see Fig. 3.10b) and larger the time difference between them gets (see in Fig. 3.10c). Also, the larger the H/d_0 is, the longer the breaking process takes and the farther the runup reaches. Therefore by knowing the H/d_0 ratio of a solitary wave, it is possible to estimate not only the magnitude of the momentum flux, but also its occurrence spatially and temporally.

3.5 Conclusions

In this contribution, we carried out three-dimensional numerical simulations of solitary waves with GPUSPH in order to study their evolution during breaking in the proximity of the shoreline. Due to the three-dimensional nature, neither the shallow water equations nor the Boussinesq approximations can describe wave breaking analysis accurately. We obtain the maxima, in space and time, of potential energy, kinetic energy and momentum flux of the flow by averaging and obtaining the maximum of these three variables in segments along x axis. Based on our study, we conclude the following:

1) The spatial-temporal tracking of the wave front, for different H/d_0 ratios, shows that the smaller the slope of the wave path, the higher its wave velocity. The slope of the wave front trajectory changes in proximity to the shoreline and so this is where the flow accelerations occur (Fig. 3.7), which is consistent with the near-shore studies of Ho and Meyer (1962) and Hibberd and Peregrine (1979). This flow acceleration is a consequence of conversion of absolute maximum potential energy into kinetic energy.

2) We obtain and plot the locations and time of the absolute maxima of potential energies, kinetic energies and momentum flux for various H/d_0 (Fig. 3.8 and 3.9). They appear on the curve of their respective H/d_0 wave path (Fig. 3.7) thereby implying that the absolute maximum of flow potential energy, flow kinetic energy and momentum flux always occur in the wave front, regardless of the H/d_0 ratio. Hence we conclude that the wave front is the most dangerous part of the tsunami at any time, regardless of the H/d_0 ratio, and for waves with the same setup.

3) Momentum flux is a more important variable, compared to potential or kinetic energies, to classify the hazard of tsunami wave breaking. This is mainly because the peaks of the absolute maxima of momentum flux occur at points of nearly simultaneous local maxima of potential and kinetic energies, regardless of their H/d_0 ratio. The occurrence is just before the shoreline thereby exposing it to the most turbulent and powerful flow, during the breaking and inundation processes. However, for waves with larger H/d_0 ratio, secondary peaks of the above mentioned variables closely follow the absolute maxima which results in a hazard-amplifying effect.

The maxima tracking of the variables studied is an appropriate technique to analyze a complex hydrodynamic phenomenon such as waves breaking. These conclusions render a better understanding of the breaking process near the shore and let us identify the physical variables that must be considered to evaluate the destructive hazards of solitary waves in space and time. Also they provide important considerations to be taken into account while developing more reliable tsunami-risk evaluations, in order to protect marine infrastructures and human lives.

Chapter 4

Numerical Simulation of Nonlinear Long Waves in the Presence of Discontinuous Coastal Vegetation [†] [‡]

[†] **Citation:** A. Zainali, R. Marivela, R. Weiss, J. L. Irish, Y. Yang, Numerical simulation of nonlinear long waves interacting with arrays of emergent cylinders; arXiv:1610.00687 [physics.geo-ph].

- In review process for the Marine Geology journal.

[‡] **Contribution:** This paper is part of Amir Zainali's dissertation (Zainali, 2016). My contribution is this paper is 20 percent approximately among the authors.

Abstract

We presented numerical simulation of long waves, interacting with arrays of emergent cylinders inside regularly spaced patches, representing discontinued patchy coastal vegetation. We employed the fully nonlinear and weakly dispersive Serre-Green-Naghdi equations (SGN) until the breaking process starts, while we changed the governing equations to nonlinear shallow water equations (NSW) at the vicinity of the breaking-wave peak and during the runup stage. We modeled the cylinders as physical boundaries rather than approximating them as macro-roughness friction. We showed that the cylinders provide protection for the areas behind them. However they might also cause amplification in local water depth in those areas. The presented results are extensively validated against the existing numerical and experimental data. Our results demonstrate the capability and reliability of our model in simulating wave interaction with emergent cylinders.

4.1 Introduction

Tsunamis, caused by different events such as earthquakes and landslides, and storms pose significant threat to human life and offshore and coastal infrastructure. The effects of coastal vegetation on long waves have been investigated extensively in the past (e.g. Mei et al., 2011; Anderson and Smith, 2014). It has been considered that continuous vegetation provides protection for the areas behind them (e.g. Irtem et al., 2009; Tanaka et al., 2007). However, limited studies focused on the propagation and run-up of long waves in the presence of discontinuous vegetation (see Irish et al., 2014). The following question arises: Do discontinuous arrays of cylinders, representing coastal vegetation such as mangroves, coastal forests, and man-made infrastructure, act as barriers or as amplifiers for energy coming ashore during coastal flooding events.

Three dimensional numerical simulation is the superior choice when computational accuracy is concerned. However, three dimensional models are computationally very expensive, and the large scale of real-world problems limits their applications in practice. Furthermore, the vertical component of the flow acceleration is small compared to the horizontal components. Thus, high fidelity depth integrated formulations, such as nonlinear shallow water equations (NSW), can be an attractive alternative for practical problems.

NSW have been extensively used for simulating long waves. Due to their conservative and shock-capturing properties, they represent a suitable approximation of the wave breaking as well as inundation. However, these equations are only valid for very long waves, and they cannot properly resolve dispersive effects before wave breaking. Thus, they become inaccurate in predicting the effects of shorter wavelength which is important for simulating the nearshore wave characteristics. On the other hand Boussinesq-type equations take dispersive effects into account and can be used to simulate the nearshore wave propagation until the breaking point more accurately. The importance of dispersive effects, until the breaking process starts, is demonstrated in Figure 4.1. Using SGN the transient leading wave almost maintains its shape, during propagation over constant water depth. However, if we ignore the effects of dispersive terms (i.e. by using NSW), after traveling a sufficiently large distance (for this scenario 80 m) the wave height decreases by the factor of 3.

Different classes of higher-order depth-integrated equations, based on Boussinesq wave the-

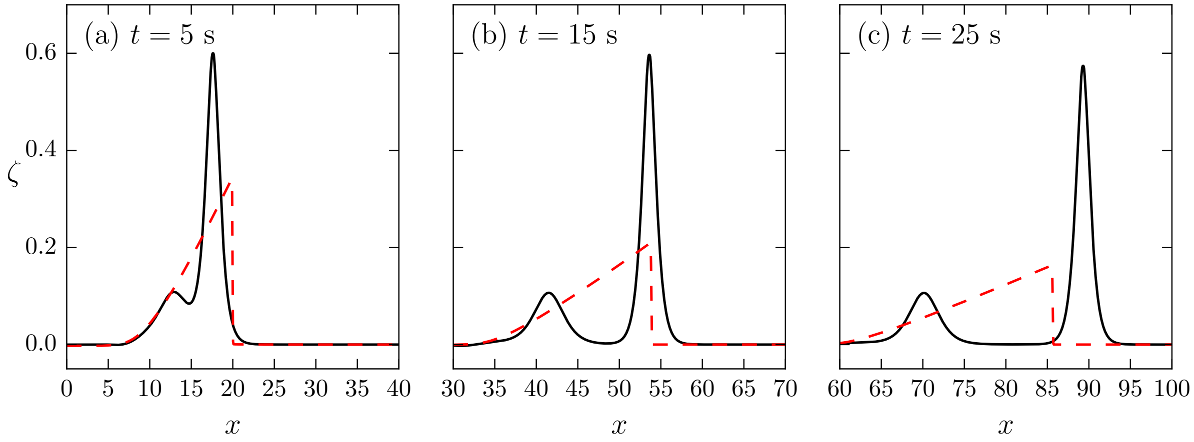

Figure 4.1: Free surface elevation of the solitary-type transient wave over constant water depth at (a) t = 5 s, (b) t = 15 s, and (c) t = 25 s; (——) 1D-SGN, and (- - -) 1D-NSW. The following parameters are used: h_0 = 0.73 m, H = 0.50 m, k_0 = 0.54 m^{-1}.

ory, have been derived and presented in literature on simulating shallow water flows: Wei et al. (1995); Liu (1994); Lannes and Bonneton (2009). In this study, we employ fully nonlinear weakly dispersive Boussinesq equations, also known as Serre-Green-Naghdi equations (SGN, Lannes and Bonneton, 2009). These equations have two advantages compared to others: (a) They only have spatial derivatives up to second order while other equations usually include spatial derivatives of third order, and (b) they do not have any additional source therm in the conservation of mass. These properties improve the computational stability and robustness of the model. Furthermore, unlike earlier studies in which vegetation effects are approximated by an ad-hoc bottom friction coefficient (e.g. Yang et al., 2016; Mei et al., 2011), we model the cylinders as physical boundaries. This enables us to simulate the wave propagation through discontinuous arrays of cylinders without making any assumptions. We demonstrate the capability of the SGN equations in simulating of the waves interacting with both offshore and coastal structures while sustaining the computational performance.

4.2 Theoretical Background

We are interested in simulating long waves; thus $\mu = (h_0/\lambda)^2 << 1$, where λ denotes the wavelength, and h_0 is the still water depth. Assuming an inviscid and irrotationl flow (in the vertical direction), expanding the Euler equations into an asymptotic series and keeping terms up to $O(\mu^2)$, SGN equations can be written in the form of

$$\begin{cases} \partial_t h + \nabla \cdot (h\boldsymbol{u}) = 0, & \text{(4.1a)} \\ \partial_t (h\boldsymbol{u}) + \nabla \cdot \left(h\boldsymbol{u} \otimes \boldsymbol{u} + \frac{1}{2} g h^2 \mathbf{I} \right) = -gh\nabla b + \boldsymbol{\mathcal{D}}, & \text{(4.1b)} \end{cases}$$

where $\boldsymbol{\mathcal{D}}$ is a nonlinear function of the free-surface elevation ζ, the depth-integrated velocity vector $\boldsymbol{u}$, and their spacial derivatives; h is the water depth; b represents the bottom variations; and $\mathbf{I}$ is the identity tensor. See Bonneton et al. (2011) and Lannes and Bonneton (2009) for the complete form of the equations and their derivation. Note that by setting $\boldsymbol{\mathcal{D}} = 0$, Eqs. (4.1a)-(4.1b) will reduce to the NSW equations (accurate to $O(\mu)$).

We employ the Basilisk code to solve the governing equations (Basilisk, URL: basilisk.fr, Popinet, 2015). The computational domain is discretized into a rectangular grid and solved using the second order accurate scheme in time and space. We refer to Popinet (2015) for more information about the numerical scheme. Friction effects become important as the wave approaches the coast. Following Bonneton et al. (2011), we added a quadratic friction term $f = c_f \frac{1}{h} |\boldsymbol{u}|\boldsymbol{u}$ to Eq. (4.1b) where the friction coefficient is $c_f = 0.0034$.

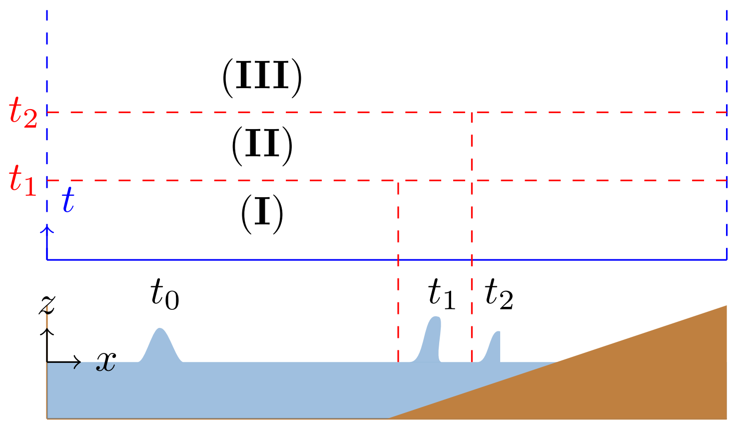

Figure 4.2: Schematic of the breaking process. The vertical dashed lines indicate the boundary of subdomains. The governing equations in the left subdomain are SGN and NSW equations elsewhere. The boundary follows the leading wave; (**I**) $t < t_1 :$ SGN in the whole domain, (**II**) $t_1 < t < t_2 :$ SGN in the left subdomain and SW in the right subdomain, and (**III**) $t > t_2 :$ NSW in the whole domain.

4.2.1 Initial and Boundary Conditions

We imposed the initial conditions

$$\zeta\left(x\right)|_{t=0} = H \,\mathrm{sech}^2\left[k_0(x - x_0)\right], \; \boldsymbol{u}(x)|_{t=0} = \frac{c\zeta}{\zeta + h_0}, \tag{4.2}$$

to generate solitary-type transient long waves (Madsen et al., 2008; Madsen and Schaeffer, 2010), in which $c = \sqrt{g(h_0 + H)}$ is the phase speed. H represents the initial wave height, c denotes the phase speed, and k_0 is the characteristic wave number. This wave type removes the constraint that exists between the wave height and the wave length and will result in a more realistic representation of tsunami waves (e.g. Baldock et al., 2009; Rueben et al., 2011; Irish et al., 2014) By choosing $k_0 = \sqrt{3H/4h_0^3}$, Eq. (4.2) will reduce to the free-surface elevation of a solitary wave with a permanent shape.

Table 4.1: Wave gauge coordinates.

		Location (m)		Location (m)		Location (m)
Gauge	1:	(18.24, 0.00)	2:	(24.43, 0.00)	3:	(29.28, 0.00)
Gauge	4:	(36.42, 0.00)	5:	(46.75, 0.55)	6:	(45.10, 2.18)
Gauge	7:	(44.34, 0.83)	8:	(48.40, 2.18)	9:	(45.65, 0.60)
Gauge	10:	(49.52, 1.10)	11:	(47.30, 2.18)	12:	(47.30, 0.00)
Gauge	13:	(42.90, 0.00)	14:	(45.10, 0.00)	15:	(47.85, 1.65)
Gauge	16:	(46.20, 1.10)				

4.2.2 Wave Breaking

We utilize the conditions suggested in Tissier et al. (2012) to estimate the start time of the breaking process. As noted earlier, NSW are employed as governing equations in the vicinity of the breaking-wave peak while modeling the rest of the domain using SGN. Here, we divide the computational domain into two sub-domains. The boundary that separates these two sub-domains follows the leading breaking wave (see Figure 4.2). We solve the domain behind the wave peak using SGN and the rest of the domain using NSW ($t_1 < t < t_2$ in Figure 4.2). The distance between the wave peak and the boundary is given by $x_b - x_w = 2h|_{x_w}$ where x_b is the coordinate of the boundary and x_w is the coordinate of the wave peak.

Note that in the very shallow areas, i.e., in the vicinity of the shoreline and the coastal areas, we always model the flow using NSW equations to avoid the numerical dispersions that can be caused by dispersive terms in SGN. In this study, we considered the run-up of a single wave. After the wave breaks completely ($t > t_2$ in Fig. 4.2), to increase the computational efficiency, we model the entire domain using NSW.

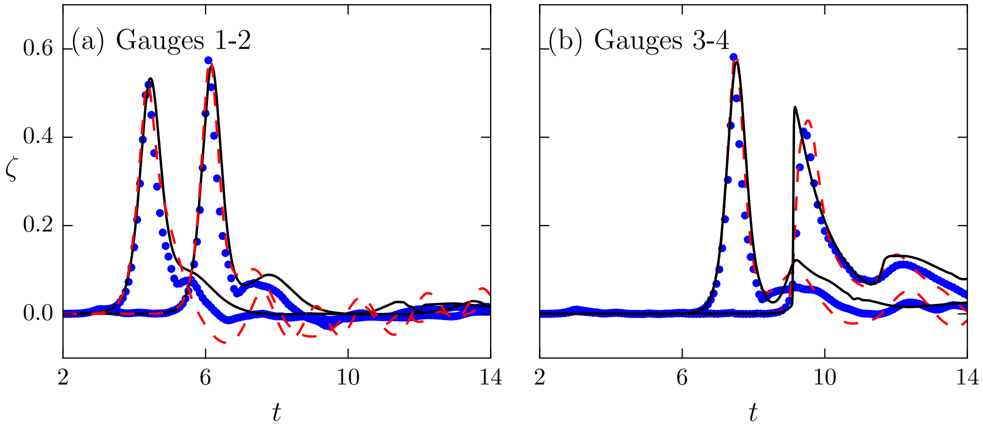

Figure 4.3: Free-surface elevation at (a) gauges 1-2, and (b) gauges 3-4. Experimental and COULWAVE results are summarized in Yang et al. (2016); (——) present simulation (2D-SGN), (●) experimental results and (- - -) COULWAVE.

4.3 Results

4.3.1 Validation of Numerical Results

Breaking Solitary-Type Transient Wave Run-Up

We investigated solitary-type transient wave run-up on a steep sloping beach (1:10) following the experimental setup in Irish et al. (2014). We discretized the computational domain (52 m, 4.4 m) using a rectangular uniform grid with $\Delta x = \Delta y = 52/1024$ m. The toe of the sloping beach is located at $x = 32$ m. The still water depth is $h_0 = 0.73$ m. The transient solitary wave is generated by setting $H = 0.50$ m, $k_0 = 0.54$ m^{-1}, and $x_0 = 10$ m at $t = 0$ s. A symmetry boundary condition is imposed on bottom and top boundaries.

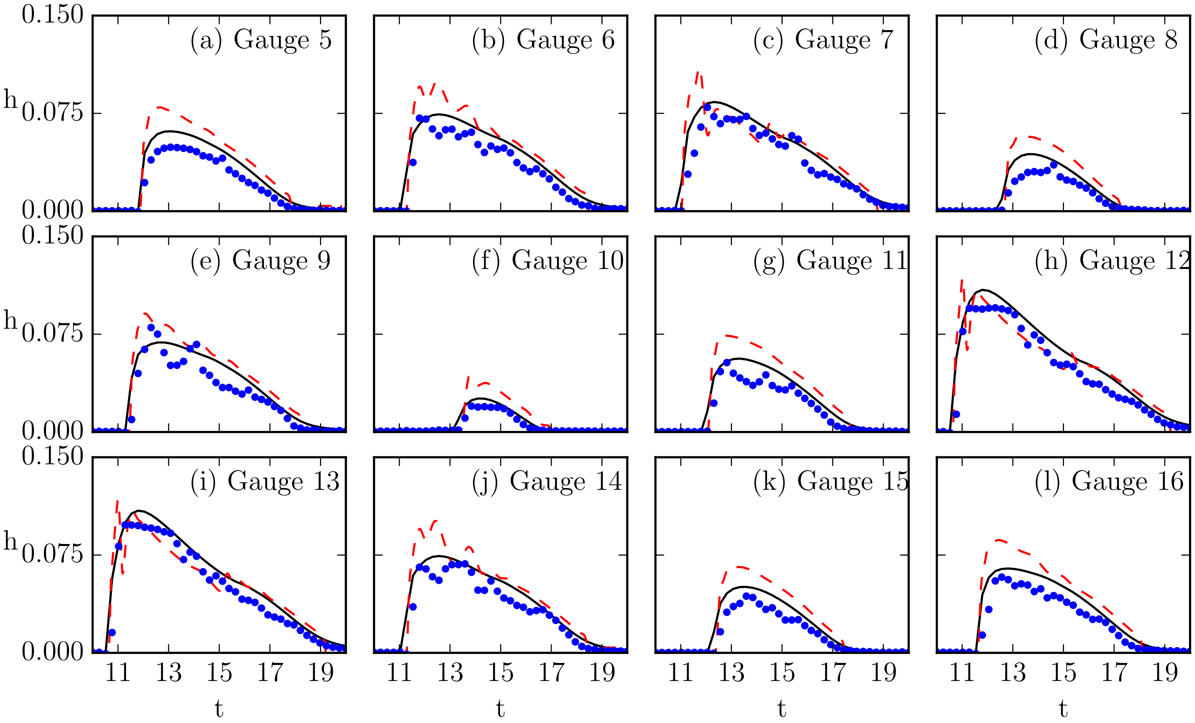

Figure 4.4: Local water depth at gauges 5-16. Experimental and COULWAVE results are summarized in Yang et al. (2016); (——) present simulation (2D-SGN), (●) experimental results and (- - -) COULWAVE.

Yang et al. (2016) studied this problem experimentally as well as numerically using COULWAVE (Cornell University Long and Intermediate Wave Modeling Package, Lynett et al., 2002) which solves the Boussinesq equations described in Liu (1994) and Lynett et al. (2002). We compared the free surface elevation (wave gauges 1-4) and the local water depth (wave gauges 5-16) with the results presented in Yang et al. (2016). The wave gauge coordinates are summarized in Table 4.1. Figure 4.3 shows the free-surface elevation ζ at gauges 1-4. While both methods capture the evolution of the free surface accurately, we observe that COULWAVE captures the breaking process slightly better. This can be due to the differences in the how wave breaking is handled. COULWAVE employs an ad-hoc viscosity model in the breaking process. In contrast, we solve NSW in the breaking zone and incorporate a shock-capturing scheme in the breaking process. Consequently, our model develops a steeper wave profile.

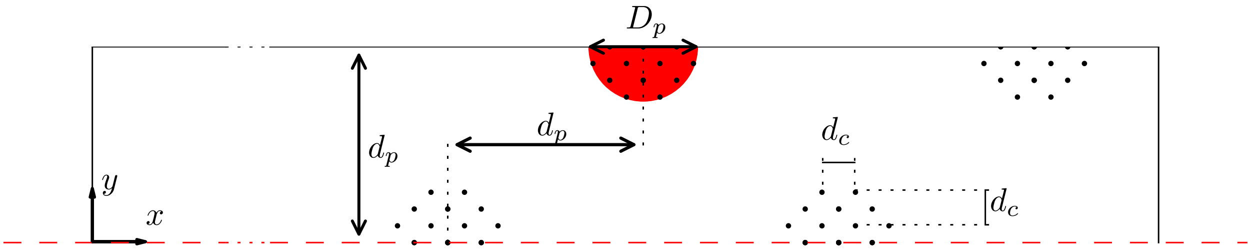

Figure 4.5: Sketch of the macro-roughness patches.

Figure 4.4 depicts the local water depth at onshore gauges 5-16. Our results are systematically closer to the experimental data. (Park et al., 2013) also reported about overpredicting the experimental results using COULWAVE. Yang et al. (2016) argued that the difference between the simulation and the experiment can be due to the existence of an slight leakage from the sloping beach among some other possible reasons. This can explain the slight overpredictions we observed using our model.

4.3.2 Breaking Solitary-Type Transient Wave Run-Up in the Presence of Macro-Roughness

A schematic sketch of the problem is shown in Figure 4.5. The computational domain, boundary conditions, and the initial conditions are the same as the ones in section 4.3.1. Three different scenarios are considered here. Each macro-roughness patch consists of regu-

Table 4.2: Geometrical parameters of macro-roughness patches. d_r : distance between two horizontally (or vertically) aligned cylinders inside a patch; N_{cp} : total number of cylinders inside a patch; d_p : distance between two horizontally (or vertically) aligned patches; C_{fp} : coordinate of the center of the first patch; D_c : diameter of the cylinders; D_p : diameter of the patches.

	d_r (m)	N_{cp}	d_p (m)	C_{fp} (m)	D_c (m)	D_p (m)
Scenario 1	0.1885	21	2.2	(34, 0)	0.01333	0.6
Scenario 2	0.0943	69	2.2	(34, 0)	0.01333	0.6
Scenario 3	0.1885	129	2.2	(34, 0)	0.01333	0.6

larly spaced vertical cylinders. The geometrical parameters of the patches for each scenario are summarized in Table 4.2. We used a nested mesh with

$$\begin{aligned} \Delta x = \Delta y &= 52/1024 \text{ m} \qquad x < 41 \text{ m}, \\ \Delta x = \Delta y &= 52/8192 \text{ m} \qquad x > 41 \text{ m}. \end{aligned}$$

Local water depth at gauges 5-16 is shown in Figure 4.6. The simulations are in good agreement with the experimental data. Some differences in transient wave peaks can be due to the ensemble-averaged experimental data. Ensemble averaging can smooth out some of the sharp transitions as suggested by Yang et al. (2016) and Baldock et al. (2009)

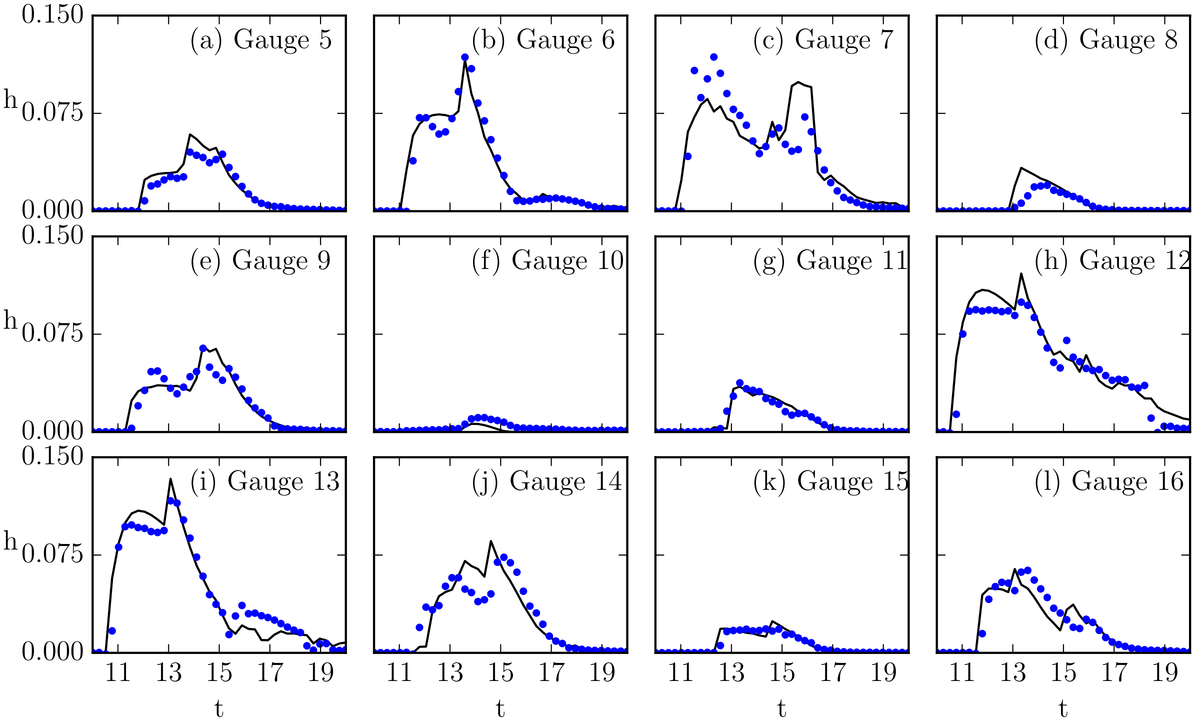

Figure 4.6: Local water depth at gauges 5-16 for Scenario 3. Experimental results are summarized in Irish et al. (2014); (——) present simulation (2D-SGN), and (●) experimental results.

4.3.3 Effects of Macro-Roughness on the Local Maximum Local Water Depth

The maximum local water depth is given by

$$h_{max} = \frac{\max(h) - \max(h)|_{ref}}{\max(h)|_{ref}}, \tag{4.3}$$

where $\max(h)|_{ref}$ is the maximum water depth in the absence of the macro-roughness patches. Unlike momentum flux we do observe water depth amplification up to 1.7 times behind the first patch in the presence of the macro-roughness patches. When the flow reaches the first patch the flow refracts away from the center of the patch toward the other patches. However, the patches located in the second row refract and reflect the water toward the centerline. This process causes the water to amplify behind the first patch (red area in Figure 4.7). As we can see in Figure 4.7(d), no amplification in local water depth occurs behind the patch in the case were all other patches are removed.

4.3.4 Effects of Macro-Roughness on the Local Maximum Momentum Flux

The momentum flux represents the destructive forces of the incident wave. To study the effects of the macro-roughness patches on momentum flux we defined the maximum normalized momentum flux as

$$F_{max} = \frac{\max(h|\boldsymbol{u}|^2) - \max(h|\boldsymbol{u}|^2)|_{ref}}{\max(h|\boldsymbol{u}|^2)|_{ref}}, \tag{4.4}$$

where $\max(h|\boldsymbol{u}|^2)|_{ref}$ is the maximum momentum flux in the absence of the macro-roughness patches. Figure 4.8 shows the F_{max} for Scenarios 1-3. We can see that the patches provide protection for the areas behind them for Scenario 1 (Figure 4.8(a)). With increasing density of the cylinders in patches, F_{max} is decreased. Thus the level of protection against incident waves increases. However we did not observe any significant changes with further increasing the density of the cylinders (see Figure 4.8).

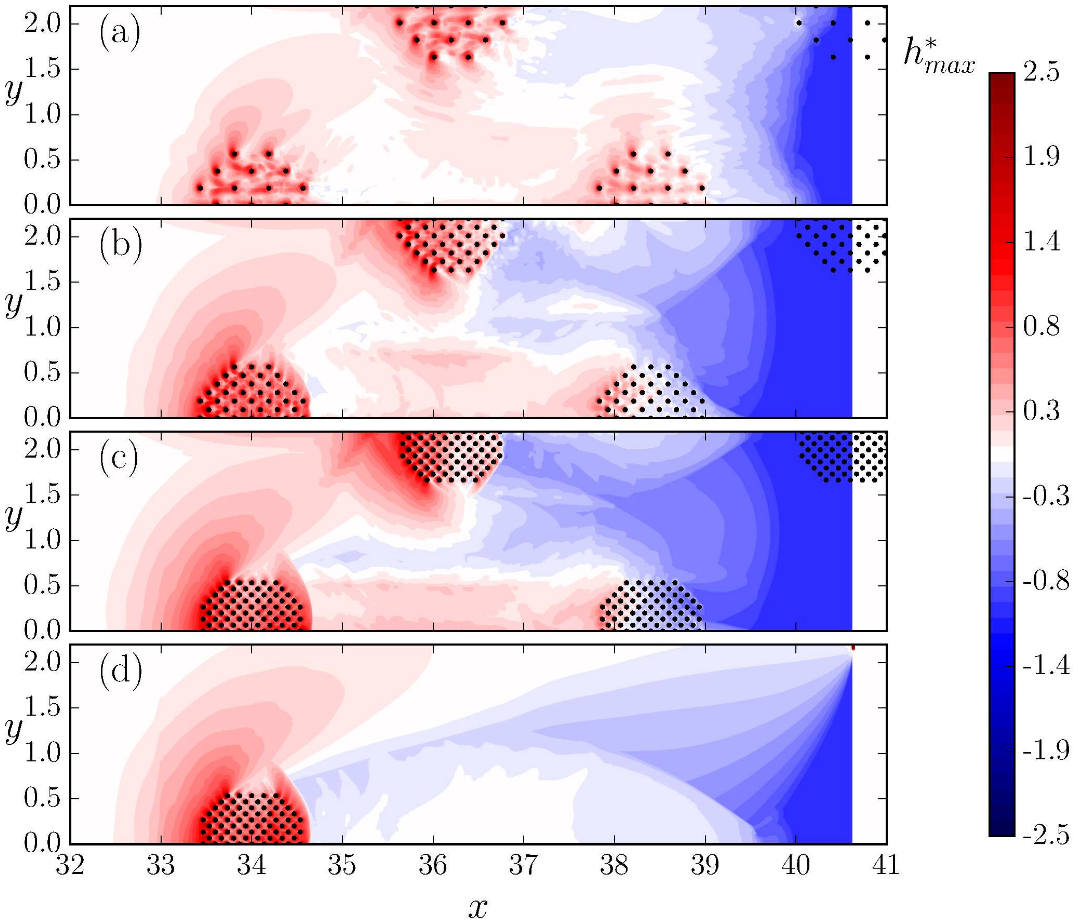

Figure 4.7: Maximum local water depth h^*_{max} for (a) Scenario 1, (b) Scenario 2 (c) Scenario 3, and (d) Scenario 3 in which all the patches are removed except the first patch. The maximum water depth for each scenario is normalized with the reference values in the absence of macro-roughness patches.

4.3.5 Maximum Run-Up

Maximum run-up is another important criteria in determining the effectiveness of the macro-roughness patches in mitigating tsunami hazard risks. Figure 4.9 shows the comparison of the simulation to the experimental results of the bore line propagation for the Scenario 2. The results are in good agreement. The maximum deviation from the experimental results is less than 4%.

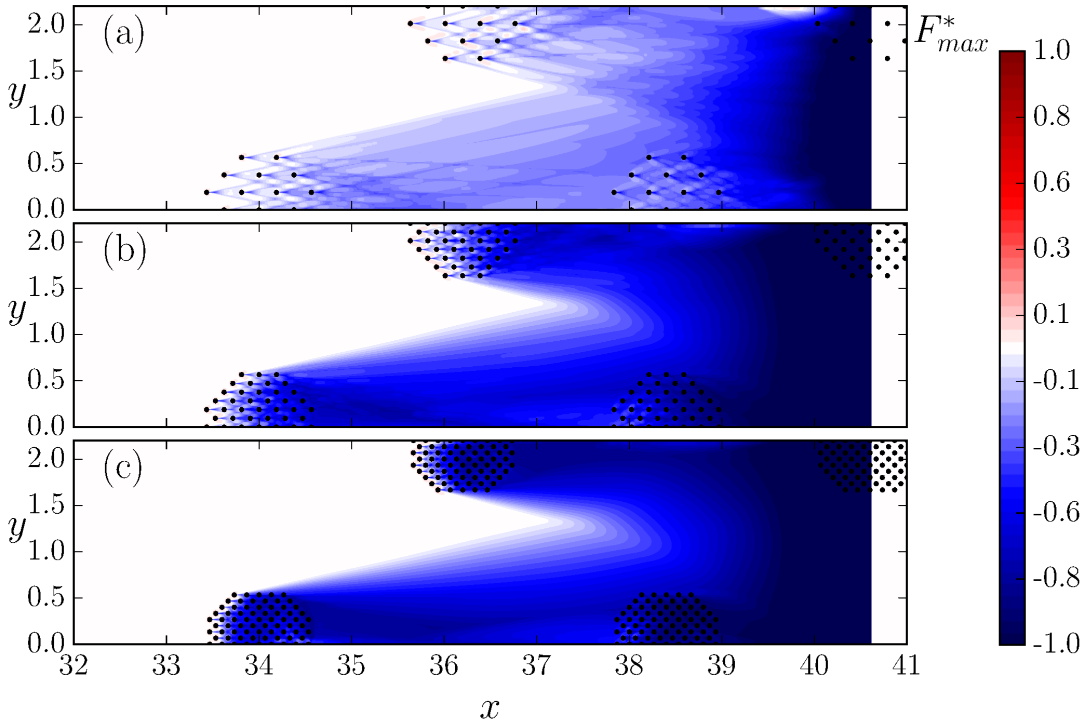

Figure 4.8: Maximum momentum flux F^*_{max} for (a) Scenario 1, (b) Scenario 2, and (c) Scenario 3. The momentum flux for each scenario is normalized with the reference values in the absence of macro-roughness patches.

Figure 4.10 shows the bore-line propagation for different Scenarios. The maximum run-up decreases with increasing the vegetation density inside the macro-roughness patches. For the very low density vegetations (Fig. 4.10(b)) this reduction is more or less uniform along the shore. However with increasing the vegetation density (Figure 4.10(c)) we observe more reduction behind the patches. With further increasing the vegetation density (Figure 4.10(d) in comparison to Figure 4.10(c)) while the maximum run-up behind the patches continues to decrease, it increases within the channel between the patches slightly. The reason for this increase is the level by which the flow is channelized between the patches.

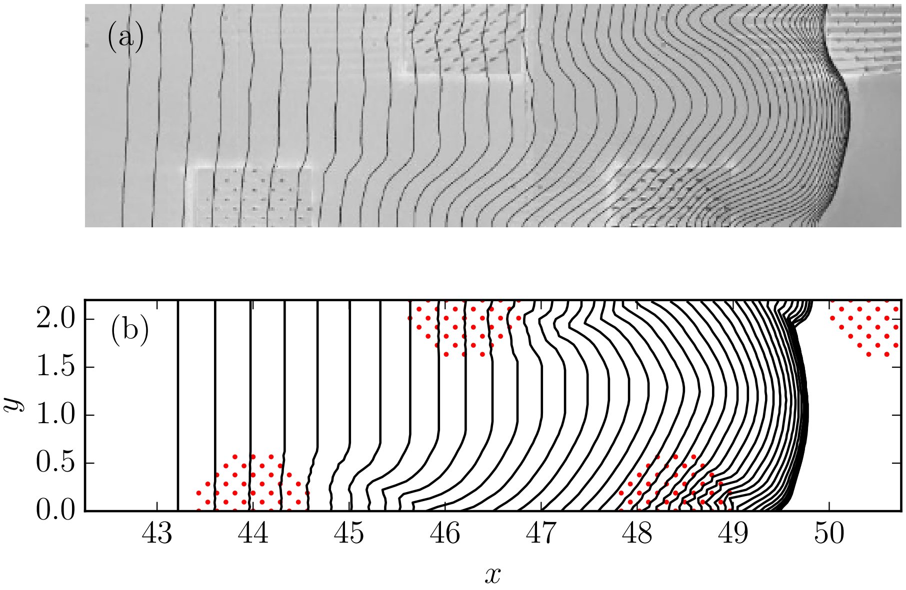

Figure 4.9: Propagation of bore-lines in the presence of macro-roughness patches (Scenario 2). Irish et al. (2014); (a) experimental results, and (b) present simulation (2D-SGN).

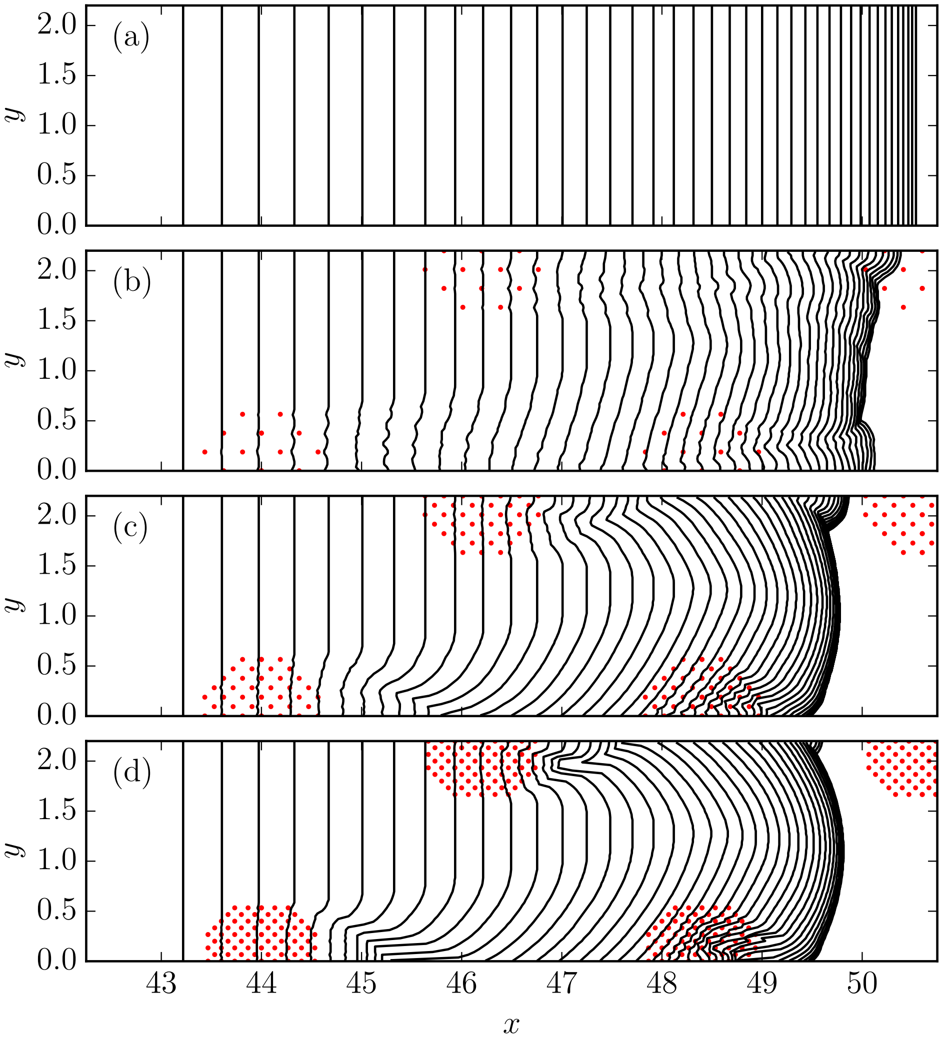

Figure 4.10: Propagation of bore-lines for (a) Scenario with no macro-roughness patches (b) Scenario 1, (c) Scenario 2 (d) Scenario 3.

4.4 Discussion and Conclusion

We presented numerical simulations of long water waves interacting with emergent cylinders. We demonstrated that higher order depth integrated equations, such as SGN, are a suitable tool to simulate the wave interaction with emergent cylinders accurately except in very close vicinity of the cylinders. Three-dimensional effects cannot be ignored at the proximity of the cylinders and we argue that they are the main reason for the existing differences between results from our model and the experimental data.

Cylinders, representing coastal vegetation, are usually approximated as macro-roughness friction (e.g. Yang et al., 2016; Mei et al., 2011). However there is no analytical solution for a correlation between macro-roughness patterns and the implemented friction coefficient. Thus these models need to be calibrated against available experimental data. However for scenarios with no experimental prototype these models can become inaccurate. Here, with further refining the grid in the coastal areas, we modeled these macro-roughness patches as physical boundaries.

We observed that discontinuous coastal vegetation can provide protection for the areas behind them. Friction forces become dominant when the flow becomes shallower. In addition, for the areas located on the onshore slope we also have the gravitational force acting in the negative flow direction. Macro-roughness patches elongate the path of the incident wave, causing a longer local inundation period. Thus the flow will be subjected to the negative gravitational and friction force for a longer time and the maximum recorded velocity will decline in comparison to the scenario where no macro-roughness patches exist. This will lead to a reduced local momentum flux and increased protection against the destructive wave force. However, in terms of local maximum water depth this conclusion does not apply. Even though the decreased local velocity will result in more protection against the wave, we observed for the studied macro-roughness the maximum local water depth actually increases behind the patches. We observed amplifications up to 1.6 times in local water depth. This will increase the chance of that area being flooded. We note here that the main reason the Fukushima Daiichi nuclear disaster happened was the fact that the water overtopped the protecting wall and reached the electric generators (Synolakis and Kânoğlu, 2015).

We demonstrated the capability of the model in analyzing the wave interaction with coastal structures. However, our study was limited to the emergent cylinders and simple macro-roughness patch patterns. Studying submerged coastal vegetations and different patch patterns will be the direction of our future studies.

Chapter 5

Effects of Coastal Vegetation in Reduction of Runup of Tsunami Waves

[†]**Note:** Authors, Marivela-Colmenarejo R., Zainali A, Weiss R., Irish J.L. and Yang Y., consider that this manuscript will be submitted to the Ocean Engineering journal in the near future.

5.1 Abstract

Field observations of the after effects of the 2004 Sumatra and the 2011 Tōhoku tsunami have indicated the important role of the coastal vegetation in affecting tsunami wave runup. By using the Serre-Green-Naghdi equations, we study how an onshore vegetation barrier modifies the tsunami runup under variations of barrier length, barrier width, barrier location, tsunami wave amplitude and beach slope. We employ homogeneous staggered distributions of rigid and emerged cylinders to represent the trees of the vegetated barrier. The numerical model is validated by comparison with laboratory experiments where vegetation is represented by staggered cylinder patches distributed on the coast. Our results indicate that a minimum barrier length is required to achieve the maximum runup reduction associated with each configuration and that the effectiveness of the barrier in reducing the runup increases with its proximity to the shoreline. We propose methods to estimate the maximum runup reduction and the minimum required barrier length. We conclude that wave amplitude and barrier length are the most important factor to obtain the runup, while barrier location is the most important to define the minimum barrier length.

5.2 Introduction

Numerous field observations after coastal inundations have shown that the presence of onshore vegetation affects the runup process. In fact, coastal vegetation has been widely promoted for the purpose of reducing the impact of large storm surges and tsunami (e.g. Feagin et al., 2010). Depending on its density and location, coastal forest is able to increase land's stability versus erosion and reduce significantly the destructive impact of a flooding event, such hurricanes or tsunamis. For instance, the destructive pattern of the 2004 Sumatra Tsunami was irregularly distributed around the coast because the non uniform trees groups presence and, although there are other ways for wave attenuation (Anderson and Smith, 2014; Tanaka, 2009; Mendez and Losada, 2004), the role of coastal forest becomes important in reducing the inundation hazards at the shoreline environment and inland. However, still there is long way to quantitatively determine more exactly the effect of the vegetation presence on the inundation process. This lack of information does not let the use of these natural resources to be used more broadly to save marine infrastructures and avoid damages. This knowledge becomes even more important if the eventual sea level rise generated by global warming is taking into account, which will lead to more vulnerability of the coastal environments under flooding events.

Therefore, there is a need of better understand the effects of onshore environments on the energy dissipation of the wave during runup. Although wave breaking and inundation imply energy dissipation, which depends on wave physical properties such as wave height, water depth and beach slope, there is an additional dissipation of energy as the wave reaches and passes through vegetated areas. This extra dissipation highly depends on the surface of the tree trunks facing the wave and on the number of impacts of the wave against them while it passes through, so dimensions of the vegetated areas play an important role in the dissipation. The exact amount of energy dissipated during this process is not easy to quantify because the flow develops with high turbulence. However, the runup reduction resulting from the vegetation not only provides a good measurement of the dissipated energy (Tanaka, 2009) but also delineates the zero hazard zone which is important for coastal protection.

as a consequence of the extra dissipation of energy, the resulting runup reduction after the vegetated area not just provides an overall good measurement of the dissipated energy (Tanaka, 2009), it also

Numerical modeling of tsunami dynamics has achieved relevant progress in determining the runup of waves under a broad range of scenarios. Feagin et al. (2010) studied the influence of the coastal vegetation on the wave runup. They observed that when trees were placed in a dense rectilinear pattern and close to the shoreline, the runup was reduced by approximately 45% compared with the control case. Thuy et al. (2009) focused on the effects of an open gap in a coastal forest on tsunami run-up. They concluded that the flow velocity at the end of the open gap increases up to 1.7 times compared with the maximum velocity without a coastal forest. They also observed that the flow velocity at the same location can be reduced by a staggered arrangement of the coastal forest. However there is a transition zone between where the barrier affects the flow the most and where the flow is not affected by the barrier at all. In this work we will study the transition zone in order to identify the effectiveness of the vegetated barrier in decreasing the wave runup.

Management of evacuation strategies still do not fully consider the interaction between tsunami wave and coastal forest, mainly, because still it is not very well understood due to the fact that vegetation has its own biological dynamics, random densities and spatial discontinuities which creates an even more complex problem (Thuy et al., 2012). To simplify this fact we study coastal vegetation barrier with same density and distribution of trees. In this contribution we determine the resulting runup after the vegetated barrier based on different solitary waves amplitudes and based on the length, width and location of the barriers. Our results provide useful information to estimate the runup behind the barrier under different barrier configurations for coastal hazard mitigation purposes.

5.3 Theoretical background

Our simulations use solitary waves approaching the beach with $\mu = \frac{h_0^2}{\lambda} << 1$ where h_0 is the initial water depth and λ id the wave length. When the parameter $\varepsilon = \frac{H}{h_0}$ is equal to $O(\mu)$, being H the wave height, an approximation of $O(\mu^2)$ can be used to represent the Euler formulae of the free surface by the Boussinesq equations (Peregrine, 1967). For keeping the $O(\mu^2)$ approximation also in large amplitude regime we use Serre-Green-Naghdi (SGN) equations:

$$\begin{cases} \partial_t h + \nabla \cdot (hu) = 0, \\ \partial_t (hu) + \nabla \cdot \Big(hu \times u + \frac{1}{2} g h^2 I \Big) = -gh \nabla b + D \end{cases} \tag{5.1}$$

where D denotes a nonlinear function of the free surface and I the identity tensor. These fully nonlinear and weakly dispersive type-equations represent accurately the wave approximation from deep to shallower water and we employ them until the breaking starts. From here we switch to nonlinear shallow water equations (NSW) by setting D*=0* in 5.1. For more detailed information about SGN equations we refer to Lannes and Bonneton (2009) and Bonneton et al. (2011).

We use Basilisk code (Popinet, 2015) and characterize the domain into before and after breaking areas to solve the governing equations as follows:

- Before time of breaking start: SGN equations in the entire domain

- During breaking: SGN equations up to the breaking area and NSW equations in the rest of the domain
- After breaking ends: NSW equations in the entire domain.

5.3.1 Setup and boundary conditions

We use the surface profile of solitary wave, η, presented in Synolakis (1987)

$$\eta(x,0) = H\,sech^2\left[\sqrt{\frac{3H}{4h_0^3}}(x - x_0)\right] \tag{5.2}$$

where h_0 is the initial water depth and x_0 is the x-location of the the maximum initial wave height, H, measured from the still water surface.

5.4 Results

5.4.1 Validation

The effects of patchy coastal forest on the runup of a solitary wave was studied in experiments presented in Irish et al. (2014). The 1:10 beach toe was located at 22 m from the wave maker, $h_0 = 0.73$ m, $H = 0.50$ m and the wave number was $3H/4h_0^3 = 0.54$ m^{-2} at the wave maker. Vertical staggered segments of PVC pipes were used as vegetation on patches. Different number of cylinders per patch were studied to form two macro-roughness scenarios where the distance between cylinders was 0.267 m for scenario 1 (S1) and 0.134 m for scenario 2 (S2). The array of staggered patches remained fixed in both scenarios. Sonic wave gauges

Table 5.1: Wave gauge coordinates.

	Location (m)	Location (m)	Location (m)	Location (m)
Gauge	1: (46.75, 0.55)	2: (45.10, 2.18)	3: (44.34, 0.83)	4: (48.40, 2.18)
Gauge	5: (45.65, 0.60)	6: (49.52, 1.10)	7: (47.30, 2.18)	8: (47.30, 0.00)
Gauge	9: (42.90, 0.00)	10: (45.10, 0.00)	11: (47.85, 1.65)	12: (46.20, 1.10)

(50Hz) were used to measure water depth at locations shown in Table 5.1. For validation we compare the time series of water depth between and experiments and simulations for S2 in Fig. 5.1.

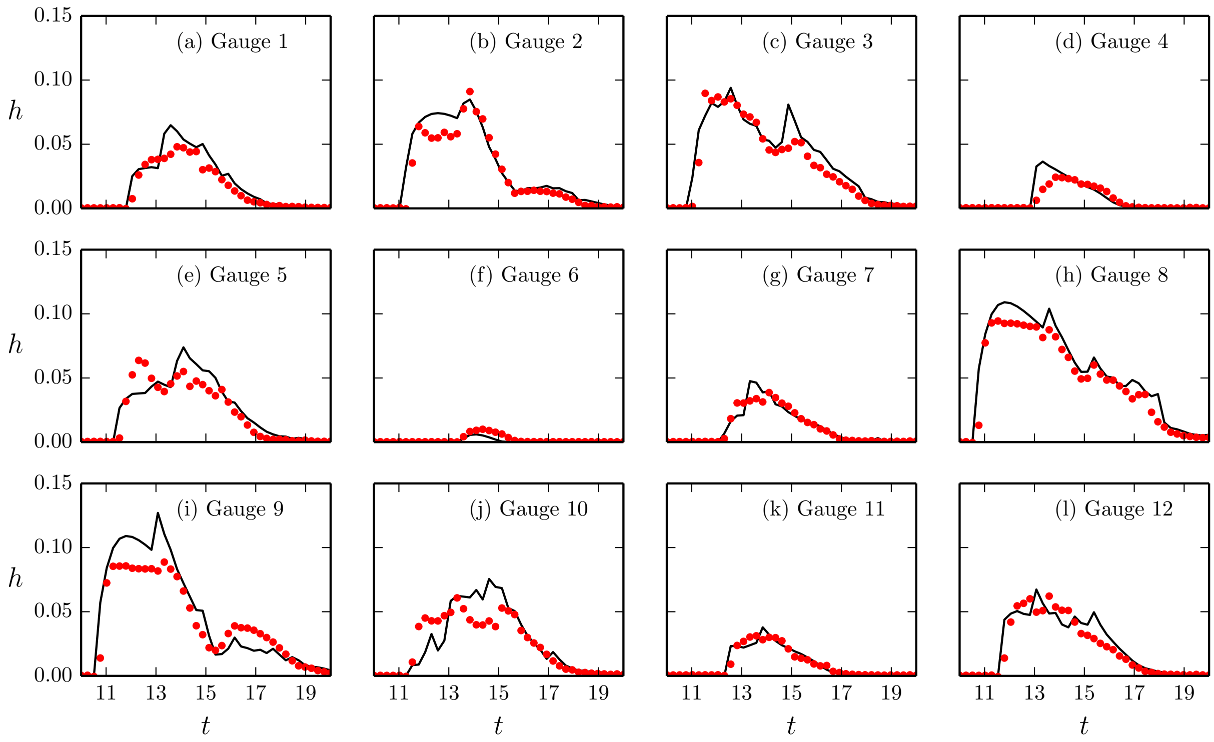

Figure 5.1: Comparison of local water depth at gauges 1-12 for Scenario 2 between 2D-SGN simulation (●) and experimental results presented in Irish et al. (2014) (——).

The H/h_0 ratio of this solitary wave is large, 0.685, which indicates a high turbulence of the flow during and after the wave breaking. Additionally the multiple stems in the flow trajectory provide extra turbulence due to: a) sequence of impacts of the flow against the cylinders and b) strong channeling and refraction of the flow between the patches. Taking these considerations into account we observe that the comparison of the water depth between experiments and simulation shown in Fig. 5.1 is excellent, especially when most of the gauges are located behind one patch at least, where the effects of multiple refractions are more intense.

5.4.2 Effects of macro-roughness patches on final runup

Yang et al. (2017) presented experiments results of an additional scenario based of the Irish et al. (2014) experiments. We refer to it as scenario 3 (S3). We show the runup evolution and the maximum runup from our simulations for control scenario (without vegetation) and scenarios 1-3 in Fig. 5.2a-d respectively. Although the number of PVC cylinder in S3 is double than in S2, we observe that the final runup of S3 is not lower than the final runup of S2. Of the three cases, maximum runup reduction is reached in S2 case so, from Fig. 5.2, we consider S2 scenario is the most efficient in reducing the final runup. For these reasons we select S2 setup (Irish et al., 2014; Yang et al., 2017) for our research.

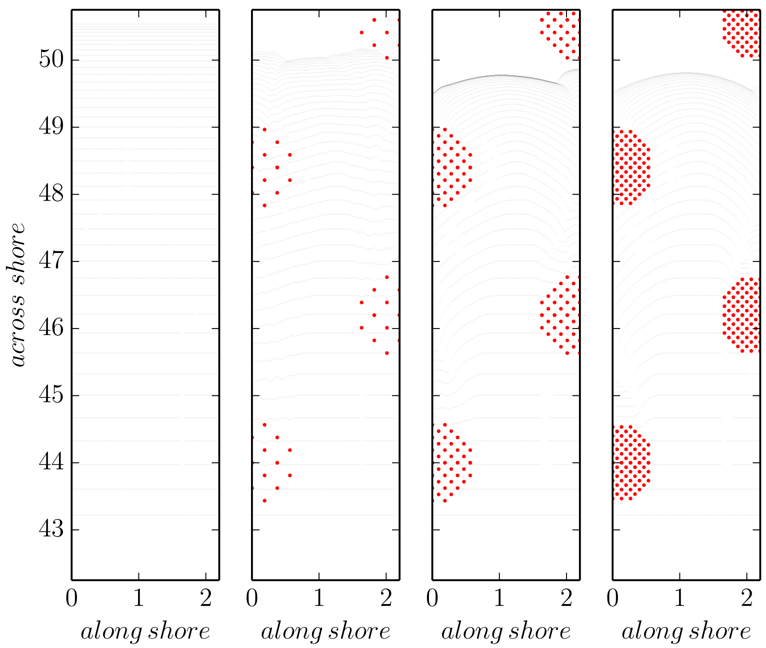

Figure 5.2: Propagation of bore-lines for (a) Scenario with no macro-roughness patches, (b) Scenario 1, (c) Scenario 2 and (d) Scenario 3.

5.4.3 Runup of solitary wave in presence of vegetated barrier

From experiments and simulations we observe that, as the flow progresses through the beach with patches, two kinds of refractions are generated from the impacts of the flow against the cylinders. The first kind are short-refractions which just develop in the stems environment because they interact intensely with each other so have short lifetimes. The second kind are long-refractions and, because they are generated in the patches edges, part of them escape from the short-refraction interactions and travel towards the channelized flow located between patches. As also observed in Yang et al. (2017) and in Zainali et al. (2016), long-refractions interact with each other as well, but with less intensity. The large number of interactions between short-refractions leads to flow energy loss inside and in front of the patches. As consequence, the runup behind the patches decreases. However this soon is affected by some of the long-refractions interactions that occurs behind the patches as well, increasing the flow momentum, so also the final runup. An increase in the momentum flux results in an increase in the water depth and turbulence of the flow behind the patches when compared to control scenario. This represents a more dangerous situation than in the case without patches. Therefore to reach the maximum runup reduction due to the patches, it is necessary to avoid the interaction between long-refractions. We do so by increasing the along shore length of the patches, so the long-refraction originated from both sides of the patch do not reach to interact with each other. For this reason we simulate just one long patch to which we refer as barrier from now. With just one barrier, the short-refractions are intensified and just two long-refractions occur and if the barrier is long enough they do not interact with each other so the stems are used more efficiently in the barriers when compared with patches.

As Fig. 5.3 illustrates, the flow is not only affected by the vegetation barrier in areas strictly behind the barrier. There is a transition zone created by the reach of a long-refraction and defined as when the runup starts to decay from its maximum value, R, and where the runup reaches its minimum value due to the barrier, R_b. We describe the transition zone by using $\mathcal{D}$ and $\mathcal{L}$. $\mathcal{D}$ indicates the alongshore distance measured from the barrier edge until where the runup starts to be influenced by the vegetation barrier. $\mathcal{L}$ represents the minimum alongshore barrier length required to achieve R_b. Note that if the barrier length $< \mathcal{L}$, the resulting runup behind the barrier would be larger than R_b and is determined by the transition curve R-R_b.

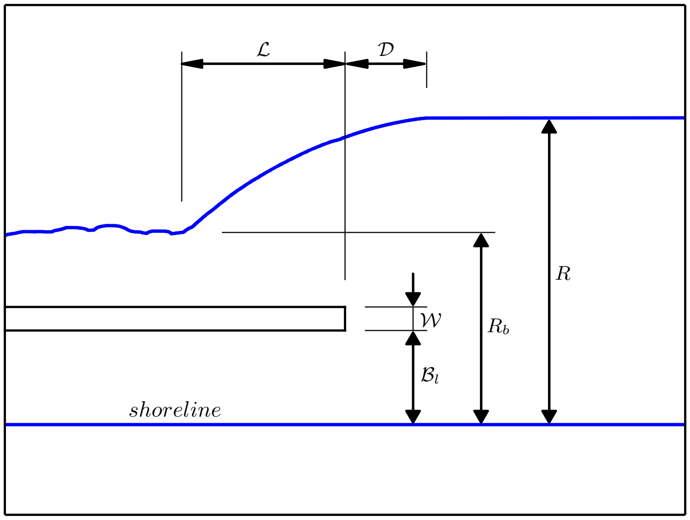

Figure 5.3: Top view of the beach numerical setting. R_b represents the maximum reduced runup after the barrier. $\mathcal{L}$ represents the alongshore distance between the barrier edge and R_b and $\mathcal{D}$ is the alongshore distance measured from the barrier edge until where the runup is not affected by the vegetated barrier at all, R. The barrier location and barrier width are represented by $\mathcal{B}_l$ and $\mathcal{D}$ respectively.

We analyze R_b, $\mathcal{L}$ and $\mathcal{D}$ as function of: 1) barrier width, $\mathcal{W}$; 2) solitary wave ratio, H/h_0; 3) beach slope, α; and 4) barrier location, $\mathcal{B}_l$. We carry out a simulation for each combination of the following values: $\mathcal{W}$ = 1.13, 0.94, 0.75 and 0.56 m represented by the following symbols respectively: ▲, ■, ● and ▼; H/h_0 = 0.45, 0.40, 0.35, 0.30, 0.25 and 0.20 represented by the following colors respectively: 🟦 , 🟥 , 🟦 , 🟧 , 🟩 and 🟪 ; α = 1:10 and 1:20 represented without and with additional cross in their respective symbols respectively; and $\mathcal{B}_l$ = 2.62, 3.62 and 4.62 m onshore measured from the still water shoreline and represented by small, medium and large symbols respectively. A total of 144 simulations are developed and we obtain one value of R_b, $\mathcal{L}$, and $\mathcal{D}$ per simulation for analysis.

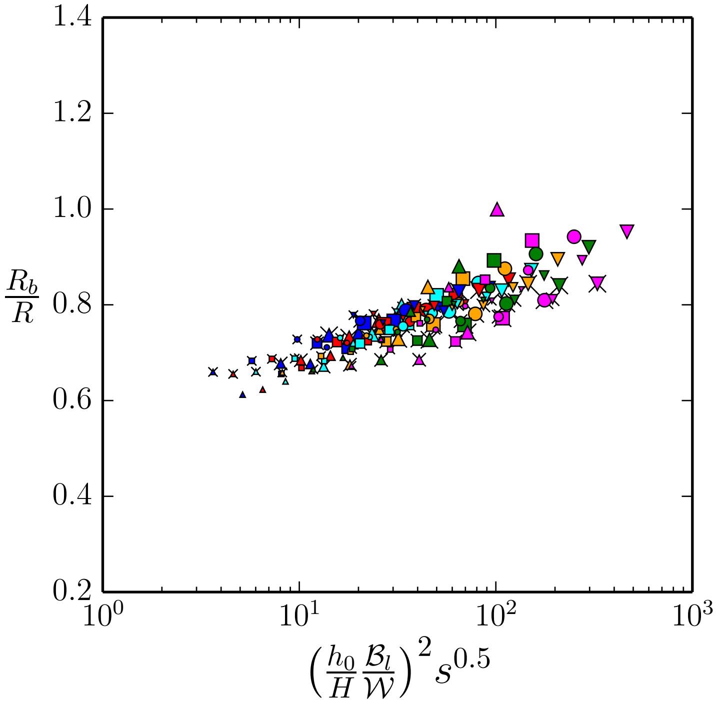

Figure 5.4: Normalized runup behind the barrier, R_b/R, versus $(h_0\mathcal{B}_l)^2/(H\mathcal{W})^2 \cdot s^{0.5}$. Note that horizontal axis is in logarithmic scale. $H/h_0 = 0.45$(🟦), 0.40(🟥), 0.35(🟦), 0.30(🟧), 0.25(🟩) and 0.20(🟪); $\mathcal{W}$ = 1.13(▲), 0.94(■), 0.75(●) and 0.57 m (▼) and $\mathcal{B}_l$ = 2.62, 3.62 and 4.62 m onshore measured from the still shoreline and represented by small, medium and large symbols respectively. Results from 1:20 simulations are additionally represented with a cross.

We show in Fig. 5.4 the normalized runup behind the barrier, $\frac{R_b}{R}$, versus $\left(\frac{h_0}{H}\frac{\mathcal{B}_l}{\mathcal{W}}\right)^2 s^{0.5}$ in logarithmic scale. Note that the R_b/R relationship indicates the percentage of R_b over R so the the lower R_b/R, the more efficient the barrier configuration is to decrease the tsunami inundation. We observe that R_b/R decreases as H/h_0 and $\mathcal{W}$ increase and as $\mathcal{B}_l$ decreases. There is a discrepancy between the data trend and the point from $H/h_0 = 0.20$ simulations. This is because the resulting reduced inundation of $H/h_0 = 0.20$ wave ends very close the barrier edge, resulting in a noisy data for this wave. However this data is still in the overall trend.

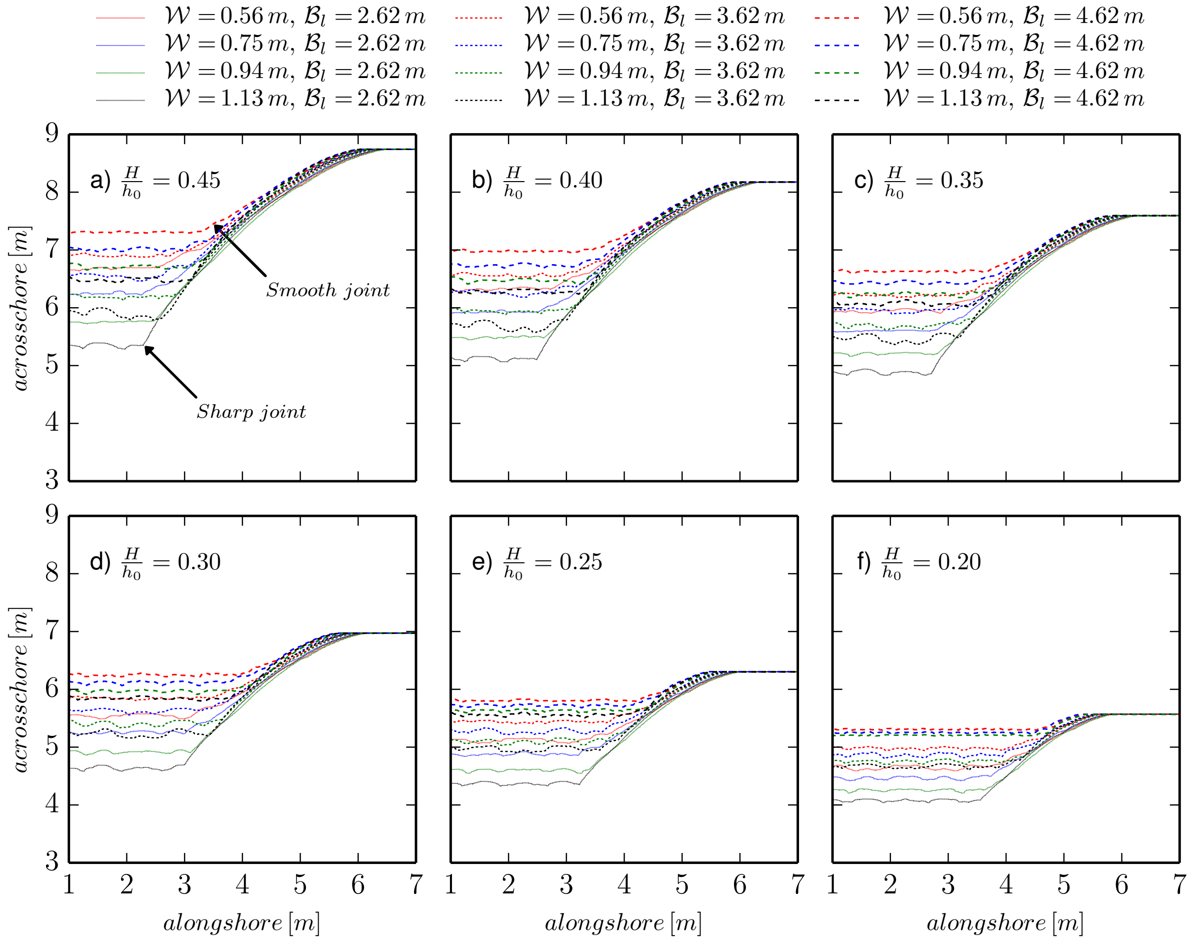

Figure 5.5: Resulting runup inundations behind vegetated barrier with different widths, $\mathcal{W}$, and locations, $\mathcal{B}_l$, up to a 1:10 beach slope for six different solitary wave amplitudes: a) $H/h_0 = 0.45$, b) $H/h_0 = 0.40$, c) $H/h_0 = 0.35$, d) $H/h_0 = 0.30$, e) $H/h_0 = 0.25$, f) $H/h_0 = 0.20$. Examples of sharp and smooth joints are indicated by arrows. Note that the barrier is located in the left area and its edge is located at $x = 5$ m.

We show the resulting inundations behind vegetated barrier, with different $\mathcal{W}$ and $\mathcal{B}_l$, up to the 1:10 beach slope for H/h_0 = 0.45, 0.40, 0.35, 0.30, 0.25 and 0.20 wave amplitudes in Fig. 5.5a-f respectively. There are three parts to the inundation runup: The first one is located at the right of each subplot where the inundation is not affected by the barrier. The second, located at the left, is where the inundation fully affected by the barrier. The third, located between the previous two, represents the transient curve. The joint between the transient curve and R_b varies (as examples see what arrows indicate in subplot a) and hence the $\mathcal{L}$ determination is affected accordingly. To correct this effect I propose to analyze the following in detail:

- The joint is sharp when R_b is small, which is determined by small values of $\mathcal{B}_l$ and large values of $\mathcal{W}$.
- When R_b is large, the joint is smoother, which introduces noise to determining $\mathcal{L}$.
- From Fig. 5.5, $\mathcal{W}$ adds more noise than $\mathcal{B}_l$. Hence, simulations with $\mathcal{W}$ = 0.56 m always provide smooth joints regardless of the H/h_0 value.

So I propose the following methods to obtain a reliable $\mathcal{B}_l$ determination:

- 1) To study the smooth joint between the transient curve and R_b and to investigate if their pattern are $f(\mathcal{W}, \mathcal{B}_l, H/h_0, s)$.
- 2) To obtain $\mathcal{L}$ using the joint of numerical-approach-transient curve with R_b and, additionally, by introducing an error = $f(\mathcal{W}, \mathcal{B}_l, H/h_0, s)$ that represents smooth joints.

5.5 Discussion

The effect of coastal vegetation in reducing tsunami inundation has been a very interesting topic (Thuy et al., 2009) and different investigations have been carried out to better understand the tsunami mitigation by: forest structures of mangroves (Maza et al., 2015; Strusinska-Correia et al., 2013; Ismail et al., 2012), submerged vegetation (Wang et al., 2015; Zhu and Chen, 2015; Mendez and Losada, 2004) or even coastal structures (Tang et al., 2017; Goseberg, 2013; Nandasena et al., 2012). Also patchy vegetation has been studied for reducing the tsunami runup (Yang et al., 2017; Irish et al., 2014; Irtem et al., 2009; Nandasena et al., 2008). Very few studies have been carried out to investigate the effect of varying locations of objects in the mitigation of tsunami waves and, as per our simulations, the onshore location of the vegetation barrier plays a very important in role it. However the wave amplitude is the most important factor in the reduction of the tsunami inundation as per Fig. 5.4 and and especially Fig. 5.5. This means, counterintuitively, that for larger values of H/h_0 the lower the R_b/R becomes, which implies an implicit and natural feature of vegetation in protecting coastal environments, regardless of the values of $\mathcal{B}_l$, $\mathcal{W}$ and α. This is because the higher the H/h_0 ratio, the higher the stems-flow and flow-flow interactions, which intensifies the short-refractions. This, in turn, limits the flow discharge through the barrier which leads to a larger reduction of R_b.

The next factor that influences R_b/R is $\mathcal{W}$. This can be observed for low values of $\mathcal{B}_l/\mathcal{W}$ in Fig. 5.4 and in 5.5: R_b/R increases more when $\mathcal{W}$ varies and $\mathcal{B}_l$ is fixed (observe symbols of the same size) than when $\mathcal{B}_l$ varies and $\mathcal{W}$ remains fixed (observe symbols with the same shape). This is because, as we mentioned before for the influence of H/h_0, higher $\mathcal{W}$ means more stems in the barrier width, which leads into a limitation of the flow discharge through the barrier, increasing aforementioned stems-flow and flow-flow interactions as well.

However, although the influence of $\mathcal{B}_l$ is lower than $\mathcal{W}$, it is also very relevant as we mentioned before, and it is almost as much important as $\mathcal{W}$ is. The effectiveness of the vegetation in reducing the runup (high values of R_b/R) increases as $\mathcal{B}_l$ decreases. This is because the closer the barrier is to the shoreline, the more intense the flow interacting with the barrier are, which is when the flow discharge (or momentum) is high. These high intense interactions provide a loss of energy as the flow impacts with itself and against the barrier stems. Marivela et al. (2016) observed that maximum flow momentum of the tsunami wave occurs closely to the shoreline. So the closer the barrier to the shoreline, the higher the effectiveness of the barrier in reducing the tsunami inundation, assuming that the stems stand the tsunami impact. In Fig. 5.4 we observe that the distributions of the points for different α do not provide significant difference of R_b/R, which indicates that α does not represent a factor of R_b/R alteration. This is valid for beaches whose slopes are between 1:10 and 1:20 and for cases with the same setup as our simulations.

Although the maximum runup reduction is the main goal of the vegetation barrier, in Fig. 5.3 we observe that this goal cannot be achieved unless the barrier length is at least $\mathcal{L}$ long. From our simulations we observe that transition curves from R to R_b, created by the long-refraction, are very similar regardless of $\mathcal{W}$ and $\mathcal{B}_l$. The major difference between these curves is their meeting point to R_b, which depends on $\mathcal{B}_l$ and $\mathcal{W}$ as we discussed earlier. However, $\mathcal{B}_l$ is the most important factor as there are three distributions of points, each one associated to each value of $\mathcal{B}_l$ employed. This is because the later the long-refraction initiates (higher values of $\mathcal{B}_l$), the lower the momentum of the long-refraction gets, which makes the long-refraction weaker and more susceptible to variations due to the high turbulent flow that crosses the barrier. The barrier influence not only rigorously affects areas behind it, but also its influence reaches up to a alongshore $\mathcal{D}$ distance, measured from the barrier edge.

Moreover $\mathcal{D}$ also determines the limit where the runup is not affected by the barrier at all (Fig. 5.3).

5.6 Conclusions

Numerous studies have been carried out to determine the resulting runup due to the presence of onshore and offshore vegetation. Most of these studies consider barrier length as large as the domain width, so one could assume that the resulting runup behind the barrier is the same, as long as we consider any area behind the barrier. This assumption is not true and dangerously lacks safety since it does not consider the transition inundation zone located between where the runup shows its maximum reduction and where the runup is not affected by the barrier at all. Additionally, numerous studies do not study the influence of different location of the barrier, or patches, in reducing the runup, or in defining the transition zone.

To cover these lacks, we develop a set of 144 two-dimensional Serre-Green-Naghdi numerical simulations in which we introduce six different values of tsunami wave amplitudes, H/h_0, four barrier widths, $\mathcal{W}$, three onshore barrier locations from the shoreline, $\mathcal{B}_l$, on two different beaches slopes, $\alpha = 1:10$ and 1:20. From their results analysis, we conclude:

1) The runup behind and due to the barrier, R_b, decreases with the increase of the amount and intensity of short-refractions that occur in the stems environment as a consequence of impacts of the tsunami waves against the simulated trees. The amount and intensity of short-refractions increase with the increase of H/h_0 and $\mathcal{W}$ and with the decrease of $\mathcal{B}_l$, which leads to the maximum reduction of the runup, R_b. As per Fig. 5.4 there is common

trend for obtaining R_b/R as function of H/h_0, $\mathcal{W}$ and $\mathcal{B}_l$ and regardless of α as long as 1:20 $\geq \alpha \geq$ 1:10.

2) Every vegetation is potentially capable to reach their R_b. However R_b is not achieved unless the barrier has a minimum length of $\mathcal{L}$. Hence the barrier length $\geq \mathcal{L}$ is a requirement in order to accomplish R_b. If the barrier length $< \mathcal{L}$, the resulting runup behind the barrier will be greater than R_b and determined by the transition zone that develops partially behind the barrier from R_b to R as per Fig. 5.3. It implies that the vegetation barrier is fully functional in reducing the runup just behind the barrier and in areas out of the transition zone influence.

3) The most important factor that determines $\mathcal{L}$ is $\mathcal{B}_l$ as per Fig. 5.5. By avoiding analysis of different barrier locations, not only the accuracy of R_b is affected, but also the minimum length of the barrier/patch studied. We encourage coastal assessments to take into account the location of coastal barrier, regardless of their nature, in order to delineate reliable inundation and evacuation maps as the barrier is more effective when located closer to the shoreline.

4) Due to its importance, we define the transition zone by the use of two lengths: 1) distance from which the runup reaches its minimum value, R_b, measured from the alongshore barrier edge towards the barrier, $\mathcal{L}$; and 2) distance from which the runup is not affected by the barrier at all, measured from alongshore barrier edge, $\mathcal{D}$.

We assume that stems are not affected by the wave impacts as in Yang et al. (2017) and Irish et al. (2014). This assumption may be violated for high H/h_0 waves, so we encourage further studies in this regard for a broader representativeness of these results. We also do not consider biological dynamics of the vegetation.

5.7 Acknowledgments

This material is based upon work supported by the National Science Foundation under Grant Number CMMI-1206271. Any opinions, findings, and conclusions or recommendations expressed in this material are those of the authors and do not necessarily reflect the views of the National Science Foundation.

Chapter 6

Future Work

As computational hardware is advancing, numerical methods are gaining powerful capabilities to simulate larger and more complex problems. However, this involves a further challenge for the numerical methods, not only because, in many cases, they have to improve in order to achieve the new accuracy that the new hardware is able to provide, but also because numerical codes have to be modified in order to become compatible with the new hardware. This, very often, implies that codes that have to be rewritten in order to become compatible with technologies such as GPU or MIC. In this way, simulating the setup presented in the Chapter 5 with the method employed in the second chapter would be very interesting since we would obtain three-dimensional results in the areas where short-refractions occur. The limitation here is to reach a particle size small enough to represent the flow between stems adequately. A coarse estimation would be to represent the space between stems with at least 20 SPH particles. When the numerical method becomes capable to do it, we would be able to measure the energy loss in the front of the vegetated barrier with greater accuracy.

Also, regarding the first research, I propose to develop similar analysis by changing the beach slope. By doing so, conclusions obtained from this research would be more applicable to various cases and in more real scenarios. Also I propose to locate some obstacles in the flow trajectory in the shoreline environment in order to study the slamming forces. The obstacle could largely modify the flow behind it and modify the pattern of the run up too.

However, since the second chapter provides the time and location where the flow reaches its highest flow momentum, it would be extremely useful to provide the velocity profile there so we could provide the worst case scenario for marine structures to stand against.

In Chapter 5, I studied the variation of properties of coastal vegetation barriers in reducing the run up, but the density of stems was considered fixed. I consider it very important to continue this research by proposing different configurations of trees inside of the barrier or even different sizes and shapes of the stems inside the barrier. Also one major assumption made in this chapter was that stability of stems is not affected by the tsunami wave. This assumption could very easily be violated, especially for big waves. For further and more reliable coastal assessments, I consider it necessary to implement stems failure for this kind of research so it can provide a more realistic design criteria.

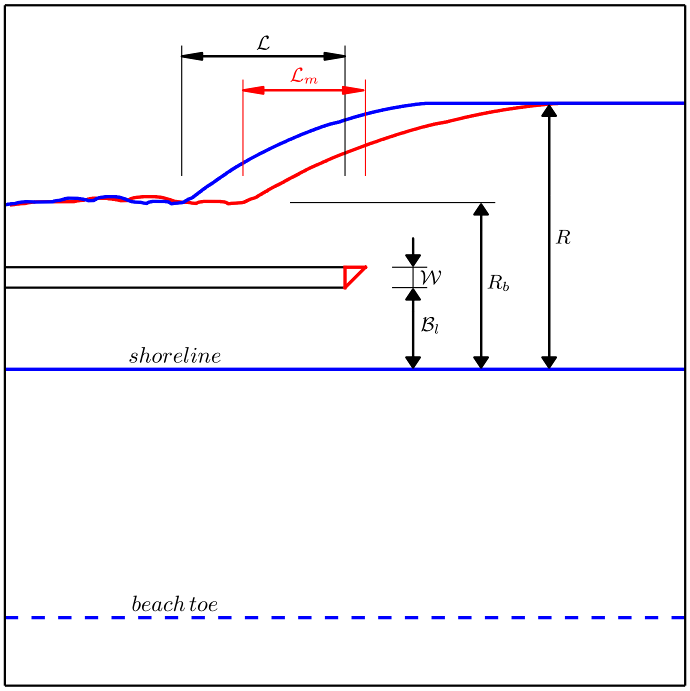

Figure 6.1: Expected modification of the minimum required barrier length $\mathcal{L}_m$, versus $\mathcal{L}$, after adding reflective shape in edge of the vegetated barrier. The resources saved from the barrier length could be used to increase the barrier width, $\mathcal{W}$, so R_b would be smaller making the coastal barrier more effective.

I outline an extra proposed work, also related to the Chapter 5. I propose a modification of the vegetation barrier, shown in Fig. 6.1, as an extra red triangular shape located at the edge of the barrier. This implementation could lead to a reorientation of the long-refraction away from the barrier, so the barrier length would reduce from $\mathcal{L}$ to $\mathcal{L}_m$. The resources saved with this reduction of the barrier length can be used in increasing the barrier width, which would help in greatly reducing the runup behind the barrier thereby making it more efficient.

Bibliography

Anderson, M. E., Smith, J., 2014. Wave attenuation by flexible, idealized salt marsh vegetation. Coastal Engineering 83, 82–92.

Baldock, T., Cox, D., Maddux, T., Killian, J., Fayler, L., 2009. Kinematics of breaking tsunami wavefronts: A data set from large scale laboratory experiments. Coastal Engineering 56 (5), 506–516.

Bonneton, P., Chazel, F., Lannes, D., Marche, F., Tissier, M., 2011. A splitting approach for the fully nonlinear and weakly dispersive Green–Naghdi model. Journal of Computational Physics 230 (4), 1479–1498.

Bradford, S. F., 2000. Numerical simulation of surf zone dynamics. Journal of waterway, port, coastal, and ocean engineering 126 (1), 1–13.

Clercx, H., Maassen, S., Van Heijst, G., 1999. Decaying two-dimensional turbulence in square containers with no-slip or stress-free boundaries. Physics of Fluids 11, 611.

Dalrymple, R., Rogers, B., 2006. Numerical modeling of water waves with the sph method. Coastal engineering 53 (2), 141–147.

Dunbar, P. K., Weaver, C. S., 2008. US States and Territories National Tsunami Hazard

Assessment: Historical Record and Sources for Waves. US Department of Commerce, National Oceanic and Atmospheric Administration Washington, DC.

Feagin, R. A., Mukherjee, N., Shanker, K., Baird, A. H., Cinner, J., Kerr, A. M., Koedam, N., Sridhar, A., Arthur, R., Jayatissa, L. P., et al., 2010. Shelter from the storm. use and misuse of coastal vegetation bioshields for managing natural disasters. Conservation Letters 3 (1), 1–11.

FEMA, J., 2008. Guidelines for design of structures for vertical evacuation from tsunamis.

FEMA, P., 2011. 55, coastal construction manual: Principles and practices of planning, siting, designing, constructing, and maintaining residential buildings in coastal areas, (2011).

Gesteira, M., Rogers, B., Dalrymple, R., Crespo, A., Narayanaswamy, M., 2008. User guide for the sphysics code.

Gingold, R. A., Monaghan, J. J., 1977. Smoothed particle hydrodynamics-theory and application to non-spherical stars. Monthly notices of the royal astronomical society 181, 375–389.

Gomez-Gesteira, M., Dalrymple, R. A., 2004. Using a three-dimensional smoothed particle hydrodynamics method for wave impact on a tall structure. Journal of Waterway, Port, Coastal, and Ocean Engineering 130 (2), 63–69.

Goseberg, N., 2013. Reduction of maximum tsunami run-up due to the interaction with beachfront development–application of single sinusoidal waves. Natural Hazards and Earth System Science 13 (2013), Nr. 11.

Grassa, J., 2007. Wave forces on a wavemaker. sph simulation and comparison with analytic results. In: Proceedings of the Congress-International Association for Hydraulic Research. Vol. 32. p. 101.

Grassa, J. M., 2004. El método sph. aplicaciones en ingeniería marítima. Ingeniería Civil (133), 37–55.

Hammack, J. L., Segur, H., 1978. Modelling criteria for long water waves. Journal of Fluid Mechanics 84 (02), 359–373.

Hérault, A., Bilotta, G., Dalrymple, R. A., 2010. Sph on gpu with cuda. Journal of Hydraulic Research 48 (S1), 74–79.

Hérault, A., Bilotta, G., Dalrymple, R. A., Rustico, E., Del Negro, C., 2006-2014. GPUSPH.

Hibberd, S., Peregrine, D., 1979. Surf and run-up on a beach: a uniform bore. Journal of Fluid Mechanics 95 (02), 323–345.

Ho, D., Meyer, R., 1962. Climb of a bore on a beach. part 1. uniform beach slope. Journal of Fluid Mechanics 14 (02), 305–318.

Irish, J. L., Weiss, R., Yang, Y., Song, Y. K., Zainali, A., Marivela-Colmenarejo, R., 2014. Laboratory experiments of tsunami run-up and withdrawal in patchy coastal forest on a steep beach. Natural Hazards 74 (3), 1933–1949.

Irtem, E., Gedik, N., Kabdasli, M. S., Yasa, N. E., 2009. Coastal forest effects on tsunami run-up heights. Ocean Engineering 36 (3), 313–320.

Ismail, H., Wahab, A. A., Alias, N. E., 2012. Determination of mangrove forest performance in reducing tsunami run-up using physical models. Natural hazards 63 (2), 939–963.

Jones, J. E., 1924. On the determination of molecular fields. II. From the equation of state of a gas. In: Proceedings of the Royal Society of London A: Mathematical, Physical and Engineering Sciences. Vol. 106. The Royal Society, pp. 463–477.

Koshimura, S., Namegaya, Y., Yanagisawa, H., 2009a. Tsunami fragilitya new measure to identify tsunami damage. Journal of Disaster Research 4 (6), 479–488.

Koshimura, S., Oie, T., Yanagisawa, H., Imamura, F., 2009b. Developing fragility functions for tsunami damage estimation using numerical model and post-tsunami data from banda aceh, indonesia. Coastal Engineering Journal 51 (03), 243–273.

Lannes, D., Bonneton, P., 2009. Derivation of asymptotic two-dimensional time-dependent equations for surface water wave propagation. Physics of Fluids (1994-present) 21 (1), 016601.

Li, J., Liu, H.-x., Tan, S. K., 2010. Lagrangian modeling of tidal bores passing through bridge piers. Journal of Hydrodynamics, Ser. B 22 (5), 513–519.

Lin, P., Chang, K.-A., Liu, P. L.-F., 1999. Runup and rundown of solitary waves on sloping beaches. Journal of waterway, port, coastal, and ocean engineering 125 (5), 247–255.

Liu, P. L.-F., 1994. Model equations for wave propagations from deep to shallow water. Advances in coastal and ocean engineering 1, 125–157.

López, D., de Blas, M., Marivela, R., Rebollo, J. J., Díaz, R., Sánchez-Juny, M., Estrella, S., 2011. Estudio hidrodinámico de vertederos y rápidas escalonadas con modelo numérico tridimensional sph. proyecto alivesca. In: Actas del Congreso JIA.

López, D., Marivela, R., 2009. Applications of the sph model to the design of fishways. In: Proceedings of 33rd Congress of IAHR. Water Engineering for a Sustainable Environment The International, Vancouvert. pp. 9–14.

López, D., Marivela, R., Aranda, F., 2009. Calibration of sph model using prototype pressure data from the stilling basin of the villar del rey dam, spain. In: Proceedings of 33rd Congress of IAHR. Water Engineering for a Sustainable Environment The International, Vancouvert. pp. 9–14.

López, D., Marivela, R., Garrote, L., 2010. Smoothed particle hydrodynamics model applied to hydraulic structures: a hydraulic jump test case. Journal of Hydraulic Research 48 (S1), 142–158.

Lucy, L., 1977. A numerical approach to the testing of fusion processes. The Astronomical J 82, 1013–1024.

Lynett, P., Liu, P. L.-F., 2004a. A two-layer approach to wave modelling. In: Proceedings of The Royal Society of London A: Mathematical, Physical and Engineering Sciences. Vol. 460. The Royal Society, pp. 2637–2669.

Lynett, P. J., Liu, P. L.-F., 2004b. Linear analysis of the multi-layer model. Coastal Engineering 51 (5), 439–454.

Lynett, P. J., Wu, T.-R., Liu, P. L.-F., 2002. Modeling wave runup with depth-integrated equations. Coastal Engineering 46 (2), 89–107.

Maassen, S., Clercx, H., van Heijst, G., 2002. Self-organization of quasi-two-dimensional turbulence in stratified fluids in square and circular containers. Physics of Fluids 14, 2150.

Madsen, P. A., Fuhrman, D. R., Schäffer, H. A., 2008. On the solitary wave paradigm for tsunamis. Journal of Geophysical Research: Oceans (1978–2012) 113 (C12).

Madsen, P. A., Fuhrman, D. R., Wang, B., 2006. A boussinesq-type method for fully nonlinear waves interacting with a rapidly varying bathymetry. Coastal Engineering 53 (5), 487–504.

Madsen, P. A., Schaeffer, H. A., 2010. Analytical solutions for tsunami runup on a plane beach: Single waves, n-waves and transient waves. Journal of Fluid Mechanics 645, 27–57.

Marivela, R., López, D., 2011. Calibración de la rugosidad de contorno en modelos sph. In: Actas del Congreso JIA.

Marivela, R., Weiss, R., Synolakis, C., 2016. The temporal and spatial evolution of momentum, kinetic energy and force in tsunami waves during breaking and inundation. arXiv preprint arXiv:1611.04514.

Maza, M., Lara, J. L., Losada, I. J., 2015. Tsunami wave interaction with mangrove forests: A 3-d numerical approach. Coastal Engineering 98, 33–54.

Mei, C. C., Chan, I.-C., Liu, P. L.-F., Huang, Z., Zhang, W., 2011. Long waves through emergent coastal vegetation. Journal of Fluid Mechanics 687, 461–491.

Mendez, F. J., Losada, I. J., 2004. An empirical model to estimate the propagation of random breaking and nonbreaking waves over vegetation fields. Coastal Engineering 51 (2), 103–118.

Monaghan, J., Kajtar, J., 2009. Sph particle boundary forces for arbitrary boundaries. Computer Physics Communications 180 (10), 1811–1820.

Monaghan, J. J., 1992. Smoothed particle hydrodynamics. Annual review of astronomy and astrophysics 30, 543–574.

Monaghan, J. J., 1994. Simulating free surface flows with sph. Journal of computational physics 110 (2), 399–406.

Nandasena, N., Sasaki, Y., Tanaka, N., 2012. Modeling field observations of the 2011 great east japan tsunami: Efficacy of artificial and natural structures on tsunami mitigation. Coastal Engineering 67, 1–13.

Nandasena, N., TANAKA, N., TANIMOTO, K., 2008. Perspective of coastal vegetation patches with topography variations for tsunami protection in 2d-numerical modeling. PROCEEDINGS OF HYDRAULIC ENGINEERING 52, 133–138.

Park, H., Cox, D. T., Lynett, P. J., Wiebe, D. M., Shin, S., 2013. Tsunami inundation modeling in constructed environments: a physical and numerical comparison of free-surface elevation, velocity, and momentum flux. Coastal Engineering 79, 9–21.

Peregrine, D. H., 1967. Long waves on a beach. Journal of fluid mechanics 27 (04), 815–827.

Popinet, S., 2015. A quadtree-adaptive multigrid solver for the Serre–Green–Naghdi equations. Journal of Computational Physics 302, 336–358.

Pujara, N., Liu, P. L.-F., Yeh, H., 2015. The swash of solitary waves on a plane beach: flow evolution, bed shear stress and run-up. Journal of Fluid Mechanics 779, 556–597.

Qi, Z., Eames, I., Johnson, E., 2014. Force acting on a square cylinder fixed in a free-surface channel flow. Journal of Fluid Mechanics 756, 716–727.

Robinson, M., Monaghan, J. J., 2012. Direct numerical simulation of decaying two-dimensional turbulence in a no-slip square box using smoothed particle hydrodynamics. International Journal for Numerical Methods in Fluids 70 (1), 37–55.

Roeber, V., Cheung, K. F., 2012. Boussinesq-type model for energetic breaking waves in fringing reef environments. Coastal Engineering 70, 1–20.

Rueben, M., Holman, R., Cox, D., Shin, S., Killian, J., Stanley, J., 2011. Optical measurements of tsunami inundation through an urban waterfront modeled in a large-scale laboratory basin. Coastal Engineering 58 (3), 229–238.

Shao, S., 2006. Simulation of breaking wave by sph method coupled with k- model. Journal of Hydraulic Research 44 (3), 338–349.

Smagorinsky, J., 1963. General circulation experiments with the primitive equations: I. the basic experiment*. Monthly weather review 91 (3), 99–164.

Strusinska-Correia, A., Husrin, S., Oumeraci, H., 2013. Tsunami damping by mangrove forest: a laboratory study using parameterized trees. Natural Hazards and Earth System Sciences 13 (2), 483.

Synolakis, C., Kânoğlu, U., 2015. The Fukushima accident was preventable. Phil. Trans. R. Soc. A 373 (2053), 20140379.

Synolakis, C. E., 1986. The runup of long waves. Ph.D. thesis, California Institute of Technology.

Synolakis, C. E., 1987. The runup of solitary waves. Journal of Fluid Mechanics 185, 523–545.

Synolakis, C. E., 1990. Generation of long waves in laboratory. Journal of Waterway, Port, Coastal, and Ocean Engineering 116 (2), 252–266.

Synolakis, C. E., Bernard, E. N., 2006. Tsunami science before and beyond boxing day 2004. Philosophical Transactions of the Royal Society of London A: Mathematical, Physical and Engineering Sciences 364 (1845), 2231–2265.

Synolakis, C. E., Skjelbreia, J. E., 1993. Evolution of maximum amplitude of solitary waves on plane beaches. Journal of Waterway, Port, Coastal, and Ocean Engineering 119 (3), 323–342.

Tanaka, N., 2009. Vegetation bioshields for tsunami mitigation: review of effectiveness, limitations, construction, and sustainable management. Landscape and Ecological Engineering 5 (1), 71–79.

Tanaka, N., Sasaki, Y., Mowjood, M., Jinadasa, K., Homchuen, S., 2007. Coastal vegetation structures and their functions in tsunami protection: experience of the recent Indian Ocean tsunami. Landscape and Ecological Engineering 3 (1), 33–45.

Tang, J., Shen, Y., Causon, D. M., Qian, L., Mingham, C. G., 2017. Numerical study of periodic long wave run-up on a rigid vegetation sloping beach. Coastal Engineering 121, 158–166.

Thuy, N. B., Tanaka, N., Tanimoto, K., 2012. Tsunami mitigation by coastal vegetation considering the effect of tree breaking. Journal of Coastal Conservation 16 (1), 111–121.

Thuy, N. B., Tanimoto, K., Tanaka, N., Harada, K., Iimura, K., 2009. Effect of open gap in coastal forest on tsunami run-upinvestigations by experiment and numerical simulation. Ocean Engineering 36 (15), 1258–1269.

Tissier, M., Bonneton, P., Marche, F., Chazel, F., Lannes, D., 2012. A new approach to handle wave breaking in fully non-linear Boussinesq models. Coastal Engineering 67, 54–66.

Valizadeh, A., Monaghan, J., et al., 2012. Sph simulations of turbulence in fixed and rotating boxes in two dimensions with no-slip boundaries. arXiv preprint arXiv:1202.2936.

Van Heijst, G., Clercx, H., Molenaar, D., 2006. The effects of solid boundaries on confined two-dimensional turbulence. Journal of Fluid Mechanics 554, 411–432.

Wang, B., Guo, X., Mei, C. C., 2015. Surface water waves over a shallow canopy. Journal of Fluid Mechanics 768, 572–599.

Wei, G., Kirby, J. T., Grilli, S. T., Subramanya, R., 1995. A fully nonlinear Boussinesq model for surface waves. Part 1. Highly nonlinear unsteady waves. Journal of Fluid Mechanics 294, 71–92.

Yang, Y., Irish, J. L., Weiss, R., 2016. Investigation of tsunami impact through discontinuous vegetation. Submitted.

Yang, Y., Irish, J. L., Weiss, R., 2017. Impact of patchy vegetation on tsunami dynamics. Journal of Waterway, Port, Coastal, and Ocean Engineering, 04017005.

Yeh, H., 2006. Maximum fluid forces in the tsunami runup zone. Journal of waterway, port, coastal, and ocean engineering 132 (6), 496–500.

Yeh, H. H., 1991. Tsunami bore runup. In: Tsunami Hazard. Springer, pp. 209–220.

Yeh, H. H., Ghazali, A., Marton, I., 1989. Experimental study of bore run-up. Journal of fluid Mechanics 206, 563–578.

Yeh, H. H.-j., Synolakis, C., Liu, P. L.-F., 1996. Long-wave Runup Models: Friday Harbor, USA, 12-17 September 1995. World Scientific.

Zainali, A., 2016. High-fidelity numerical simulation of shallow water waves. Ph.D. thesis, Virginia Tech.

Zainali, A., Marivela, R., Weiss, R., Irish, J. L., Yang, Y., 2016. Numerical simulation of nonlinear long waves interacting with arrays of emergent cylinders. arXiv preprint arXiv:1610.00687.

Zhang, Y., Kennedy, A. B., Panda, N., Dawson, C., Westerink, J. J., 2013. Boussinesq–green–naghdi rotational water wave theory. Coastal Engineering 73, 13–27.

Zheng, K., Sun, Z.-c., Sun, J.-w., Zhang, Z.-m., Yang, G.-p., Zhou, F., 2009. Numerical simulations of water wave dynamics based on sph methods. Journal of Hydrodynamics, Ser. B 21 (6), 843–850.

Zhu, L., Chen, Q., 2015. Numerical modeling of surface waves over submerged flexible vegetation. Journal of Engineering Mechanics 141 (8), A4015001.